



HAL
open science

Out-of-equilibrium states of the electric double layer

Zouhir Benrahla

► **To cite this version:**

Zouhir Benrahla. Out-of-equilibrium states of the electric double layer. Physics [physics]. Université de Bordeaux, 2022. English. NNT : 2022BORD0313 . tel-03982037

HAL Id: tel-03982037

<https://theses.hal.science/tel-03982037v1>

Submitted on 10 Feb 2023

HAL is a multi-disciplinary open access archive for the deposit and dissemination of scientific research documents, whether they are published or not. The documents may come from teaching and research institutions in France or abroad, or from public or private research centers.

L'archive ouverte pluridisciplinaire **HAL**, est destinée au dépôt et à la diffusion de documents scientifiques de niveau recherche, publiés ou non, émanant des établissements d'enseignement et de recherche français ou étrangers, des laboratoires publics ou privés.

THÈSE POUR OBTENIR LE GRADE DE

DOCTEUR DE
L'UNIVERSITÉ DE BORDEAUX
.....

ÉCOLE DOCTORALE SCIENCES PHYSIQUES ET DE L'INGÉNIEUR

LASERS, MATIÈRE ET NANOSCIENCES.

LABORATOIRE DE LOMA - UNIVERSITÉ DE BORDEAUX.

OUT-OF- EQUILIBRIUM STATES OF THE ELECTRIC DOUBLE LAYER
.....

ÉTATS HORS ÉQUILIBRE DE LA DOUBLE COUCHE ÉLECTRIQUE
.....

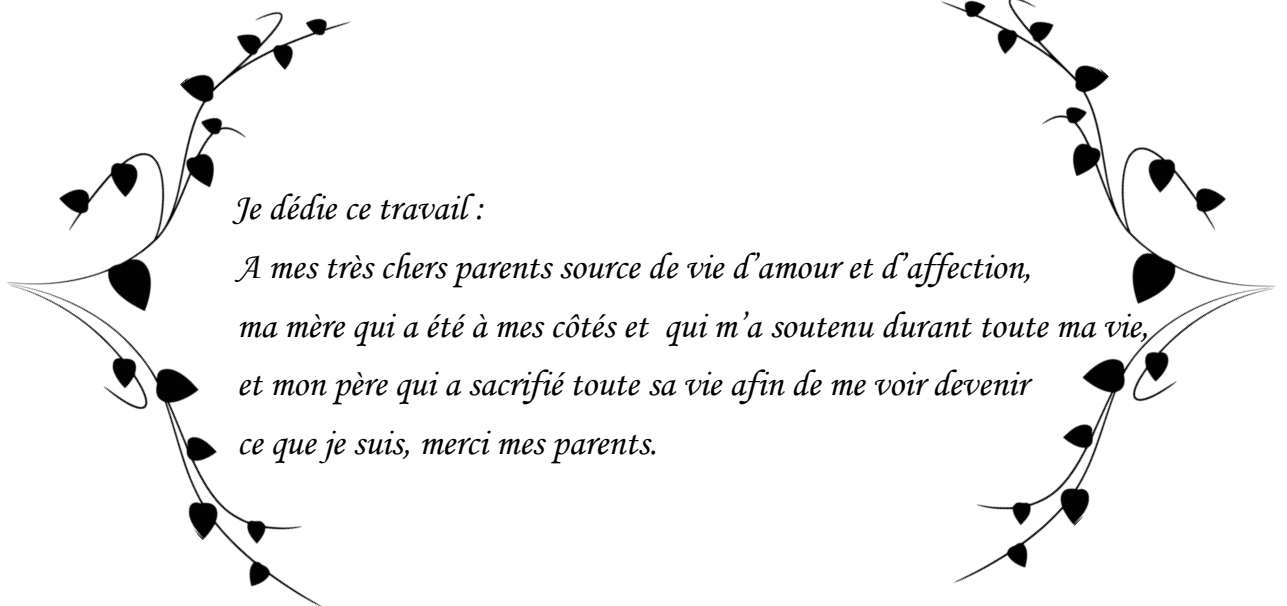
Par: **BENRAHLA Zouhir**

Sous la direction de : **WÜRGER Aloïs**

Soutenue le 25 Novembre 2022.

Membres du jury :

M. ONDARÇUHU Thierry	Directeur de recherche CNRS	Université de Toulouse	Rapporteur
M. MESSINA René	Professeur	Université de Lorraine	Rapporteur
M. GRELET Eric	Directeur de recherche CNRS	Université de Bordeaux	Président
M. WÜRGER Aloïs	Professeur	Université de Bordeaux	Directeur



Je dédie ce travail :

*A mes très chers parents source de vie d'amour et d'affection,
ma mère qui a été à mes côtés et qui m'a soutenu durant toute ma vie,
et mon père qui a sacrifié toute sa vie afin de me voir devenir
ce que je suis, merci mes parents.*

REMERCIEMENTS

Ce travail théorique du projet ANR sur la double couche électrique dynamique (EDDL) a été réalisé au sein du laboratoire onde et matière d'Aquitaine (LOMA) à l'université de Bordeaux, en étroite collaboration avec les groupes expérimentaux de MAALI Abdelhamid (LOMA, Université de Bordeaux) et Élisabeth Charlaix (LIPHY, Université de Grenoble).

Je tiens à remercier dans un premier temps, le directeur du laboratoire LOMA et mon enseignant de master 2. Monsieur PISTOLESI Fabio, de m'avoir accueilli au sein du laboratoire.

Je voudrais remercier, mon directeur de thèse Monsieur WÜRGER Aloïs, professeur de physique à l'université de Bordeaux, pour sa patience, sa disponibilité et surtout ses judicieux conseils et critiques, qui ont contribué à alimenter ma réflexion. Merci de m'avoir proposé ce sujet de thèse qui m'a permis de faire mes premiers pas dans la recherche scientifique, pour le temps que t'as consacré pour me diriger tout au long de cette thèse malgré ton emploi du temps chargé d'enseignement et engagements professionnels, Finalement, merci d'avoir partagé avec moi tes connaissances et expériences et ta sagesse de vie.

J'adresse tous mes remerciements à Monsieur ONDARÇUHU Thierry, directeur de recherche à l'université de Toulouse, ainsi qu'à Monsieur MESSINA René, professeur à l'université de Lorraine. De l'honneur qu'ils m'ont fait en acceptant d'être rapporteurs de cette thèse, pour leurs commentaires enrichissants et constructifs sur ce manuscrit.

Je remercie Monsieur MAALI Abdelhamid, directeur de recherche à l'université de Bordeaux, pour l'honneur qu'il m'a fait d'être présent au jour de ma soutenance, votre présence était vraiment un soulagement ! Qu'il soit aussi remercié pour son aide (surtout pour les manipulations d'AFM), sa gentillesse, sa disponibilité permanente, il a toujours été là pour me soutenir et me conseiller au cours de cette thèse.

Je tiens à remercier particulièrement Monsieur DRUMMOND Carlos, directeur de recherche à l'université de Bordeaux et mon directeur de stage de Master 2, je lui exprime mon grand respect. Pour ces précieux conseils dans le domaine professionnel ainsi que dans la vie quotidienne, merci beaucoup pour votre aide Monsieur.

Je tiens à remercier RODRIGUEZ MATUS Marcela acienne doctorante dans mon groupe, pour son aide et ces délicieux cakes ! Et comment ne pas penser à BARCHI Yasma pour son aide et son soutien le long de ces trois années, et durant les moments difficiles surtout la période du Covid 19, ce que t'as fait pour moi, je ne l'oublierai jamais.

Finalement, un grand merci à ma famille pour leur soutien sans faille, surtout mes chers parents pour leurs encouragements et leurs confiances, ils n'ont cessé de prier pour moi durant mon cursus scolaire et m'ont encouragé régulièrement. Merci maman pour ta patience. Papa, t'étais et tu resteras toujours ma source d'inspiration et du courage. "You are the best". Un grand merci aussi à Adel, Lamin, Malek et tous les membres de ma famille, je vous remercie profondément et je vous offre ce travail.

Abstract

This manuscript presents the theoretical work done during my PhD, on the electric double layer in the non-equilibrium state. The contact of an electrolyte solution with a solid surface gives rise to two opposite charge layers, a fixed layer of ions and a diffuse layer of counterions. The coupling of the diffuse layer with the liquid flow causes various electrokinetic and viscoelectric effects. To study these effects, we consider two generic situations of confined electrolyte solution between a sphere and a substrate, where the sphere moves in the normal or the radial direction with respect to the substrate. Experimentally, these situations are realized by a colloidal sphere mounted on an AFM close to the substrate.

Our investigation on the coupling between the diffuse layer and the liquid, is a completion to several previous works. We have used Onsager equations to evaluate the charge-flow coupling effects, by means of transport coefficients evaluated numerically and analytically at the equilibrium state. The coupling showed an enhancement of the viscous and dynamic responses but still weak compared to the measured responses. Our results confirm the fact that the flow-charge coupling only is insufficient to interpret the experimental findings. The description based on the charge-flow coupling misses an additional element which is the salt contained in the electrolyte solution.

For this purpose, we took into account the salt in the electrolyte solution and studied the effect of the salt-charge-flow coupling, by means of Onsager coefficients calculated in the equilibrium state as a preliminary approach. The result we found does not explain the measured responses either. We realized then the fact that the sphere vibrations significantly modify the salt density and keep it far from its equilibrium state, given the slow backdiffusion of the salt and the weak thermodynamic force, which does not succeed in counteracting the salt advected by the sphere motion.

Chapter 5 provided the evidence that salt-dependent Onsager coefficients must be calculated in the non-equilibrium state rather than the equilibrium state. Therefore we proposed in chapter 6, a theoretical model to calculate the coupling coefficients in the non-equilibrium state, taking into account the time dependence of the salt in the continuity equation.

Keywords : out of equilibrium electric double layer, electroviscous force, electrokinetic lift force, onsager coefficients, salt diffusion, relaxation time.

Résumé

Ce manuscrit présente le travail théorique effectué pendant mon doctorat, sur la double couche électrique dans l'état hors équilibre. Le contact d'une solution électrolyte avec une surface solide donne naissance à deux couches de charges opposées, une couche d'ions fixe et une couche diffuse de contre-ions. Le couplage de la couche diffuse avec l'écoulement du liquide provoque, divers effets électrocinétiques et viscoélectriques. Pour étudier ces effets, nous considérons deux situations expérimentales, une solution électrolytique confinée entre une sphère et un substrat, où la sphère se déplace dans la direction verticale dans un cas et dans la direction parallèle au substrat dans un autre cas. Expérimentalement, ces deux situations sont réalisées par une sphère colloïdale montée sur le cantilever d'un AFM et un substrat.

Notre investigation sur le couplage entre la couche diffuse et l'écoulement, est un travail complémentaire aux travaux précédents. Nous avons utilisé des équations simples qui nous ont permis d'évaluer les effets du couplage, à partir des coefficients d'Onsager que nous avons évalués numériquement et analytiquement à l'état d'équilibre. Le couplage a montré une amélioration des réponses visqueuses et dynamiques, mais toujours faible par rapport aux réponses mesurées. Notre résultat confirme le fait que le couplage charge-écoulement est insuffisant pour interpréter les résultats expérimentaux. La description basée sur le couplage charge-écoulement manque un élément supplémentaire qui est le sel contenu dans la solution d'électrolyte.

Pour cela, nous avons pris en compte le sel de la solution électrolyte et on a étudié l'effet du couplage sel-charge-flux, par le biais des coefficients d'Onsager calculés à l'état d'équilibre dans le cadre d'une approche préliminaire. Le résultat que nous avons trouvé n'explique pas non plus les résultats expérimentaux, et on a réalisé ensuite que les vibrations de la sphère modifient significativement la densité du sel et la maintiennent loin de son état d'équilibre, étant donné la rétrodiffusion lente du sel et la faible force thermodynamique qui ne parvient pas à contrecarrer le sel advecté par le mouvement de la sphère.

Le chapitre 5 a fourni une preuve que les coefficients d'Onsager dépendent du sel, doivent être calculés dans l'état hors-équilibre plutôt que dans l'état d'équilibre. Nous avons donc proposé au chapitre 6, un modèle théorique pour calculer les coefficients de Onsager dans l'état hors équilibre, en tenant compte de la dépendance temporelle du sel dans l'équation de continuité.

Mots-clés: double couche électrique hors équilibre, force électrovisqueuse, force de portance électrocinétique, coefficients d'Onsager, diffusion de sel, temps de relaxation.

Contents

1	Introduction	10
1.1	Electric double layer at charged surfaces	11
1.2	Electrostatic interactions of nearby surfaces	12
1.3	Electrokinetic phenomena	14
1.4	Confinement with an open geometry!	17
1.5	Sphere-plane relative motion	19
1.5.1	Squeezing motion	19
1.5.2	Sliding motion	20
1.6	Thesis plan	22
2	Electrostatics	23
2.1	Poisson Boltzmann mean field theory	23
2.2	1D Poisson Boltzmann equation	24
2.2.1	Electrostatic potential for infinite half-space	24
2.2.2	Electrostatic potential in a narrow channel	26
2.3	CC, CP and CR boundary conditions	29
2.3.1	Constant charge boundary condition (CC)	29
2.3.2	Constant potential boundary condition (CP)	31
2.3.3	Charge regulation boundary condition (CR)	31
2.4	Out of equilibrium force	32
3	Hydrodynamics	34
3.1	Stokes equation	34
3.2	Lubrication approximation	35
3.3	1D Stokes equation	37
3.4	Velocity profile components	38
3.4.1	Pressure driven velocity	38
3.4.2	Electroosmotic velocity	39
3.4.3	Diffusioosmotic velocity	39
4	Charge- flow coupling	42
4.1	Irreversible processes and linear laws	42
4.2	Volume and charge currents	43
4.2.1	Volume current	43
4.2.2	Charge current	44
4.3	Analytic expressions of Onsager's coefficients	45
4.3.1	Wide channel approximation WCA	45
4.3.2	Narrow channel approximation NCA	48
4.4	Mobility effect	50

4.5	The coupling parameter ξ	52
4.6	Electrostatic repulsive force	55
4.7	Electroviscous Force	56
4.8	Electrokinetic lift force	57
4.9	Conclusion	63
5	Salt-charge-flow coupling	64
5.1	Salt-charge and volume currents	65
5.1.1	The volume current	65
5.1.2	Charge current	66
5.1.3	Salt current	67
5.2	Analytic expressions of Onsager's coefficients	67
5.2.1	Wide channel approximation WCA	68
5.2.2	Narrow channel approximation NCA	71
5.3	Salt-charge-flow coupling parameter ξ	74
5.4	Electroviscous force	78
5.5	Conclusion	80
6	Perspectives	81
6.1	Out-of-equilibrium ion densities in a narrow channel	81
6.2	Out of equilibrium Onsager coefficients	83
6.3	Slow relaxation of excess salinity	83
6.4	Discretization of the salt dynamics	85
7	Appendices	87
7.1	Osmotic pressure	87
7.2	Diffusioosmotic pressure gradient	88
7.3	AFM measurement	89
7.4	PB equation solution in asymmetric geometry	90
7.5	PB equation solution in symmetric geometry	91
7.6	Velocity profile components	92
7.6.1	Pressure driven velocity	93
7.6.2	Electroosmotic velocity	94
7.6.3	Diffusioosmotic velocity	95
7.7	Incompressibility condition	95
7.8	Charge and salt profiles in the WCA	96
7.9	Onsager coefficients in WCA	96
7.10	Numerical evaluations	99
7.11	Electrostatic repulsion between two solid surfaces	101
7.12	Charge current relaxation time	102
7.13	Salt-charge-flow coupling parameter ξ	103
7.14	Debye Hückel approximation	103

Chapter 1

Introduction

In the past decades, confined fluid investigations at the micrometer scale have made a significant progress, and inspired the researchers to explore confined fluids at the nanoscale [1–4]. Recently nanofluidics has known notable advancements theoretically and experimentally, as a result of the dedicated work on this novel field of research. New properties have been discovered and harnessed for many applications [5–7], among these widespread applications one can mention:

The energy harvesting technique, based on the osmotic power conversion to a mechanical or electrical energy. Bocquet et al succeeded in manufacturing a device consisting of two reservoirs connected to a nanotube of boron nitride BN via an impermeable membrane. This device can produce a power density of 4 kW.m^{-2} , meaning an efficiency 1000 bigger than the efficiency of the current harvesting devices.

This performance is due on one hand to BN tube, characterized by a high surface charge density sensitive to pH, and on the other hand to the low friction with the flow crossing it [8,9].

The desalination technique involving reverse osmosis processes, where the salt water is pushed through a semipermeable membrane that serves as a filter, letting through only the pure water without salt, thus producing a pure water. [10–12].

The development of high efficiency batteries. Daiguji et al pointed out that the efficiency of a nanofluidic battery consisting of a nanochannel connected to an anode and a cathode, can be improved by increasing the surface charge density of the nanochannel and decreasing its height, afterwards the analysis of Yan et al revealed that the slip length can significantly improve the efficiency of this kind of batteries [13,14].

The nanofluidic diodes manufacturing, based on an asymmetric conical nanopore, one half of which carries a positive charge on its surface and the other half carries a negative charge. Depending on the applied voltage, the concentrations of ions inside the nanopore can be increased or decreased.

This variations in the concentration lead to the generation of a high electric current, in one half of the nanopore and a negligible one in the other half. Therefore the nanofluidic diodes can imitates the electronic diodes, which allow the electric current to circulate only in one direction in a circuit, as shown in the work of Vlassioug et al and Karnik et al [15,16].

In addition to these applications, we get too many others in biotechnology and clinical diagnostics, such as (lab-on-a-chip) a device which combine various laboratory functions on a single chip to perform several analyses simultaneously. In this device nanofluids technologies may used in order to increase its performance by manufacturing nanochannels

which may replace the microchannels currently used [17–19].

All the proprieties emerging from a liquid confined at the nanometric scale, are linked to the charged surfaces of the confinement structure. This charge surface arises from the interaction between the solid surfaces of the structure, and the electrolyte solution made of NaCl dissolved in water for example.

The solid surface-electrolyte solution interaction, generates an organized distribution of two layers of opposite charges. The first layer is formed on the solid surface while the second one is formed near to the first layer, these double layers are separated by a thin layer which adhere to the surface (a compact layer), this latter can be considered as a dielectric in a conventional capacitor [20, 21].

Several experimental techniques and theoretical models, have been developed for a better understanding of the double layer properties. Experimentally one can mention the electrophoresis technique, used to measure ions mobility under the effect of an electric field [22, 23]. Later on the electrophoresis theory developed by Smoluchowski, provided the analytic expression of the mobility well known as the Smoluchowski mobility [24, 25].

Another widely used technique is the capacitance measurements, this technique quantifies the quantity of the charges stored in a double layer capacitor. Providing a thorough understanding on the structure as well as the composition of the electric double layer in terms of physical factors, including ion size and concentration [26–28].

Regarding the forces, which arise from the electrolyte solution confinement at the nanometric scale. The atomic force microscopy provides a pretty complete understanding of interactions, that arise from a confined sample between the AFM probe and a substrate.

This technique provides a thorough and quantitative description, of the forces arising from the double layer interactions in the static and dynamic cases, ranging from Van der Waals forces to the repulsive forces between the bottom surface of the probe and the sample [29, 30].

Theoretically, many models are established either to interpret experimentally made measurements, or to predict the new properties of the confinement. Generally all the theoretical approaches are based on the classical Poisson Boltzmann mean field theory, which adopts Boltzmann distribution and Poisson's equation, to describe the density of charges in the free layer from an average electrostatic potential generated from all charges [31, 32].

1.1 Electric double layer at charged surfaces

It is well known that the interaction of an electrolyte solution with a solid surface, induces two oppositely charged layers in the solid and the liquid mediums respectively. Where the first charged layer in the solid surface is balanced by a second layer of an equal but oppositely charged cloud of counterions, these two layers are known as electric double layer EDL [33, 34].

Some of the counterions form a compact "bound" layer (few angstroms) in the vicinity of the solid surface, known as Stern layer [35, 36]. Whereas the remaining counterions close to the surface exhibit a thermal motion and form the diffuse layer (free layer) [37, 38]. Sufficiently far from the surface in the bulk we consider that the electrolyte solution is neutral as shown in figure (1.1).

For the sake of simplicity, we deal in our investigation, only with a diffuse layer of monovalent counterions, since divalent and trivalent counterions show very important

correlations [113,114].

From a purely electric perspective we can model the electric double layer, as a planar capacitor where Stern layer is considered to act as a dielectric [39–41].

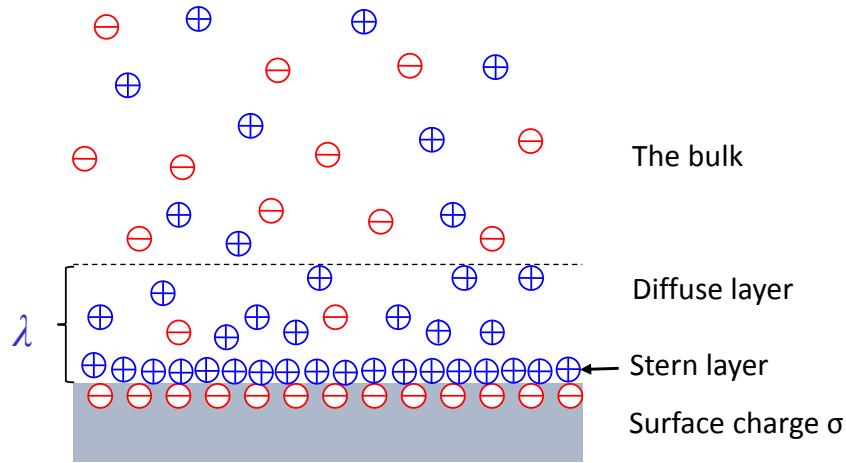


Figure 1.1: Schematic representation of the electric double layer structure. The blue circles refers to the counterions whereas the red circles account for the coions.

It is worthy to explain some of the charging surfaces mechanisms, which lead to the E.D.L establishment. We can think of the ionization which is the dissociation of chemical groups of the solid surface and the physical adsorption of ions from the liquid medium.

The ionization or dissociation reaction, is a reaction in which groups of ionic compounds dissociate in electrolyte solution, into cations and anions. For example the dissociation of protons from the carboxylic groups, ($\text{R} - \text{COOH} \rightarrow \text{R} - \text{COO}^- + \text{H}^+$) resulting in a negatively charged surface [42]. This process depend strongly on the electrolyte solution pH, where the surfaces are generally charged positively for lower pH, and negatively for higher pH.

Adsorption is a surface phenomenon, in which ions from the electrolyte solution attach to a solid surface [43]. This process occur through preferred adsorbing sites e.g., the adsorption of OH^- groups to water-hydrocarbon interfaces making the surface negatively charged with a positive charge excess in the liquid.

1.2 Electrostatic interactions of nearby surfaces

We aim in this section, to understand the origin of the electrostatic repulsion of two close parallel surfaces. For this purpose, let's consider two flat plates parallel to each other having a uniform negative charge density with positive counterions in the gap between them. The dielectric constant of the medium ϵ considered to be homogeneous.

During the surface charging, a coulombic attractive force rises to pull back the counterions onto the surfaces. This attraction is balanced by the osmotic pressure which tends to achieve the state of equilibrium through the redistribution of counterions, the equilibrium

between the electrostatic interactions and the entropy shapes the charge density profile, which we define as the difference between the counterions and the coions densities [21].

The variations of the free energy of the whole system (which can be given by the sum of the electrostatic interactions, and the entropy between the different ions) with respect to the distance of separations, between the two surfaces d [31]. Results in a pressure called the disjoining pressure, first introduced by Deryagin and Kusakov [44]. Relying on the linear superposition of the double layers of both surfaces, one can get the approximation expression [21],

$$P = 64k_B T \rho_0 (4\lambda/b)^2 e^{-z/\lambda}, \quad (1.1)$$

where λ is the diffuse layer thickness, b is the Debye length and k_B Boltzmann constant, z measures the distance between the planar surfaces, ρ is the bulk concentration of ions.

Near the midplane between similarly charged surfaces (1.2), the electric field vanishes and the disjoining pressure, is merely given by the excess of the osmotic pressure. Thus the repulsion between the solid surfaces originates from the excess of the osmotic pressure at the midplane, this latter tends to set apart the two surfaces [21]. Further details about the disjoining pressure as well as the excess osmotic pressure are given in the appendix (7.1) .

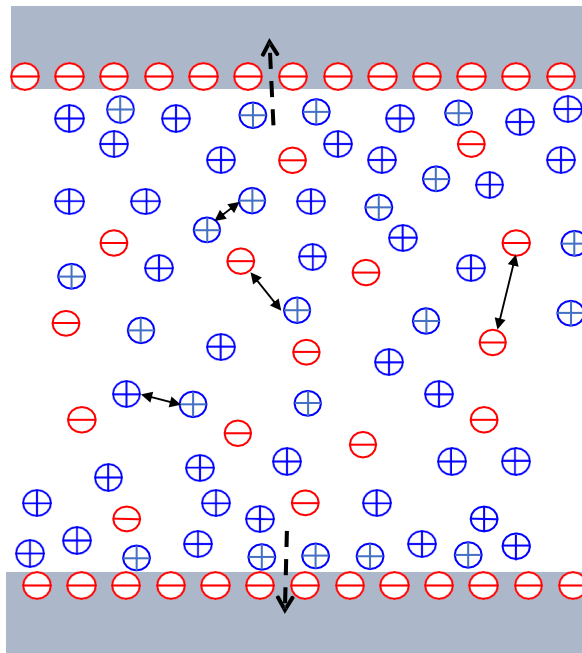


Figure 1.2: Schematic representation of the electrostatic repulsion of two parallel surfaces, the solid arrows express the electrostatic interactions between charges whereas the dashed arrows indicate the repulsive force between the surfaces.

The system of two solid surfaces interacting through an electrolyte solution, can give rise to several kinds of forces. Indeed for medium separations (in the mean field approximation), we have seen that the surfaces repel each other.

This repulsion can be transformed into attraction force, if the two surfaces are brought much closer to each other, so the counterions between the surfaces experience correlated electrostatic interactions, which dominate the osmotic pressure in the gap between the

surfaces. Thus the two charged surfaces with $-\sigma$, are attracted to the correlated counterions that can be modeled as a solid surface charged with $+2\sigma$ [45].

Similarly the attractive Van Der Waals forces, due to the thermal fluctuations of the neighboring atoms dipoles of the surfaces [46]. Can be measured if the surfaces are close enough and a quantity of salt is added to reduce sufficiently the diffuse layer thickness.

It is worth to mention, that the electrostatic interactions of nearby surfaces are described earlier by the classical theory of Derjaguin, Landau, Verwey, and Overbeek (DLVO theory), which assumes that the interaction between two solid surfaces in aqueous solution, can be approximated by a superposition of van der Waals and the double layer forces [47].

Peshel et al treated experimentally the interaction of two planar surfaces of silica immersed in LiCl, NaCl and KCl solutions [48]. They found good agreement between the experimental findings for both EDL repulsive and Van der Waals attractive forces and the theory predictions, especially for separations higher than 4nm.

For smaller separations, they confirmed the existence of an additional repulsive force measured earlier by Israelachvili and Adams [49]. Pashlay referred this supplementary repulsive force to the hydration effects [50].

Further new forces which are not predicted by the DLVO model, are measured recently by Smith et al [51], they pointed out that the origin of these new forces is still unknown and requires further research to elucidate it.

1.3 Electrokinetic phenomena

The electrokinetic phenomena refer mainly, to the relative motion between the contents of the electric double layers. More precisely the transport of the diffuse layer content near a fixed charged surface under the influence of an external force.

This relative motion between the constituents of the diffuse layer and the charged solid surface, is at the origin of many interfacial transport phenomena such as electroosmosis, electrophoresis, diffusioosmosis and diffusiophoresis.

Electroosmosis and diffusioosmosis expresses the generation of a flow in the interfacial structure, by the application of an external force.

The electroosmosis is the motion of the liquid near a charged solid surface, under the effect of an electric field applied parallel to the surface (1.3). When the counterions of the diffuse layer move under the effect of the electric field, they drag the liquid along them producing a flow [52, 53].

The electroosmotic velocity v which expresses the velocity of the liquid with respect to the solid surface can be given by,

$$v = \mu_{eo}E, \quad (1.2)$$

where the electroosmotic mobility is given by the Smoluchowski formula,

$$\mu_{eo} = \frac{\epsilon\zeta}{\eta}, \quad (1.3)$$

with the permittivity ϵ and ζ the electrostatic potential at the solid surface, η is the electrolyte solution dynamic viscosity. Further details on the derivation of (1.3) are given in chapters 3 and 5.

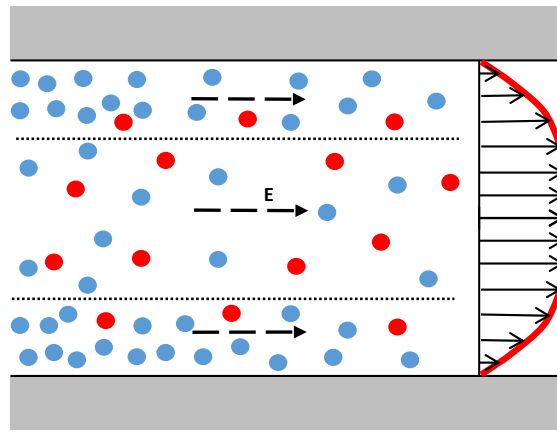


Figure 1.3: Schematic illustration of the electroosmotic effect. The blue circles refer to the counterions whereas the red circles express the coions, the black dashed arrows account for the applied electric field. The free ions in the bulk region where the salinity is given by n_0 give rise to a constant velocity profile.

The diffusioosmosis is the flow adjacent to a stationary wall or pore surface, derived by a concentration gradient in the solution, see figure below. Where the difference in the ion concentrations near and far from the solid surface, generates a difference in the thermodynamic force density $-k_B T \nabla n$, this latter causes the liquid flow generation [54, 55]. For more insights about the diffusioosmosis effects see appendix (7.2).

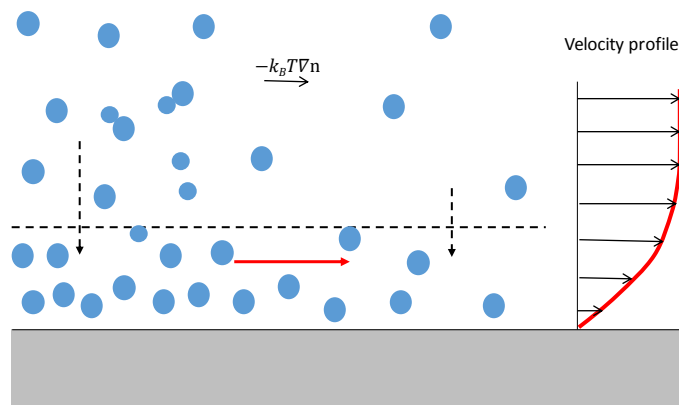


Figure 1.4: Schematic illustration of the diffusioosmotic process. The solid black arrow expresses the thermodynamic force, the red arrow refers to the liquid flow and the dashed black arrows account for the ions density near and far from the solid surface.

For further illustration let's consider an electrolyte solution between two uncharged solid surfaces. In such cases the salt diffuses homogeneously in the channel, thus the salt diffusion can not generate a liquid flow. However in the case of charged solid surfaces, the

interaction potential between the surfaces and the salt in the channel, induces a difference in the salt density near and far the solid surface.

This difference in the salt density, give rise to a difference in the thermodynamic force $-k_B T \nabla n$, which generates a liquid flow in the channel.

Electrophoresis and Diffusiophoresis are processes which bearing on the motion of particles, such as colloid particles under the effect of a solute gradients (applied electric field for the case of electrophoresis).

Diffusiophoresis or Chemiophoresis is a compound processes, based on the motion of a colloid (negatively charged for example) along an imposed salt gradient. The latter gives rise to both an electroosmotic and diffusioosmotic flows on the colloid surface in the direction opposite to the salt gradient, see figure below. The total flow induced balances the salt gradient effect and pushes forward the colloid particle [56, 57].

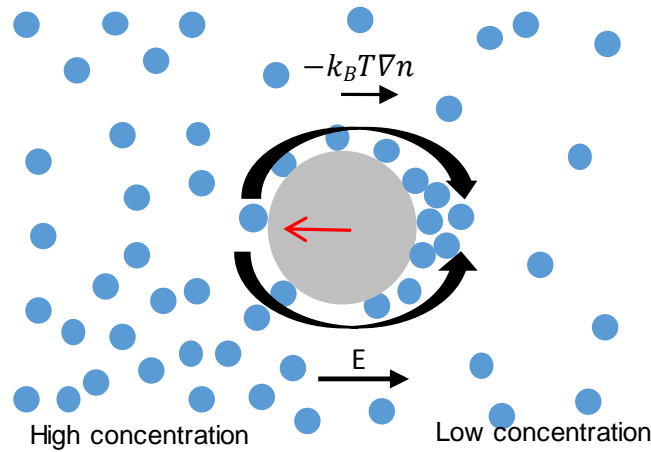


Figure 1.5: Schematic view of the diffusiophoresis effect. Top and bottom solid arrows expresses the salt gradient and the generated electric field respectively. The curved arrows account for the diffusioosmosis and electroosmosis fluxes near the colloid surface, whereas the red arrow show the particle motion direction. Note that the diffuse layer thickness of the colloid particle depend on the salt concentration.

The diffusiophoretic velocity (v) of a particle due to a solute gradient can be written as [57],

$$v = \mu_p \nabla \ln n, \quad (1.4)$$

where (μ_p) is the diffusiophoretic mobility and (n) is the salt density.

The electrophoresis effect, describes the motion of charged particles under the effect of an electric field. This process is used for the migration and separation of charged particles, under the influence of an electric field [58]. This technique based on ion displacement has many applications in biology, chemistry and molecular biology.

Technically the separation can be realized, by means of two electrodes of opposite charge connected to an electrolyte solution, the separation of the ionic particles results from differences in their velocity (v), which is the product of the particle's mobility (μ)

and the electric field (E) [58],

$$v = \mu_E, \quad (1.5)$$

where μ is the electrophoretic mobility, for a particle with a radius much greater than the Debye length. The electrophoretic mobility is simply given by the Smoluchowski formula,

$$\mu = \frac{\epsilon\zeta}{\eta}. \quad (1.6)$$

All these processes are widely investigated previously by both theoretical and experimental approaches. In the following chapters we will elucidate some of them, through the mathematical description of the fluxes generated from the transport of the flow, salt and the diffuse layer contents.

1.4 Confinement with an open geometry!

Unlike the common investigations on the transport phenomena, in a confining structures made of two finite flat plates [59]. In the present work we use an open geometry made of a sphere moving either perpendicular (squeezing motion) or parallel (sliding motion) to a fixed flat substrate. Experimentally this open geometry can be realized by a sphere mounted on the cantilever of an Atomic Force Microscopy (AFM) [60], and a substrate made of mica. See appendix (7.3) for more details.

The sphere motions squeezes the sample against the substrate, generating a radial gradient of pressure $\nabla_r P$ which drags the sample contents inducing a liquid current combined to the charge current. The liquid and charge transport are at the origin of several electrokinetic phenomena.

In this work we deal also with the electrokinetic phenomena, resulting from the advection of the salt contained in the electrolyte solution, through the motions of the AFM sphere. We define the salt density simply by the sum of the coions and counterions densities.

In the open geometry, the salt density of the electrolyte solution advected under the effect of $\nabla_r P$ in the lubrication zone, where the sample width h is much smaller than the sphere radius R (further details on this approximation are given in chapter 3) can be subject to exchanges by mean of diffusion with the outer zone (reservoirs), where the lubrication approximation is no longer applicable as shown in the figure below.

Our approach consists in studying the salt density divination between the lubrication and reservoirs zones, to see whether the salt profile remains in the equilibrium state under the effect of $\nabla_r P$ or not. If it remains in the equilibrium state then Poisson Boltzmann equation can provide a complete description of the salt density variations.

If the salt density density is found to be in a non-equilibrium state, we call upon the continuity equation which describe the salt density variations between the lubrication zone and the reservoirs tp determine the effective derivation, i.e the resolution of the salt continuity equation coupled to the salt current generated from the sphere vibrations in order to determine the effective quantity of salt present in the lubrication area in the steady state.

The continuity equation reads as,

$$\partial_t n + \nabla \cdot j_s = 0, \quad (1.7)$$

where n is the salt density, ∂_t refers to the time derivative and j_s is the salt current density which can be generally given by,

$$j_s = -D\nabla n + nv + \mu neE, \quad (1.8)$$

with $D = \mu k_B T$ is the diffusion coefficient, v refers to the velocity profile of the fluid resulting from the upper sphere motions, the third term refers to the conduction of the salt density by the coulomb force generated from the charge density advection, μ is the mobility.

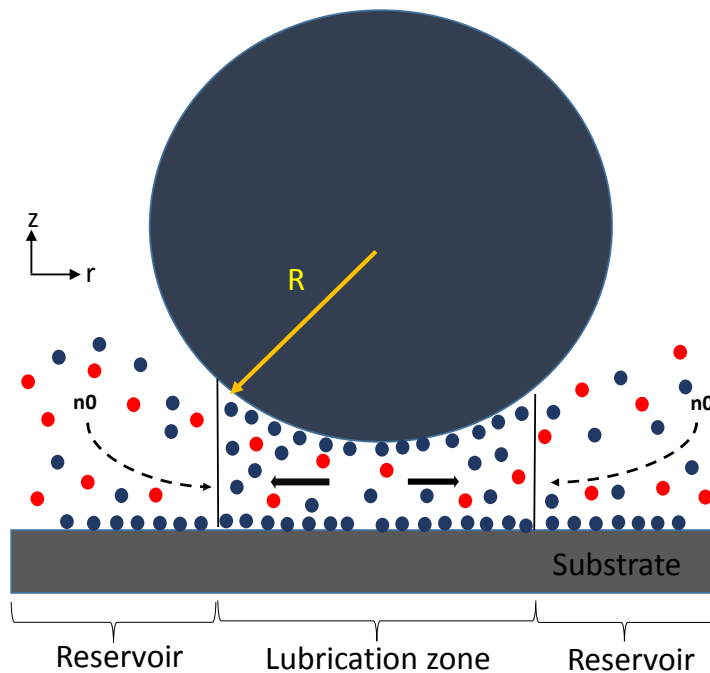


Figure 1.6: Schematic illustration of the salt exchanges between lubrication zone and reservoirs. solid arrows express the salt advection out the lubrication zone whereas the dashed arrows refer to the salt diffusing from the reservoirs to the lubrication zone.

Unlike the salt density profile, the charge density profile remains always in its equilibrium state. Due to the significant electrostatic interactions which take place between the sample and the solid surfaces. Thus the liquid flow induced by the sphere motions displaces a small quantity of charge $\delta\rho$ from the charge density profile ρ defined by the difference between the counterions and the coions densities.

The advected quantity $\delta\rho$ is brought back very quickly to the charge profile to restore the equilibrium state, by means of a high radial electric field resulting from $\delta\rho$ advection, in order to ensure the surface charge density screening. The continuity equation for the charge density takes the form,

$$\partial_t \rho + \nabla \cdot j_c = 0, \quad (1.9)$$

where ρ is the charge density made basically of counter ions and j_c is the charge density current defined in the same way as the salt density current.

$$j_c = -D\nabla \rho + \rho v + \mu v e E. \quad (1.10)$$

1.5 Sphere-plane relative motion

In the previous section, we have given a global overview of the confinement geometry employed in our investigation. In this section we give a detailed description of the relative motions between the sphere and the substrate, in particular the squeezing and sliding motions and their effects on the sample content, followed by a qualitative description of the couplings between the liquid and the charge currents, as well as the different effects resulting from this coupling.

1.5.1 Squeezing motion

Consider a sample of a weak monovalent electrolyte solution containing just two species of ions, having the charge $+z_1q$ and $-z_2q$ respectively (with $z_1 = -z_2$ the ions valency and q is the elementary charge), confined between a substrate and the lower surface of a vibrating sphere. The film width, the radius of the sphere and its velocity are referred to as h_0 , R and V respectively, where $h_0 \ll R$ as shown in the figure below.

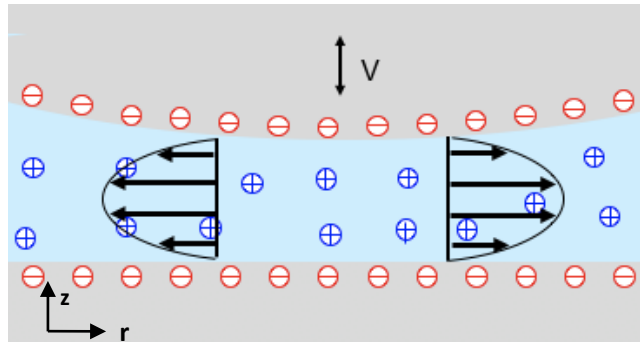


Figure 1.7: Schematic view showing the squeezing motion of the diffuse layer. V expresses the sphere vibrations velocity in the normal direction, whereas the black arrows account for the velocity profile resulting from squeezing out the sample film.

The vertical motion of the sphere squeezes the incompressible electrolyte film onto the substrate, generating a gradient of pressure ∇P which give rise to a liquid flow as well as a charge flow in the radial direction. The electric field established from the counterions advection generate an electroosmotic back flow which decreases the forward liquid flow.

The decay in the forward flow can be interpreted as an enhancement of the medium viscosity caused by the diffuse layer perturbations. This effect widely known as the first effect is at the origin of the electroviscous damping enhancement [61,62].

For separations of few nanometers the "viscoelectric" effect (second effect) which expresses the viscosity dependence on the electric field may enhance also the dynamic viscosity. Hsu et al in a recent work showed that the decrease on both electroosmotic mobility and the conductance at high charge concentrations arises from the viscoelectric effects [63–65].

Cox determined in his paper [66] the force exerted on a sphere moving in an electrolyte solution, with an approach based on a singular perturbation expansion using a parameter $\varepsilon \equiv (\lambda/L)$, where the sphere size L is much bigger then the diffuse layer thickness λ , with

a Peclet number of the order $\mathcal{O}(1)$. He showed that the distortion of the diffuse layer induces a tangential streaming potential combined to a pressure gradient.

According to Cox, the force induced from the streaming potential gradient within the diffuse layer combined to the pressure gradient, is the largest contribution to the electroviscous force with an order of $\mathcal{O}(\varepsilon^4)$. While he considered Maxwell's stress contribution $\mathcal{O}(\varepsilon^6)$ is negligible.

Schnitzer et al demonstrated in the thin limit that the Peclet number scales with λ^2 , meaning that this number cannot be around $\mathcal{O}(1)$. With their assumptions they found that the electroviscous force is of the order $\mathcal{O}(\varepsilon^2)$ and includes both Maxwell's stress and the viscous stress contributions [67,68].

Liu et al studied the hydrodynamic dumping enhancement, by measuring experimentally the viscosity enhancement due to Maxwell's and the viscous stresses, they developed a semi analytical model qualitatively in agreement with the measured data. Quantitatively they found a viscosity enhancement much larger than the experimental one [61].

1.5.2 Sliding motion

In the case of a sliding motion, the system remains the same except the fact that the sphere moves at a constant speed V without rotation in the direction parallel to the substrate, as shown in the figure(1.8).

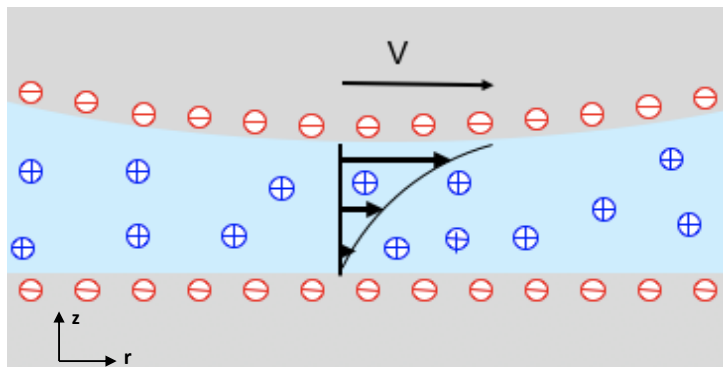


Figure 1.8: Schematic view of the sliding motion, V expresses the radial velocity of the sphere, whereas the black arrows account for the shearing profile derived from the sliding motion of the sphere.

The black arrows show the shear flow caused by the sliding motion between the sphere and the immobile substrate. This flow generates an electric field from the counterions advection.

The effect of the radial electric field on the sphere can be determined using Maxwell's stress tensor [69]. Knowing that the diagonal elements of the stress tensor are pressures and the off diagonals are shears, in the case of bidimension geometry, the electrostatic pressure acting in the normal direction on the AFM sphere expresses the lift force, which tends to derive away the sphere from the substrate. This effect is known as the electrokinetic lift force [70–72].

Bike and Prieve found inconsistencies between the experimental findings and their quantitative predictions on the electrokinetic lift force. According to their model the

theoretical lift force turns out to be weaker by orders of magnitude compared to the experimental observations.

They also showed that the lift force is inversely proportional to the fluid conductivity. From experiments made on pure glycerol and water/glycerol solutions, they demonstrated the fact that the electrokinetic lift force may reach significant values in some fluids characterized by lower conductivities [73, 74].

Cox showed in his 1997 paper, that significant values of the lift force can be measured assuming a Peclet number of $\mathcal{O}(\varepsilon^4)$. Where he found in the thin double layer limit a lift force of $\mathcal{O}(\varepsilon^4)$ ([66]).

Shnitzer et al based on their studies on the streaming potential phenomena in the thin Debye layer [67, 68, 75]. They revisited Cox's work and showed that the Peclet number scales with λ^2 and the lift force with $\mathcal{O}(\varepsilon^3)$ [76].

The discrepancy found between the calculated and measured lift force in Bike and Prieve work, is approved by the model proposed by Shnitzer et al, since both models underestimate the experimental lift force by orders of magnitude.

1.6 Thesis plan

This thesis deals with the electrical double layer in the out-of-equilibrium state, resulting from the confinement of an electrolyte solution between a substrate and a vibrating sphere mounted on an AFM. Our study is based on two aspects, the first is the squeezing motion where the sphere vibrates in the normal direction and squeeze out the sample against the substrate, and the second aspect is the sliding motion where the sphere moves parallel to the substrate.

The first chapter presents a general overview of the electric double layer, the electrokinetic phenomena and a detailed explanation of the squeezing and the sliding motions. In order to provide the reader with a basic understanding of the concepts related to small scale charge transport.

The second chapter is devoted to the electrostatic aspect of the electric double layer. We first derive the one dimensional Poisson Boltzmann equation used to describe the electrostatic potential in the gap between the surfaces. In a second step we give a detailed study on the effects of the boundary conditions on the electrostatic phenomena and as final step we derive the non-equilibrium thermodynamic force expression.

Chapter 3 deals mainly with the hydrodynamic aspect of the confinement. In this chapter we first give the Stokes equation that describes the variations of the velocity profile generated by the sphere vibrations, then we explain the legitimacy of using the well known lubrication approximation in our approach, and finally the general expression of the velocity components.

Chapter 4 is dedicated to the study of the non-equilibrium electrostatic double layer, through the charge-flow coupling. We first define the currents induced by the sphere motions. After that we calculate Onsager's coefficients analytically and numerically in the case of wide and narrow channels. Finally we calculate the electroviscous force as well as the lift force and compare them with the experimental findings.

Based on the discrepancy between the experimental findings and the theoretical predictions. We conclude in this chapter that the charge-flow coupling is insufficient to describe the electrostatic double layer in the non-equilibrium state.

Chapter 5 is similar to chapter 4. We have kept the same approach and we have performed the same calculations by including the salt density as a third element. The evaluation of Onsager's coefficients dependent on the salt, in the equilibrium state is irrelevant to interpret the experimental findings, given the discrepancy found between the experimental and the theoretical predictions of the electroviscous force.

From this preliminary result, we have realized the requirement of calculating Onsager's coefficients depending on the salt in the non-equilibrium state. Thus we give in the last chapter a theoretical model that can be relevant to calculate Onsager's coefficients depending on the salt in the non-equilibrium state.

Chapter 2

Electrostatics

Poisson Boltzmann equation is a widely used equation, for studying the electrostatic properties of biological macromolecules, physiological interfaces, as well as the distribution of electrons in plasmas and semiconductors.

This fundamental equation is used in our investigation, to define the electrostatic potential generated from the distribution of ions between the sphere lower surface and the substrate.

Poisson Boltzmann equation is a nonlinear equation derived from Poisson's equation, which relates the electrostatic potential variations to the charge density by mean of Boltzmann distribution [77, 78].

2.1 Poisson Boltzmann mean field theory

It is practically unfeasible mathematically, to find an analytical solution that describes all the electrostatic interactions between the ions in the diffuse layer.

The Mean field theory (MFT), assumes that all the ions interactions can be approximated by the interaction of an ion with a mean electrostatic field, resulting from the average spatial distribution at thermodynamic equilibrium of all ions [79, 80]. In other words the MFT theory reduces a multibody system to a one body system, this approximation is valid when a given ions has many random interactions which tend to cancel out each other.

The well known Boltzmann distribution for ions at the equilibrium state is given by,

$$n_{\pm} = n_0 \exp \frac{ze\psi}{k_B T}. \quad (2.1)$$

The ions density is a rapidly varying function of the electrostatic potential governed by Poisson equation,

$$\nabla^2 \psi = \frac{en_{\pm}}{\epsilon}, \quad (2.2)$$

where ∇^2 is the Laplace operator, which expresses the electrostatic potential variations in 3 dimensions, analytic solutions can be found for this partial differential equation under some specific conditions.

Combining Boltzmann distribution with Poisson's equation, yields the non linear Poisson Boltzmann equation which links the charges density distribution to the electrostatic potential [81],

$$\nabla^2 \psi = \frac{en_0}{\epsilon} \exp \frac{\pm e\psi}{k_B T}. \quad (2.3)$$

2.2 1D Poisson Boltzmann equation

Since we deal with an electrolyte solution, with two ionic species trapped between two surfaces in a bidimensional geometry. We retain only the potential variations in the normal direction to the surfaces which depend on z , assuming a constant potential in the radial direction according to r .

Equation (2.1) provide the distribution expression of the counterions n_+ as well as the co-ions n_- between the surfaces,

$$n_{\pm} = n_0 e^{\mp\phi}, \quad (2.4)$$

with the dimensionless potential $\phi = e\psi/k_B T$, and Boltzmann constant $k_B = 1.38 \times 10^{-23} \text{J.K}^{-1}$, T is the ambient temperature.

The resulting expressions for the charge density reads as,

$$\rho = e(n_+ - n_-) = 2en_0 \sinh \phi, \quad (2.5)$$

where n_0 is the bulk salinity.

Based on the assumptions given above Poisson Boltzmann equation in one dimension can be given by [31],

$$\frac{\partial^2 \phi}{\partial z^2} = \lambda^{-2} \sinh \phi, \quad (2.6)$$

where the Debye length λ expresses the diffuse layer thickness,

$$\lambda = \frac{1}{\sqrt{8\pi l_B n_0}}. \quad (2.7)$$

And l_B is the Bjerrum length,

$$l_B = \frac{e^2}{4\pi\epsilon k_B T}. \quad (2.8)$$

The Bjerrum length expresses the distance, at which the electrostatic potential energy for two elementary charges is equal to the thermal energy $k_B T$, for water at room temperature $l_B \sim 0.7 \text{nm}$.

2.2.1 Electrostatic potential for infinite half-space

Practically, the geometry of the infinite half-space can be realized by moving away one of the confining surfaces at sufficiently large distances (infinity), taking into account the electric double layer of a single surface (substrate for example) [21], as shown in the figure below,

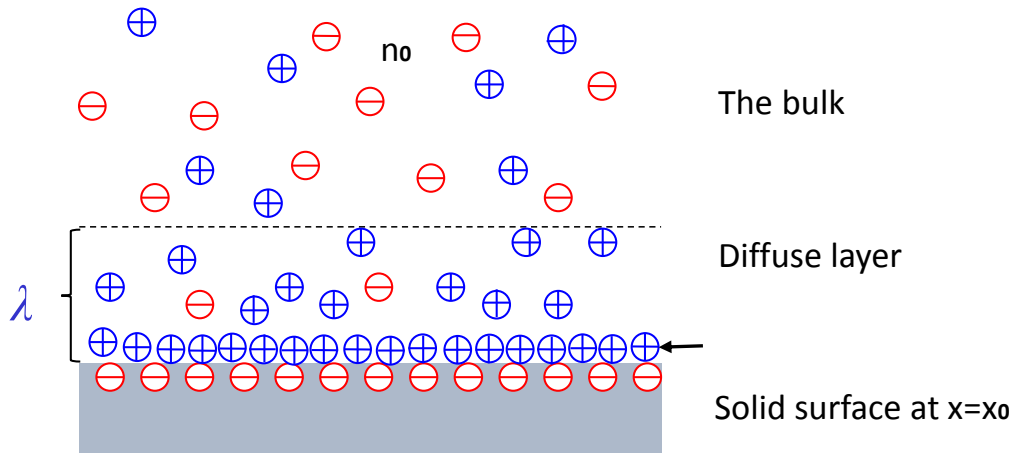


Figure 2.1: Schematic view of infinite half-space geometry, where the solid surface carries a charge density σ , the diffuse layer thickness is equal to λ and the bulk salinity to n_0 .

To determine the analytic expression of the electrostatic potential at an infinite half-space, one can use the constant charge boundary condition (CC),

$$\left. \frac{\partial \phi}{\partial z} \right|_{z=0} = \frac{\sigma}{\epsilon}. \quad (2.9)$$

For a monovalent electrolyte solution, the integration of Poisson Boltzmann equation (2.6) yields the analytic expression of the electrostatic potential,

$$\phi(z) = -2 \ln \left(\frac{1 + \gamma e^{-z/\lambda}}{1 - \gamma e^{-z/\lambda}} \right). \quad (2.10)$$

For more details on the analytic expressions of ϕ and γ derivation see appendix (7.4).

The electrostatic field resulting from this potential can be determined, by a simple derivation of the expression (2.10) with respect to z , the derivation yields,

$$E_{\infty}(z) = \frac{4\gamma e^{z/\lambda}}{\lambda(e^{2z/\lambda} - \gamma^2)}, \quad (2.11)$$

where the integration constant γ is given by,

$$\gamma = \sqrt{\frac{b^2}{\lambda^2} + 1} - \frac{b}{\lambda}, \quad (2.12)$$

b is the well known Gouy Chapman length, which expresses the distance at which the thermal energy $k_B T$ is equal to the electrostatic potential energy, of a single charge interacting with a constant surface charge density σ [21]¹. This length is given by the ratio,

$$b = \frac{2\epsilon k_B T}{e\sigma} \quad (2.13)$$

$$= \frac{e}{2\pi l_B \sigma}, \quad (2.14)$$

¹ $e\sigma/2\epsilon$ expresses coulomb interaction, between the single charge and the charge density σ .

b is inversely proportional to the charge density σ , for strongly charged surfaces b is only few angstroms,

Knowing the electrostatic potential expression, one can readily calculate the densities of co-ions and counterions by applying Boltzmann distribution (2.4),

$$n_{\pm} = n_0 \left(\frac{1 \pm \gamma e^{-z/\lambda}}{1 \mp \gamma e^{-z/\lambda}} \right)^2. \quad (2.15)$$

Note that this expression is valid, to describe the total electrostatic potential generated from one surface. Equation (2.10) will be used afterwards to describe the electric double layers confinement at distances very large compared to the Debye length, where the electrostatic potential generated from the surfaces does not overlap.

The figure (2.2) shows the variations of n_+ and n_- densities as a function of z . One can notice that the counter ion density is dominant for small distances, this dominance can be attributed to the screening effects that ensure the solid surface screening. For quite large distances the densities of co-ions as well as the counterions equal to the bulk density n_0 .

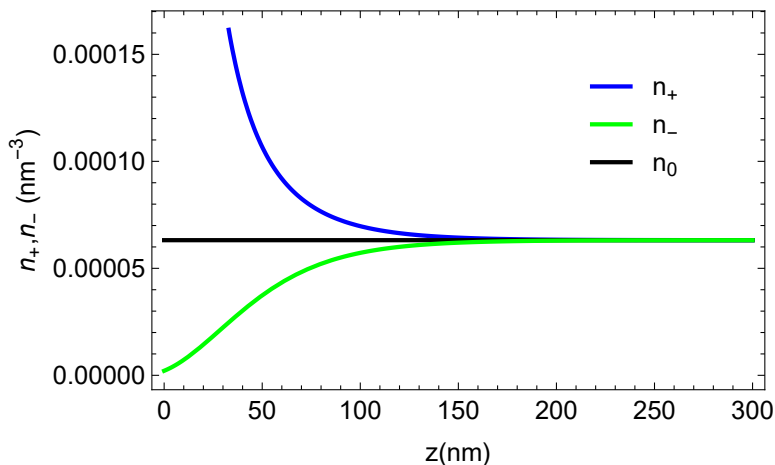


Figure 2.2: Plot of coions n_- and counterions n_+ profiles as a function of z on a linear scale. In the framework of infinite half-space geometry, with a surface charge density $\sigma = 0.02\text{nm}^{-2}$ and a diffuse layer thickness $\lambda = 30\text{nm}$.

2.2.2 Electrostatic potential in a narrow channel

As we mentioned in the introduction, it is paramount to study the electric double layers in a narrow channel, where the thickness of the water film confined between the surfaces is equal or smaller than Debye length $h \leq \lambda$. In this approximation we consider that the two surfaces are located in the positions $z = -h/2$ and $z = h/2$ respectively.

When we confine the electrolyte solution on such distances, new effects emerges from the overlapping between the surfaces potentials, affecting the viscous as well as the electric proprieties of the electrolyte solution.

In order to establish the analytic expression of the electrostatic potential between close surfaces, the overlapping effect must be taken into account when solving the non linear Poisson Boltzmann equation, see appendix (7.5) for more details.

The solution of Poisson Boltzmann equation (2.6) describing the electrostatic potential

between nearby surfaces is expressed in terms of Jacobi elliptic functions [82–84] as,

$$\phi(z, k) = \ln(k) + 2 \ln \left(\text{cd}(z, k) \right), \quad (2.16)$$

the first term depends on the parameter k , describing the finite value of the electrostatic potential at midplane $k = \exp(\phi(0))$, whereas the second term depends on both k and the vertical coordinates z through the function cd .

It is worthy to note that the parameter k depends implicitly on the channel height h , λ and σ , as shown in the figure (2.3),

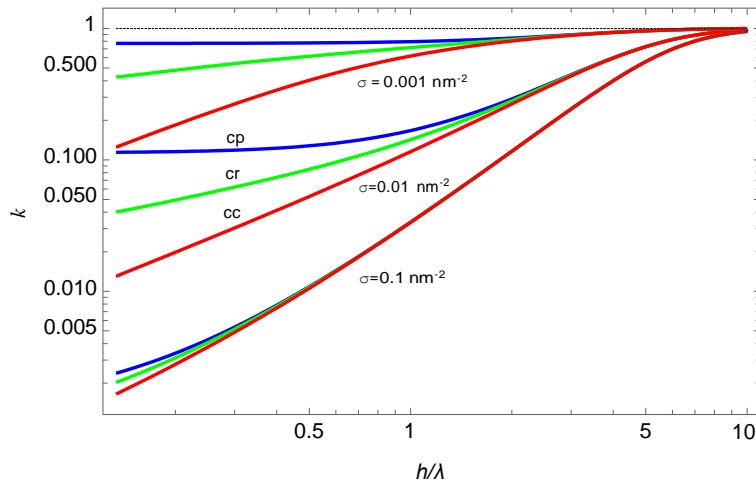


Figure 2.3: The parameter k variation as a function of the reduced height of the channel. The blue solid lines refers to the variations derived from (CP), whereas the green and the red expresses the variations derived from (CR) and (CC) respectively.

The parameter k is proportional to the channel height and inversely proportional to the surface charge density σ . From the figure above we can notice that, the boundary conditions (CC, CR and CP) are relevant only for very small heights.

The equation (2.16) can be evaluated only numerically except for very small separations, where Taylor's expansions can provide an analytic expression of $\phi(z, k)$.

The electrostatic field can be given simply, by the derivative of the electrostatic potential (2.16) with respect to z ,

$$E(z) = \frac{(k^2 - 1)nd(z, k)sd(z, k)}{\sqrt{k}\lambda\text{cd}(z, k)}, \quad (2.17)$$

using the electrostatic potential and Boltzmann distribution one can readily finds the densities of co-ions and counterions,

$$n_{\pm}(z, k) = n_0 e^{\mp\phi(z, k)}, \quad (2.18)$$

1- Channel with a fixed height

Consider an electrolyte solution confined in a narrow channel, made of two surfaces separated by a fixed height h , the channel is connected on its both ends to a reservoirs of salinity n_0 , as shown in the figure (2.4),

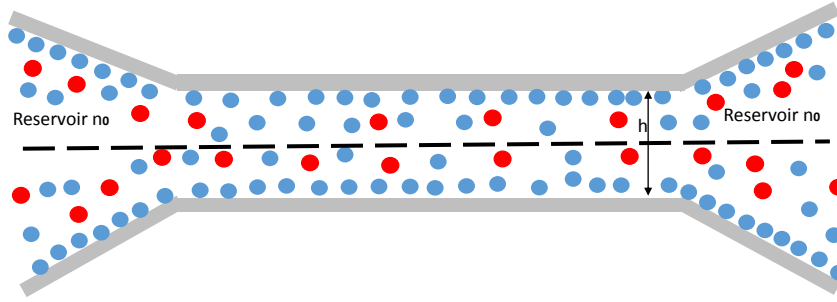


Figure 2.4: Schematic view of a narrow channel with a fixed height h , connected to two reservoirs. The dashed line expresses the midplane.

As discussed before, the electrostatic potential in the channel depends only on the vertical coordinate z , therefore it can be described using equation (2.16). At midplane the electrostatic potential as well as counterions and co-ions densities equals to,

$$\begin{aligned}\phi &= \ln k \\ n_{\pm} &= n_0 e^{\mp \ln k}.\end{aligned}\tag{2.19}$$

In the reservoir the densities $n_{\pm} = n_0$, whereas inside the channel at the midplane, the densities are slightly deviated from their densities in the reservoirs (2.19), yet this deviation is constant because the parameter k takes a constant value given that λ , σ as well as h are constants.

2- Sphere-plane geometry

Now let's consider an electrolyte solution confined between a sphere of a radius R and a substrate, as shown in the figure (2.5).

In the lubrication area for small angle θ , the channel width is a slowly varying function of the radial coordinate r , according to the Darjaguin approximation,

$$h(r) = h_0 + \frac{r^2}{2R},\tag{2.20}$$

with h_0 is the minimum value of the height, further details on this approximation are given in chapter 3.

Since the variations of h are very small in the lubrication zone, we can consider that the variations of the electrostatic potential in it, are similar to that of a narrow channel with a fixed height. i.e the electrostatic potential depends only on the vertical coordinate z and it is described by (2.16). Yet in the outer zone (reservoirs) (2.16), is no longer applicable, except at the midplane where the electrostatic potential equal to zero $\phi = 0$, given $k = 1$ in this region, see figure (2.3).

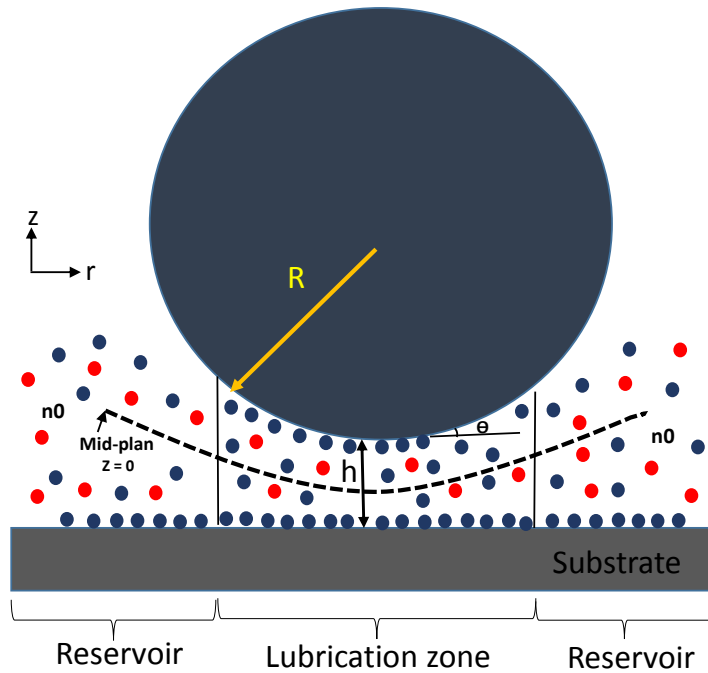


Figure 2.5: Schematic view of the open geometry. The blue circles refers to the counterions whereas the red circles refers to the co-ions. The film height h is a slowly varying function of the radial coordinate r .

Note that the electrostatic potential, as well as the counterions and co-ions densities (2.19) varies along the midplane, these variations are expressed through the parameter k dependency on the film height h . Nevertheless these variations remains weak at the equilibrium state where the chemical potential is equal to zero.

2.3 CC, CP and CR boundary conditions

For quite simple geometries, analytical solutions for the nonlinear Poisson Boltzmann equation can be found, relying on boundary conditions which represent a major key to the derivation of the electrostatic potential analytical expression.

The boundary conditions, constant charge (CC), constant potential (CP) and charge regulation (CR), are the most commonly used boundary conditions, in the studies which involve around the electrostatic phenomena at the interfaces.

2.3.1 Constant charge boundary condition (CC)

Constant charge boundary condition is effective, when both solid surfaces carries a uniform surface charge σ , which remains constant for all the inter-surfaces separations. In this specific case the potential is not constant and the electric field on the negatively charged solid surfaces situated at $z = 0$ and $z = h$ satisfies,

$$\left. \frac{\partial \phi}{\partial z} \right|_{z=0,h} = \mp \frac{\sigma}{\epsilon}. \quad (2.21)$$

Figure (2.6) shows the variations of the normalized profiles of $n_{\pm}(z)$, $\rho(z)$, the potential ϕ as well as the electric field E , as a function of z .

The quantity of co-ions is very small compared to counterions especially in the vicinity of the plates, this distribution is expected since the counterions of the diffuse layer, screens the negative charge σ of the surfaces. At sufficiently large distances from the walls both n_{\pm} are equal to the bulk density n_0 .

The charge density profile defined as $\rho = n_+ - n_-$, is basically made of counterions and tend to zero in the bulk region, the integration $\rho(z)$ over z yields 2σ .

Since the electrostatic potential depends on the distribution of counterions in the diffuse layer, we notice similar variations between ϕ and ρ (2.6). Note that the potential is derived from the superposition of the potentials of both surfaces, this approximation remains valid as long as there is no overlap between the potentials.

The electric field reach its maximum close to the surfaces and tend to zero in the bulk region where the liquid medium is neutral.

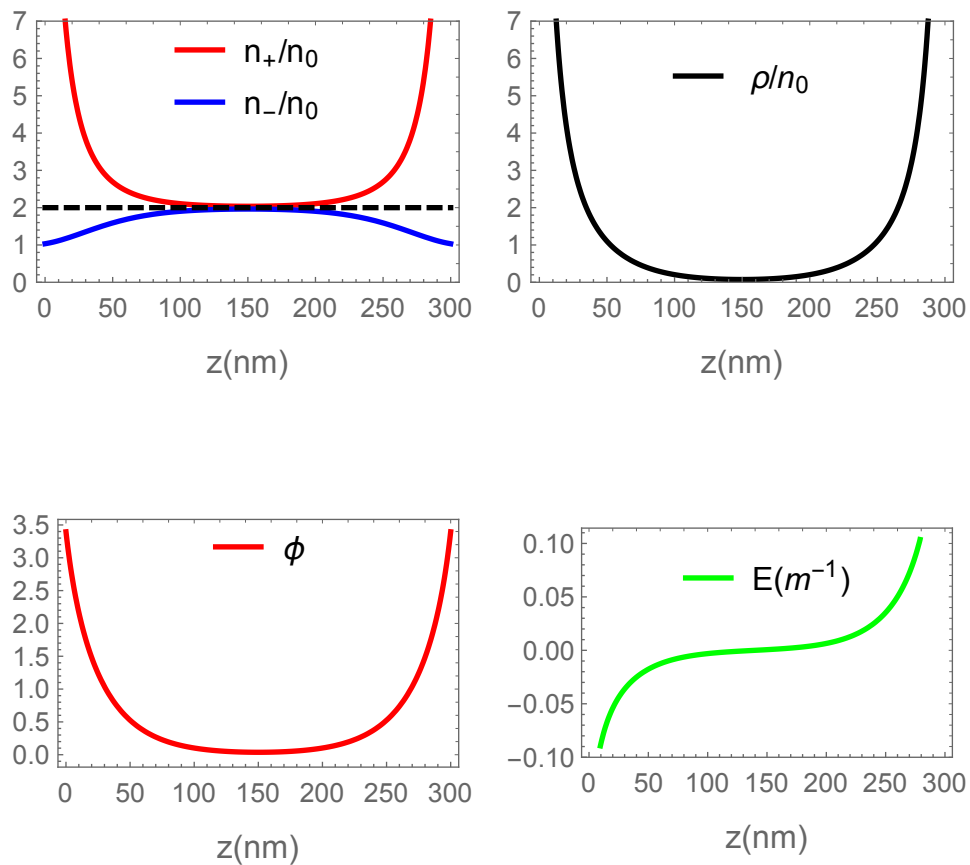


Figure 2.6: Plot of the normalized profiles of $n_{\pm}(z)$ and $\rho(z)$ (up), the electrostatic potential and the electric field variations as a function of z (down), for an univalent electrolyte solution between two negatively charged surfaces. The calculations for this curves are performed using (CC) boundary condition with $\sigma = 0.02\text{nm}^{-2}$.

2.3.2 Constant potential boundary condition (CP)

Constant potential boundary condition (CP) [85], is effective when both solid surfaces carries a fixed electrostatic potential which satisfies,

$$\phi(\pm h/2) = \phi_0, \quad (2.22)$$

where ϕ_0 is the electrostatic potential value at the interface. For (CP) the surface charge density varies with the separation distance between the surfaces h .

The figure (2.7) shows the variations of the normalized charge density profile (CP) boundary condition, with the parameters $\lambda = 30\text{nm}$ and $\sigma = 0.02\text{nm}^{-2}$.

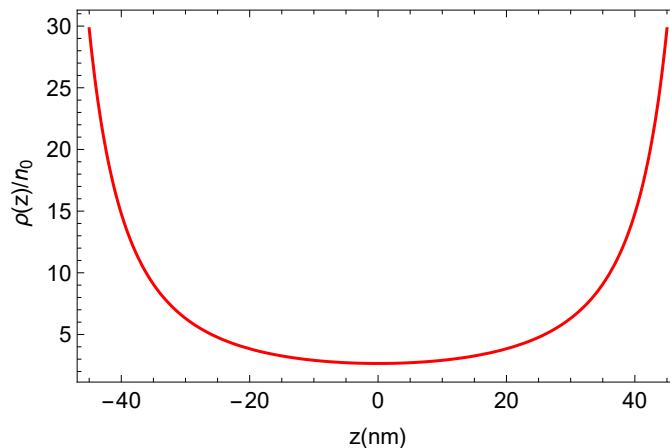


Figure 2.7: Plot of the normalized charge density profile as a function z , on a linear scale. The calculations are performed using (CP) boundary condition with $\phi_0 = -3.39$

2.3.3 Charge regulation boundary condition (CR)

In most cases, the ionizable sites on the surface are not fully dissociated, therefore absorption reactions come into play making the surface charge density and the surface potential varying [86,87]. If we consider that the protons can bind to acid groups HA, the equilibrium condition at the surface yields,



Expressing the proton concentration at the surface as $[\text{H}^+]$, the concentration of negative sites as $[\text{A}^-]$ and the undissociated sites as $[\text{AH}]$. One can define the surface dissociation constant as,

$$\begin{aligned} K_d &= \frac{[\text{H}^+][\text{A}^-]}{[\text{AH}]} \\ &= \frac{\alpha}{1 - \alpha} n_s, \end{aligned} \quad (2.24)$$

where α is the fraction of sites effectively dissociated, with $n_s = [\text{H}^+]_\infty e^{-\phi_0}$ the hydronium concentration at the surface, from equation (2.24) one readily find,

$$\alpha = \frac{1}{1 + n_s/K_d}. \quad (2.25)$$

For very large K_d , $\alpha = 1$ which means that none of the sites have been dissociated, therefore we recover the constant charge boundary condition (CC). For distances sufficiently far from the solid surface the results found in (CP) and (CR), converge towards the results found by (CC).

The surface charge density can be expressed as,

$$\sigma' = \frac{\alpha}{S}, \quad (2.26)$$

where the area per site S is defined in a way that for quite large distances $\sigma' = \sigma$.

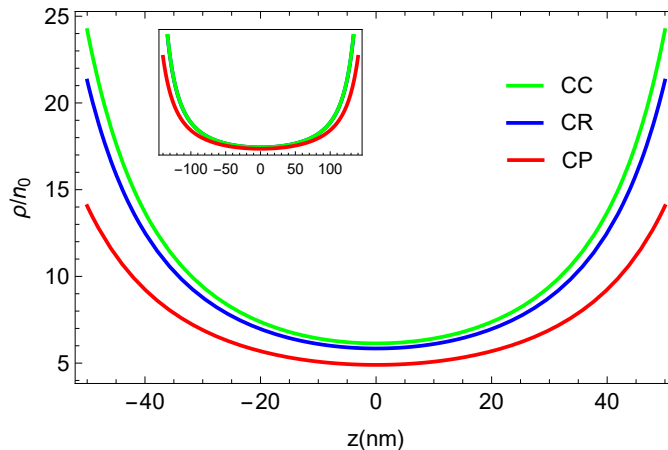


Figure 2.8: Charge density profile variations as a function z on a linear scale. For (CC), (CR) and (CP) boundary conditions with $\lambda = 60\text{nm}$, the surface charge $\sigma = 0.008\text{nm}^{-2}$, the dissociation constant $K_d = 10^{-3}$, $\text{pH} = 5$ and $pK = 3.6$. The inset shows the convergence between the curves far away from the surfaces.

Figure (2.8) shows the variations of the normalized charge density profile for different boundary conditions. It is obvious that the boundary conditions have an effect on the charge density only near the solid surfaces. For sufficiently far distances all the profiles converge (figure shown in inset).

(CC) boundary condition gives an overestimation of the effective charge density in the vicinity of the solid surface, whereas (CP) gives an underestimation of it. This is reasonable because in reality neither the potential nor the surface charge density remains constant. Therefore (CR) is the most relevant boundary condition which describes the exchanges at the solid-liquid interface permanently.

2.4 Out of equilibrium force

When we apply an external perturbations on the diffuse layer counterions (the sphere vibrations in our case), the electrostatic equilibrium occurs very quickly in the vertical direction, by means of ions diffusion, we can estimate the vertical relaxation time by,

$$\tau_z = \frac{h_0^2}{D}, \quad (2.27)$$

for a channel with a height $h_0 \sim 200\text{nm}$ and ions-diffusion coefficient $D \sim 10^{-9}\text{m}^2/\text{s}$, the relaxation time $\tau_z \sim 4 \times 10^{-5}\text{s}$ which is very small compared to the sphere vibrations $\omega_0^{-1} \sim 10^{-2}\text{s}$.

However in the radial direction the ions diffuse slowly. We define the relaxation time as the time required for the ions to recover their equilibrium state after perturbation, thus the radial relaxation time can be estimated by,

$$\tau_r = \frac{r^2}{D}, \quad (2.28)$$

r is the distance of the ion from its starting position at time t which can be approximated by $r \sim \sqrt{R h_0}$.

For $R = 47\mu\text{m}$ and $h_0 = 200\text{nm}$, one finds $\tau_s = 9.4 \times 10^{-3}\text{s}$. This value is comparable to ω_0^{-1} .

We define the out of equilibrium thermodynamic force as the variations of the free enthalpy with respect to the radial coordinate r as following,

$$f = -\nabla_r(g_+ + g_-), \quad (2.29)$$

where g is the chemical potential given by,

$$g_{\pm} = \pm e\hat{\phi} + k_B T \ln \hat{n}_{\pm}, \quad (2.30)$$

with $\hat{\phi}$ is the electrostatic potential and \hat{n}_{\pm} the ions densities in the out of equilibrium state,

$$\hat{n}_{\pm} = \hat{n}_0 e^{\mp \hat{\phi}}, \quad (2.31)$$

where \hat{n}_0 is an effective salinity given by $\hat{n}_0 = \sqrt{n_+ n_-}$. Both $\hat{\phi}$ and \hat{n}_0 depends on the deviation of the co-ions and counterions densities \hat{n}_{\pm} from their densities at the equilibrium state n_{\pm} .

Inserting (2.30) in (2.29) one readily gets the thermodynamic force,

$$X = -k_B T (\hat{n}_+ + \hat{n}_-) \nabla_r \ln \hat{n}_0 \quad (2.32)$$

In the quasi-static case, where the sphere vibrations are very small, it can be assumed that the deviation of the salt profile from its equilibrium state is relatively small. Therefore one can consider that $\hat{n}(z) \sim n(z)$ in the calculations afterwards. This assumption is the basis for the calculations carried out in chapter 5 which deals with the salt-charge-flow coupling.

Chapter 3

Hydrodynamics

Navier Stokes equation is differential equation widely used to describe fluid flows [88–90]. For the derivation of this equation, let's consider a Newtonian¹ and incompressible liquid. To describe fully our system we need first to the incompressibility condition given by,

$$\nabla \cdot \mathbf{v} = 0, \quad (3.1)$$

where \mathbf{v} is the velocity field vector.

And a second equation derived from the application of Newton' second law on a fluid particle,

$$\rho \left(\partial_t \mathbf{v} + \mathbf{v} \nabla \mathbf{v} \right) = \mathbf{f} - \nabla P + \eta \nabla^2 \mathbf{v}, \quad (3.2)$$

where ρ is the density of the liquid, η the dynamic viscosity, P is the hydrodynamic pressure modulated by the sphere oscillations. The left hand term represent the acceleration which consists of the time derivative of the velocity combined to a convective term $\mathbf{v} \nabla \mathbf{v}$. The right hand consist of the pressure gradient which is responsible for the fluid flow and a body force term \mathbf{f} and a viscous term.

3.1 Stokes equation

The linear stokes equation is derived from the general Navier Stokes equation, when the viscous forces in the system $\eta \nabla_z^2 v$ are assumed to be significantly greater than the inertial forces $\rho(\mathbf{v} \cdot \nabla) \mathbf{v}$. This assumption is applicable for fluids characterized by a small Reynolds number ($Re \ll 1$), a number which expresses the nature of the flow regime [91]. It can be defined as,

$$Re = \frac{vr}{\eta}, \quad (3.3)$$

with v is the fluid velocity and r expresses the flow range in the lubrication area.

The velocity variations with time are negligible since the liquid medium is viscous. All this approximations are linked to the creeping flow approximations, used to study sphere the flows resulting from an immersed in a fluid [91]. Applying this approximation to (3.2) yields,

$$\eta \nabla^2 \mathbf{v} = \nabla P - e\rho E + n(z)X, \quad (3.4)$$

¹A Newtonian fluid, is a fluid in which the viscous stresses arising from its flow are at every point linearly correlated to the local strain rate.

where $e\rho$ is the charge density, E is the radial electric field established from the charge density advection and X is the thermodynamic force.

The source term in (3.4) consists of a pressure gradient ∇P which give rise to the liquid flow, that carries a long with it the charge and salt densities. The Coulomb force $e\rho E$ resulting from the interaction between the charge density and the radial electric field, and the thermodynamic force.

Reynolds was the first who treated the liquid flow confined between two surfaces, for the case of an open geometry made of a flat substrate and a sphere [82, 83].

3.2 Lubrication approximation

Lubrication approximation is used in fluid dynamics to describe the flow of a fluid in a geometry, in which one dimension is significantly smaller than the other. i.e the thickness of the liquid film separating the two surfaces is very small compared to the curvature radius of the sphere R and the flat substrate R_s .

Derjaguin developed a theory used to evaluate the force resulting from two interacting bodies, using their energy densities of interaction, multiplied by the effective radius of the two bodies [92, 93], for the case of an open geometry the effective radius is equivalent to the radius of the sphere $R_{eff} = R$, given the radius of the flat plate tends to infinity.

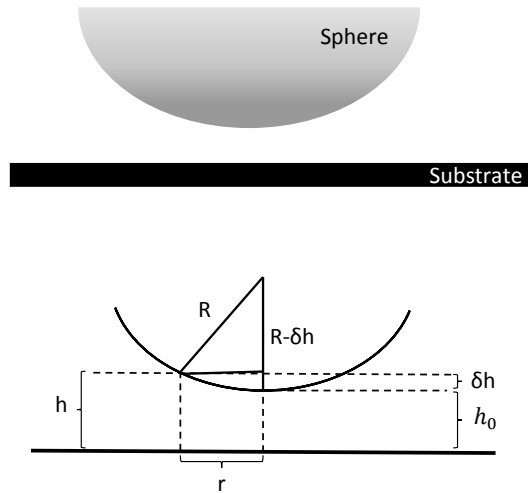


Figure 3.1: Schematic representation of the Derjaguin approximation for the sphere-plane geometry.

Figure (3.1), shows a schematic illustration of Derjaguin approximation, r designate the radial distance where the lubrication approximation is valid, h_0 refers to the minimum separation between the two bodies, h is the full separation and δh is the small variation of the separation h .

Using Pythagorean theorem, one can find that the separation $h(r)$ can be approximated by,

$$h(r) = h_0 + R - \sqrt{R^2 - r^2}, \quad (3.5)$$

Using Taylor expansion on the last term on (3.5), the separation $h(r)$ can be approximated by,

$$h(r) = h_0 + \frac{r^2}{2R} \quad (r \ll R), \quad (3.6)$$

$h(r)$ is a slowly varying function of the radial coordinate r , we can say that locally over a distance ($r \ll R$) the lower surface of the sphere and the substrate are parallel flat plates.

Performing the differentiation of $h(r)$ in (3.6) one finds,

$$Rdh = r dr, \quad (3.7)$$

this equation is used later on to evaluate the integrations, by changing the surface element $r dr$ by Rdh which is more convenient for the calculations.

Lubrication flow

The lubrication approximation has consequences on the flow of the electrolyte solution between the substrate and the sphere. More precisely on the velocity components as well as the forces in the radial and vertical directions [94].

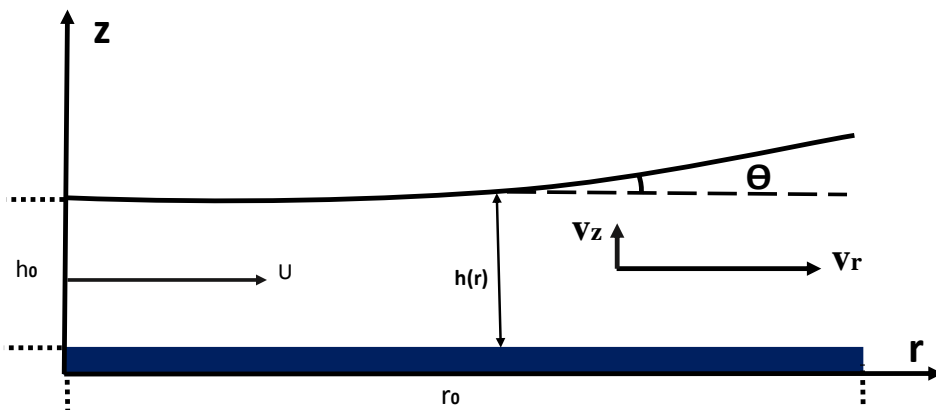


Figure 3.2: Schematic illustration of the lubrication flow.

The equation (3.4) projection with respect to (r) and (z) yields,

$$\eta \left(\frac{\partial^2 v_r}{\partial r^2} + \frac{\partial^2 v_r}{\partial z^2} \right) = -\frac{\partial P}{\partial r} - e\rho E_r - n(z) \frac{\partial X}{\partial r} \quad (3.8)$$

$$\eta \left(\frac{\partial^2 v_z}{\partial r^2} + \frac{\partial^2 v_z}{\partial z^2} \right) = -\frac{\partial P}{\partial z} - e\rho E_z + n(z) \frac{\partial X}{\partial z}, \quad (3.9)$$

for (3.8) and (3.8) one must add the mass conservation equation for an incompressible liquid,

$$\nabla \cdot v = 0 \quad (3.10)$$

$$\frac{\partial v_r}{\partial r} + \frac{\partial v_z}{\partial z} = 0. \quad (3.11)$$

Since the flow is laminar within the lubrication region, we can consider that the angle between the velocity vector and a flow line is very small ($\theta \ll 1$),

$$\tan \theta \sim \theta \sim \frac{v_z}{v_r} \quad (3.12)$$

$$v_z \sim v_r \theta \sim U \theta, \quad (3.13)$$

given the slow variation of the height $h(r)$ with respect to r in the lubrication area. The velocity components variations with respect to z can be approximated by,

$$\frac{\partial v_r}{\partial z} \sim \frac{U}{h_0} \quad (3.14)$$

$$\frac{\partial v_z}{\partial z} \sim \frac{U \theta}{h_0}, \quad (3.15)$$

where U is the velocity. Using (3.11) and (3.13) one can deduce the variations of v_r with respect to r ,

$$\frac{\partial v_z}{\partial z} = -\frac{\partial v_r}{\partial r} \sim \frac{U \theta}{h_0}. \quad (3.16)$$

For the second derivative of the velocity components with respect to z one readily gets,

$$\frac{\partial^2 v_r}{\partial z^2} \sim \frac{U}{h_0^2} \quad (3.17)$$

$$\frac{\partial^2 v_z}{\partial z^2} \sim \frac{U \theta}{h_0^2}. \quad (3.18)$$

For the second derivative of the velocity components with respect to r we take $\partial_r \sim 1/r_0$, therefore,

$$\frac{\partial^2 v_r}{\partial r^2} \sim \frac{U \theta}{h_0 r_0} \quad (3.19)$$

$$\frac{\partial^2 v_z}{\partial r^2} \sim \frac{U \theta}{r_0^2}, \quad (3.20)$$

the terms given in (3.19) and (3.20) are very small compared to the terms related to the second derivatives with respect to z (3.17) and (3.18), therefore we can neglect them [91].

We neglect also the term depending on θ in (3.18) compared to (3.17), since θ is assumed to be very small $\theta \ll 1$. Thus one retains from the velocity components only the term $\partial^2 v_r / \partial z^2$.

Regarding the forces, it is trivial that $\partial X / \partial z = 0$ for the thermodynamic force, whereas E_z is negligible, given the significant electrostatic interactions in z direction.

3.3 1D Stokes equation

Taking into account the approximations given above. In a stationary regime the velocity profile of the incompressible electrolyte solution flow, in the lubrication area satisfies the 1D Stokes equation given by,

$$\eta \partial_z^2 v = \partial_r P - e \rho E + n(z) X, \quad (3.21)$$

with $v \equiv v_r$. We work in the linear regime, which allow us to write the solution of the equation (3.21) as the sum of three components, a pressure driven term $v_p(z)$, electroosmotic term $v_E(z)$ and a diffusioosmotic driven term $v_s(z)$ [95].

3.4 Velocity profile components

In the lubrication area we can assimilate the lower sphere surface, as a flat solid surface situated at $z = h/2$ and the immobile substrate surface at $z = -h/2$, this geometry is privileged just for convenience. The velocity profile components are derived from the double integration of the Stokes equation taking into account the appropriate boundary conditions for each component.

3.4.1 Pressure driven velocity

The first component is the pressure driven velocity obtained from (3.21), taking into account just the liquid and discarding both the charge and salt densities, by setting both E_r and X equal to zero,

$$\eta \partial_z^2 v_p = \partial_r P, \quad (3.22)$$

equation (3.22) links the second derivative of the velocity profile to the force $\partial_r P$. Meaning that the determination of the velocity profile requires the performance of a double integration based on an adequate choice of boundary conditions. The first integration gives the variations of the shear stress τ_{zr} , which we consider null at the midplane of the channel, where the velocity profile reaches its maximum value $v(0) = v_{max}$,

$$\tau_{zr} = \eta \partial_z v_{max} = 0, \quad (3.23)$$

this condition is a result of the velocity profile symmetry, imposed by the non slip condition on the two surfaces $v(\pm h/2) = 0$, performing the integration one readily finds,

$$v_p(z) = \frac{\partial_r P}{\eta} \int_z^{h/2} dz' \int_0^{z'} dz'' \quad (3.24)$$

$$= -\frac{h^2 - 4z^2}{8} \frac{\partial_r P}{\eta}. \quad (3.25)$$

This integration yields the Poiseuille profile $p(z)$, which causes the salt and charge advection [96]. Figure (3.3) shows the Poiseuille profile $p(z)$ variations,

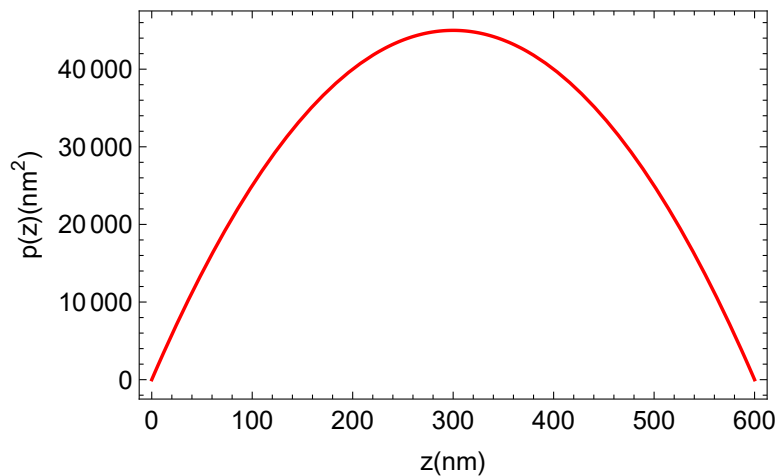


Figure 3.3: Poiseuille profile $p(z)$ variations as a function of the height z , on a linear scale.

3.4.2 Electroosmotic velocity

The second component in the velocity field is the electroosmotic velocity $v_E(z)$, which describe the profile resulting from the diffuse layer content distribution. This velocity can be derived from (3.21) by taking both ∇P and X equal to zero,

$$\eta \partial_z^2 v_E = \rho e E. \quad (3.26)$$

The integration is carried out in the same way as the previous case of the pressure driven velocity, the particularity in this case lies in the charge density ρ which we describe by mean of Poisson equation.

We carry out a double integration, considering the shear stress condition at midplane as well as the non slip boundary condition ($v(\pm h/2) = 0$) one finds,

$$v_E(z) = \int_z^{h/2} dz' \int_0^{z'} \rho(z'') dz'' \frac{eE}{\eta} \quad (3.27)$$

$$v_E(z) = f(z) \frac{eE}{\eta}, \quad (3.28)$$

the electrophoretic mobility in equation (3.28) can be reexpressed as,

$$f(z) = \epsilon(\psi(z) - \zeta), \quad (3.29)$$

where the electrophoretic mobility $f(z)$ describe the motion that ions exhibit as a result of them experiencing the electric field.

For a channel with a height h very large, we recover the Smoluchowski electrophoretic mobility $f(z) = -\phi_0/4\pi l_B \eta$ [97].

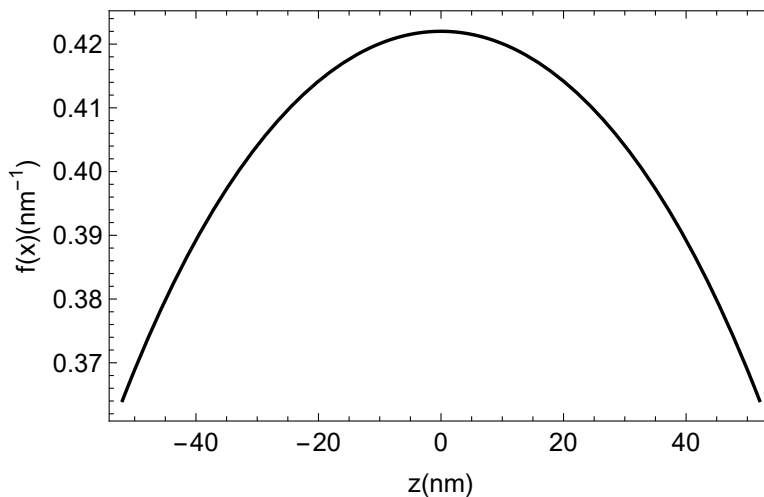


Figure 3.4: Electrophoretic mobility profile variations as a function of z , on a linear scale. The profile is calculated in a symmetric geometry using (CC) boundary condition with $\sigma = 0.02 \text{nm}^{-2}$. The thickness of the diffuse layer $\lambda = 30 \text{nm}$.

3.4.3 Diffusioosmotic velocity

The last component is the diffusioosmotic velocity, which is delicate to determine since it is related to the diffusion osmosis phenomenon. This component describe the profile

produced from the salt density distribution, derived from (3.21) by taking both ∇P and E_r equal to zero.

For an electrolyte solution confined between uncharged surfaces, the salt content diffuses in the radial direction in a homogeneous way and does not drag the liquid along with it. However in the case of charged surfaces, the interaction potential between the salt in the radial direction and the surfaces creates an inhomogeneity in the salt density.

Close to the surfaces the salt density is greater than the midplane density, which corresponds to the density between uncharged surfaces. The difference between the salt gradient in the two region generate a liquid flow (diffusioosmosis).

The midplane salt density can be considered as an inert density, since it does not carry any liquid, therefore it should be subtracted from the total salt profile $n_t(z)$ and we write $n(z) = n_t(z) - n(0)$, with $n(0)$ the salt density at midplane.

The diffusioosmotic velocity yields from the double integration of the equation,

$$\eta \partial_z^2 v_s = n(z)X, \quad (3.30)$$

unlike the electroosmotic velocity profile, the establishment of a general analytic expression for the diffusioosmotic velocity $v_s(z)$, which remains valid for small and large separations between the surfaces is impossible. The salt density can not be linked to the electrostatic potential as in the case of the electroosmotic velocity where the charge density was described by Poisson's equation.

In the quasi-static case, we calculate the velocity from the effective salt density at the equilibrium state, thus the diffusioosmotic velocity profile can be expressed as,

$$v_s(z) = \frac{H(z)}{\eta}X, \quad (3.31)$$

where $H(z)$ is the diffusiophoretic mobility [98], which describes the motion that ions exhibit as a result of them experiencing the salt gradient, this profile is readily calculated by performing the double integration of the salt density, taking in account the shear stress condition $\partial_z n = 0$ and the non slip boundary conditions,

$$H(z) = \int_z^{h/2} dz' \int_0^{z'} dz'' n(z''), \quad (3.32)$$

with,

$$n(z) = n_t(z) - n(0), \quad (3.33)$$

with $n(0)$ the inert salt density at midplane, for two surfaces sufficiently distant this quantity equal to the bulk salinity n_0 . Figure (3.5) shows the variations of the diffusiophoretic mobility as a function of the separation distance z .

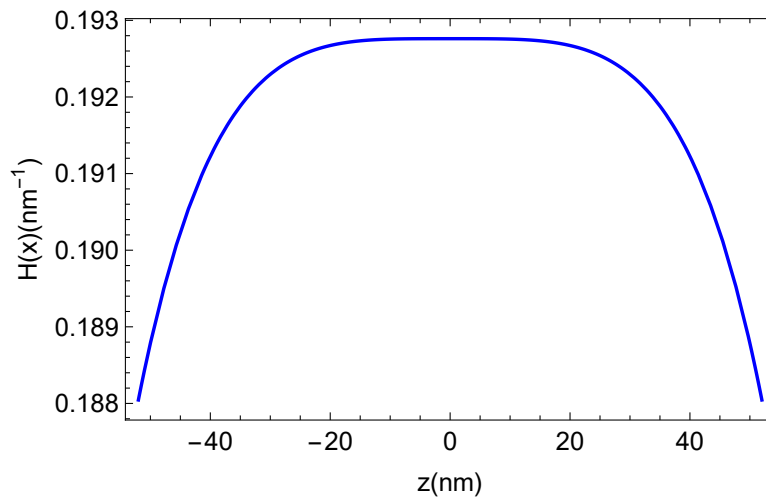


Figure 3.5: Diffusiophoretic mobility profile variations as a function of z on a linear scale. The profile is calculated in a symmetric geometry using (CC) boundary condition with $\sigma = 0.02\text{nm}^{-2}$. The thickness of the diffuse layer $\lambda = 30\text{nm}$

Further details on the velocity profile components are given in the appendix (7.6).

Chapter 4

Charge- flow coupling

We know that the sphere motions induces a volume current J_v , as well as a charge current J_c from the advection of the diffuse layer content. In this chapter we aim to characterize the coupling between these two currents, by studying the effect of this coupling, on the electroviscous force as well as the electrokinetic lift force.

4.1 Irreversible processes and linear laws

In thermodynamics, the concept of irreversibility refers to processes in which the changes in the thermodynamic state of a system and its environment, cannot be restored to their initial state by infinitesimal modifications without expenditure of energy.

To deal with irreversible processes in systems, with perturbations not too important compared to the state of equilibrium, the system may break down into small subsystems where each subsystem is assumed to be in local equilibrium and can be treated as an individual thermodynamic system, characterized by small number of equilibrium variables.

Onsager transport equations provide linear relations between the fluxes and the forces which generates it, this linearity is widely investigated and proved experimentally in a wide variety of different irreversible processes.

For a complete set of n fluxes and forces, which characterize several irreversible processes that occur simultaneously, Onsager's equations take the following form [99–102],

$$J_i = \sum_{j=1}^n L_{ij} \Upsilon_j, \quad (4.1)$$

where Υ is the forces and L_{ij} are Onsager coefficients or transport coefficients which are independent of the forces, these coefficients can be written in matrix form (Onsager matrix \mathbf{L}).

Onsager matrix consists of diagonal coefficients L_{ii} that link the forces to their conjugated flows, e.g an applied electric field on an electrolyte solution generate a coulomb force $e\rho E$ that induces a charge flow (conjugate flow).

The off diagonals elements L_{ij} relate the forces to the non conjugate fluxes. Taking the above example if we apply now, to the electrolyte solution a gradient of pressure, the charge advection by this latter force contributes to the charge flow generation (non conjugate flow).

Onsager added a significant concept on the theory of irreversible thermodynamics which rely on the symmetry of the phenomenological coefficients,

$$L_{ij} = L_{ji}, \quad (4.2)$$

these relations are called the Onsager reciprocal relations which are verified experimentally.

The charge-flow coupling can be studied from the coefficients linking the charge and volume currents J_c and J_v to the forces ∇P and eE .

4.2 Volume and charge currents

The sphere motions generates two kinds of currents, a volume current J_v induced from the radial pressure gradient ∇P acting on the liquid. Associated to a charge current J_c resulting from the advection and the conduction of the diffuses layer counterions by ∇P and the radial force $e\rho E$ respectively.

As we discussed earlier these currents can be described by Onsager's linear equations, as a consequence the transport coefficients which relates them to the forces can be written in a matrix form as,

$$\begin{pmatrix} J_v \\ J_c \end{pmatrix} = \begin{pmatrix} L_{vv} & L_{vc} \\ L_{cv} & L_{cc} \end{pmatrix} \begin{pmatrix} -\nabla P \\ eE \end{pmatrix}. \quad (4.3)$$

The diagonal elements L_{ii} connect each force with its conjugate flow, i.e, the radial gradient of pressure to the volume current and the force eE to the charge current, while the off diagonal elements L_{ij} determines the influence of the forces on a non conjugate flow, i.e, the influence of the ∇P on the charge current and the force eE on the volume current.

4.2.1 Volume current

The volume current rises from the velocity field integrated over the film width.

$$J_v = \int_{-h/2}^{h/2} v(z) dz, \quad (4.4)$$

where,

$$v(z) = v_p(z) + v_E(z). \quad (4.5)$$

In this section we deal with the charge-flow coupling, therefore we disregard the thermodynamic force in Stokes equation (3.4). Thus the velocity field profile consists of the pressure driven velocity profile $v_p(z)$ combined with the electroosmotic velocity profile $v_E(z)$.

For the sake of simplicity we consider that the electric mobility and the diffusion coefficients of coions and counterions are identical as a first approximation. Meaning that the conduction and the diffusion of the ions contained in the diffuse layer, are done in the same way in the radial direction regardless their positive or negative charge.

$$\mu_+ n_+ + \mu_- n_- = \mu(n_+ + n_-) = \mu n_t \quad (4.6)$$

$$D_+ n_+ + D_- n_- = D(n_+ + n_-) = D n_t. \quad (4.7)$$

Using the general analytic expression for $v_p(z)$ and $v_E(z)$ in (4.4) and performing the integral one obtains,

$$J_v = L_{vc} \frac{eE}{\eta} - L_{vv} \frac{\nabla P}{\eta}. \quad (4.8)$$

L_{vv} results from the integration of the velocity profile $v_p(z)$ (3.25), this latter coefficient describes the Poiseuille flow between two parallel surfaces. this coefficient relates ∇P to its conjugate flow J_v .

$$L_{vv} = \int_{-h/2}^{h/2} dz \frac{h^2 - 4z^2}{8} \quad (4.9)$$

$$= \frac{h^3}{12}. \quad (4.10)$$

L_{vc} describes the electroosmotic effect responsible for the liquid advection in the channel by mean of the radial electric field, this latter describes the contribution of the force eE to the volume current. It is calculated by integrating the electroosmotic velocity $v_E(z)$ (3.29) in (4.4),

$$L_{vc} = \int_{-h/2}^{h/2} f(z) dz. \quad (4.11)$$

The relation (4.8) is closed by the incompressibility condition between the volume current and the imposed velocity $V(t)$.

$$\frac{rV(t)}{2} - J_v = 0. \quad (4.12)$$

In the absence of the charge density the sphere vibrations animated by the velocity V generates a radial pressure $\nabla P_0 = -3\eta RV/h_0^2$. The charge density advection under the sphere vibrations, modifies the pressure profile P_0 . This modification is evaluated afterwards in this chapter by mean of the Onsager's coefficients.

J_v is a surface density current, for more details about (4.10) see appendix (7.7).

4.2.2 Charge current

The charge density current is generated simply from the advection of the charge density by the velocity field $v(z)$ combined with the salt electrophoresis. The charge current is given by the integration of the charge density current over the film width,

$$j_c = \rho(z)v(z) + n(z)\mu eE \quad (4.13)$$

$$J_c = \int_{-h/2}^{h/2} j_c dz. \quad (4.14)$$

Inserting the general expressions of the pressure and electroosmotic driven velocities, in the equation above and performing the simple integration one readily gets,

$$J_c = L_{cc} \frac{eE}{\eta} - L_{cv} \frac{\nabla P}{\eta}, \quad (4.15)$$

L_{cv} account for the pressure driven charge current, this coefficient describe the advection of the charge by the pressure driven velocity profile. This letter must be symmetric to L_{vc} according to Onsager's theory. L_{cv} can be calculated by integrating the electroosmotic velocity $v_E(z)$ (3.29) in (4.14),

$$L_{cv} = \int_{-h/2}^{h/2} \rho(z) \frac{h^2 - 4z^2}{8} dz, \quad (4.16)$$

L_{cc} account for the electric conductivity, that comprises the advection of the charge density by the electroosmotic velocity combined with the conduction of ions by means of the electric field, it is readily calculated by inserting (3.29) in (4.14),

$$L_{cc} = \int_{-h/2}^{h/2} dz \left(\rho(z)f(z) + \mu n_t(z) \right). \quad (4.17)$$

The relation (4.15) closed to the continuity equation, allows the calculation of the forces generated by the charge flow. The continuity equation reads,

$$\nabla \cdot J_c = -\partial_t C, \quad (4.18)$$

with $C = \int \rho(z)dz$ more details are given in the appendix (7.8)

4.3 Analytic expressions of Onsager's coefficients

In this section we provide in a first step the analytic expressions of the transport coefficients in the wide channel approximation. Where the film width is considered to be much larger than the diffuse layer thickness λ .

In a second step we provide the analytic expressions for the coefficients in the narrow channel where the film width is comparable to the Debye length λ . These coefficients are used afterwards to determine the coupling parameter between the volume and the charge currents.

The analytic expression of the coupling parameter as well as the force, are compared afterwards to numerical calculations in order to determine the relevance of the approximations used for the analytic calculations see appendix (7.10).

4.3.1 Wide channel approximation WCA

The wide channel approximation is used purposely in order to get analytic expressions for the coefficients, therefore the forces in the case where $h/\lambda \gg 1$. In this approximation the overlap between the potentials of the two surfaces is not taken into account.

Since the two surfaces are largely separated one can neglect the effect of one surface on the other, and consider just a single solid surface located at a position $z = 0$ in a contact with an electrolyte solution where the counterions occupy the half plane $z > 0$.

• Onsager Coefficients in WCA

From the charge density profile (2.2) it is obvious that the quantity of counterions close to the solid surfaces is very important and decrease exponentially to reach its minimum for distances far enough from the two surfaces.

The variations of the electrophoretic mobility $f(z)$ are linked to the charge density profile. For very small separations the counterions stay very close to the solid surfaces to ensure the surface charge screening, therefore the electrophoretic mobility is very small. As we moves away from the surface the counterions becomes free, thus the mobility increases before reaching a stationary state where the electrophoretic mobility equals to

$-\epsilon\phi_0/\eta$ [25].

Figure (4.1) expresses the variations of electrophoretic mobility $f(z) = v_E(z)/eE$ in linear scale as a function of the separation distance h .

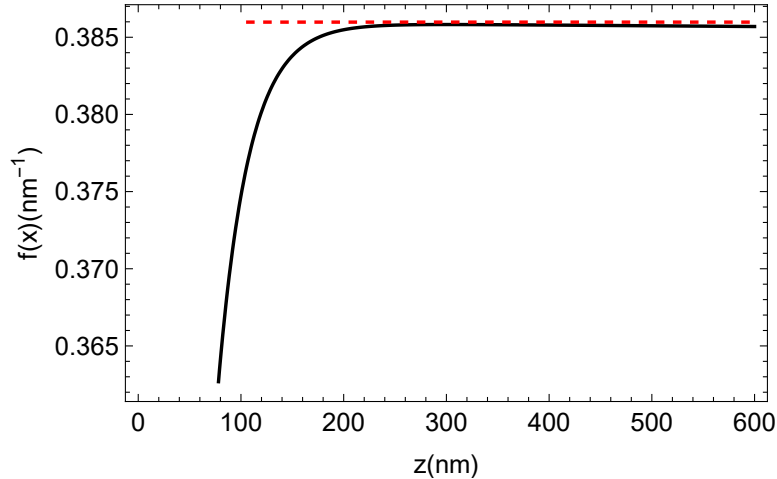


Figure 4.1: Electrophoretic mobility variations as a function of z on a linear scale. The profile is obtained in the WCA, using the boundary condition (CC) with $\sigma = 0.02\text{nm}^{-2}$ and a diffuse layer thickness $\lambda = 30\text{nm}$. The dashed line refers to Smoluchowski mobility. The variations are relevant in the range of separations where the WCA is valid $h \sim 5\lambda$.

Now that we know the velocity profile variations in the W.C.A, we can calculate Onsager coefficients starting with the off diagonal coefficients.

L_{vc} account for the electroosmotic effect given by Smoluchowski electrophoretic mobility times the film width h .

$$L_{vc} = -\frac{\phi_0 h}{4\pi l_B}, \quad (4.19)$$

these equation shows the linearity of the electroosmotic profile with respect to the electrolyte film width, i.e, the quantity of liquid dragged by the electric field depends only on the film width. Since the electrophoretic mobility $\mu = \phi_0/4\pi l_B$ remains constant.

L_{cv} account for the charge flow carried by the Poiseuille flow, symmetric to L_{vc} .

$$L_{cv} = -\frac{\phi_0 h}{4\pi l_B}, \quad (4.20)$$

this coefficient describes the contribution of the pressure gradient on the charge current, i.e, the advection of the charges by mean of the Poiseuille flow caused by ∇P .

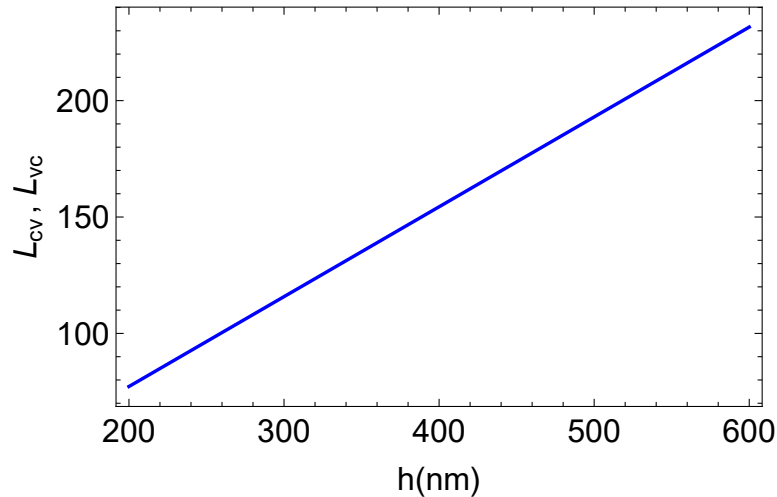


Figure 4.2: Plot of L_{vc} and L_{cv} as a function of h on a linear scale. The calculation is performed using (CC) boundary condition, with $\sigma = 0.02\text{nm}^{-2}$ and $\lambda = 30\text{nm}$. The variations are plotted in an range of values where the WCA approximation is valid.

The conductivity L_{cc} includes the charge density advection by the electroosmotic velocity $v_E(z)$, combined with the conduction of the salt ions by the electrophoresis effect [103].

$$L_{cc} = \frac{\sinh(\frac{\phi_0}{4})^2}{\lambda\pi^2 l_B^2} + \frac{n_0 h + \sigma}{3\pi a}, \quad (4.21)$$

the first term in (4.21) account for the surface conductivity which is proportional to surface charge density σ via $\sinh(\phi_0/2)$. This term is independent on the film width h , this means that the advection of charge by $v_E(z)$ for separations large enough compared to λ remains always constant.

The second term describes simply the conduction of the salt content by the radial electric field. It is characterized by two contributions, the first is linked to the diffuse layer counter ions electrophoresis, and the second is related to the bulk conduction $2\mu n_0 h$, this latter is dominant for large separations. a is the hydrodynamic radius of ions.

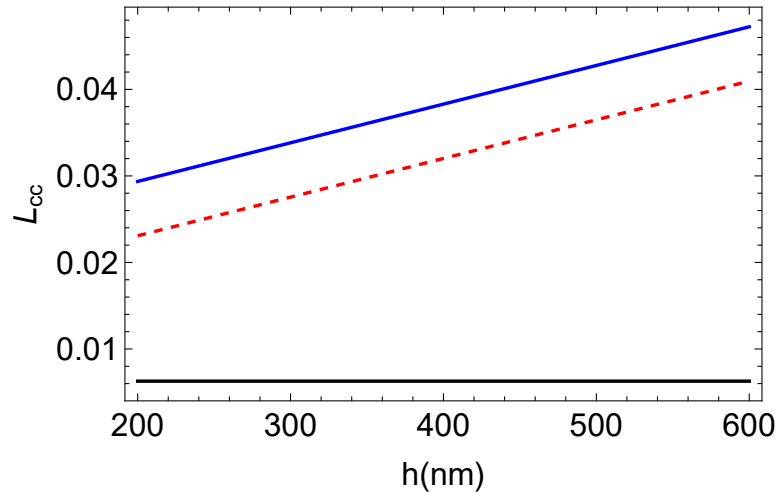


Figure 4.3: Plot of L_{cc} variations as a function of h on a linear scale. The calculations are performed using (CC) boundary condition with $\sigma = 0.02\text{nm}^{-2}$ and $\lambda = 30\text{nm}$. The black solid line refers to the surface conductance, the dashed red line designate the bulk conductance and the blue solid line expresses the combination of both contributions. The variations are plotted in an range of values where the WCA approximation is valid.

Figure (4.3) shows a plot in a linear scale, of the different components of the electric conductivity as a function of h . We notice that the surface conductance (black solid line) is very small compared to the bulk conductance (dashed red line). Thus the conduction for wide separations in WCA is dominated by the bulk conductance.

For more details on L_{cv} as well as L_{cc} calculated in the wide channel approximation (WCA), see appendix (7.9).

4.3.2 Narrow channel approximation NCA

As we mentioned in the introduction, it is paramount to study the electric double layers in a narrow channel, where the thickness of the water film confined between the surfaces is equal or smaller then the Debye length $h \leq \lambda$.

In this approximation, we consider that the two surfaces are located in positions $z = -h/2$ and $z = h/2$ respectively. When we work on such distances new proprieties emerges from the overlapping between the potentials of the surfaces, thus affect the viscous as well as the electric proprieties of the liquid medium.

In order to establish the analytic expression of the electrostatic potential in NCA, the overlapping effect must be taken into account when solving the non linear Poisson Boltzmann equation, see appendix (7.5).

To establish the analytical expressions of Onsager coefficients for a narrow channel, where the separation distance between the surfaces is comparable to the Debye length λ . We apply Taylor expansions with respect to the vertical coordinate on the electrostatic potential given by the equation (2.16) and expand the elliptic function cd to the second order in z ,

$$\phi(z, k) = \ln(k) - 4\pi l_B \sigma \frac{z^2}{h}, \quad (4.22)$$

where the parameter k is given by,

$$k = l_d + \sqrt{1 + l_d^2}. \quad (4.23)$$

The dimensionless quantity l_d characterizes the contribution of the surface and the bulk to the conductivity $l_d = \sigma/n_0h$. This quantity represent the Dukhin number [97], defined as the ratio between the surface charge density to the fluid bulk density multiplied by the separation distance h .

The effects of the overlapping between the potentials also influence the electric charge density ρ . Indeed when the confinement surfaces approach sufficiently each other, the counter ions cloud of the diffuse layer form a homogeneous gas density, which depends only on the separation distance h , thus we write,

$$\rho = \epsilon \partial_z^2 \psi = 2\sigma/h. \quad (4.24)$$

• Onsager Coefficients in N.C.A

Using (4.22) and relying on the general definition of the coefficients given by (4.11) and (4.16). One readily gets the off diagonal symmetric coefficients, which describes the electroosmotic and the pressure induced charge current respectively,

$$L_{vc} = L_{cv} = \frac{\sigma h^2}{6}. \quad (4.25)$$

Unlike the case of wide channel approximation, in which the non diagonal coefficient are given by Smoluchowski electrophoretic mobility times the separation distance h . In the case of narrow channel approximation they depends only on the surface charge density and the separation distance squared h^2 (figure 4.4). These changes in L_{vc} and L_{cv} coefficients are due to the overlapping effects.

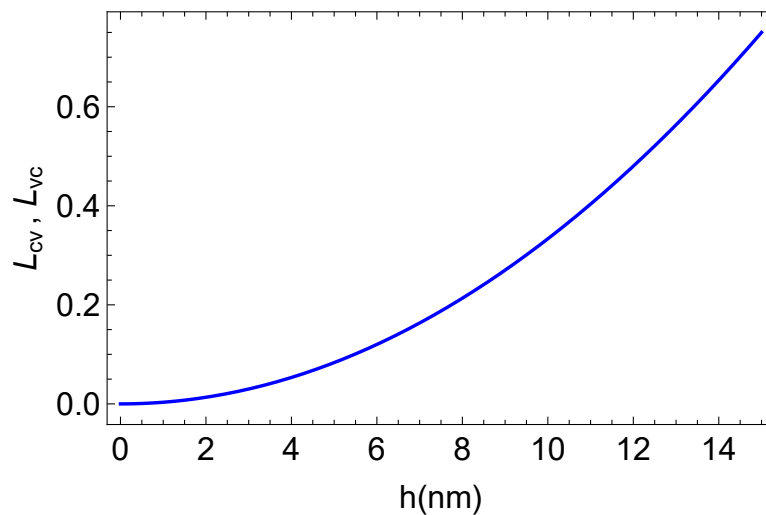


Figure 4.4: Plot of L_{vc} and L_{cv} as a function of h on a linear scale. The calculations are performed using (CC) boundary condition, with $\sigma = 0.02\text{nm}^{-2}$ and $\lambda = 30\text{nm}$. The variations are plotted in an range of values where the NCA approximation is valid.

$$L_{cc} = \frac{\sigma^2 h}{3} + \frac{n_0 h \sqrt{1 + (\sigma/n_0 h)^2}}{3\pi\alpha}. \quad (4.26)$$

The advection part of L_{cc} (first term) is remarkably different, compared to the case of wide channel approximation. This difference is manifested in the film height dependency,

where in NCA the advection of the charge density varies linearly with the separation distance h (figure 4.5), whereas in the WCA we noticed that the conduction is constant.

The second term of conductivity L_{cc} due to the salt electrophoresis depend on σ and varies linearly with h also,

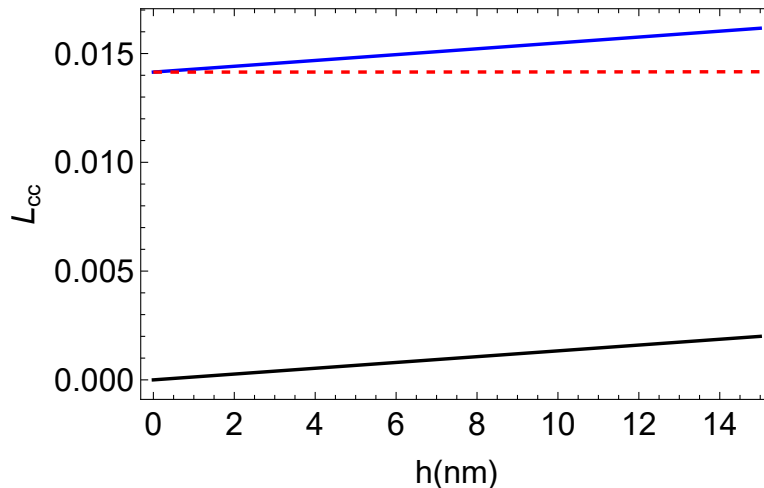


Figure 4.5: Plot of L_{cc} variations as a function of h on a linear scale. The calculations are performed using (CC) boundary condition, with $\sigma = 0.02\text{nm}^{-2}$ and $\lambda = 30\text{nm}$. The black solid line refers to the surface conductance, the dashed red line designate the bulk conductance and the blue solid line refers to the combination of both contributions. The variations are plotted in an range of values where the NCA approximation is valid.

The variations of the electric conductivity components in the NCA are very similare to that of the WCA with a dominance of the bulk conductivity.

4.4 Mobility effect

The conduction of the ions in a liquid medium by a certain conductive force, depends on the mobility of these ions. The ions mobility characterizes how quickly an ion can move through the liquid medium when pulled by a conducting force, this latter can be given by,

$$\mu = \frac{1}{6\pi\alpha\eta}, \quad (4.27)$$

where α is the hydrodynamic radius and η is the dynamic viscosity.

In the previous section, we considered that the mobility of coions and counterions are the same, i.e, a similar hydrodynamic radius has been imposed on the different ions. This approximation does not reveal the real behavior of the two species under the influence of a conductive force.

In reality the counter ions have a larger hydrodynamic radius than that of the co-ions. For example if we consider an electrolyte solution of NaCl, the hydrodynamic radius of Na^+ ions is equal approximately to 0.19nm while that of Cl^- is equal to 0.13nm.

The difference between the coions and counterions mobilities, affect the electric conductivity L_{cc} [103], on its second part related to the electrophoreses effect. Taking into

account the difference in mobilities, the new expression for L_{cc} can be given by,

$$L_{cc} = \int_{-h/2}^{h/2} dz \left(\rho(z)f(z) + \mu_+ n_+ + \mu_- n_- \right) \quad (4.28)$$

$$= \frac{\sinh(\frac{\phi_0}{4})^2}{\lambda \pi^2 l_B^2} + \sum_{\pm} \mu_{\pm} n_0 \left(h - \frac{4\gamma\lambda}{\gamma \mp 1} \right). \quad (4.29)$$

For similar mobilities we take the mean values of $(\alpha_{Na^+})^{-1}$ and $(\alpha_{Cl^-})^{-1}$ respectively, to determine the equivalent hydrodynamic radius,

$$\frac{1}{\alpha} = \frac{1}{2} \left(\frac{1}{\alpha_+} + \frac{1}{\alpha_-} \right). \quad (4.30)$$

Figure (4.6) shows a plot of the conductivity transport coefficient in the wide channel approximation, in the case of similar mobilities $\mu_{\pm} = \mu$ and dissimilar mobilities $\mu_+ \neq \mu_-$.

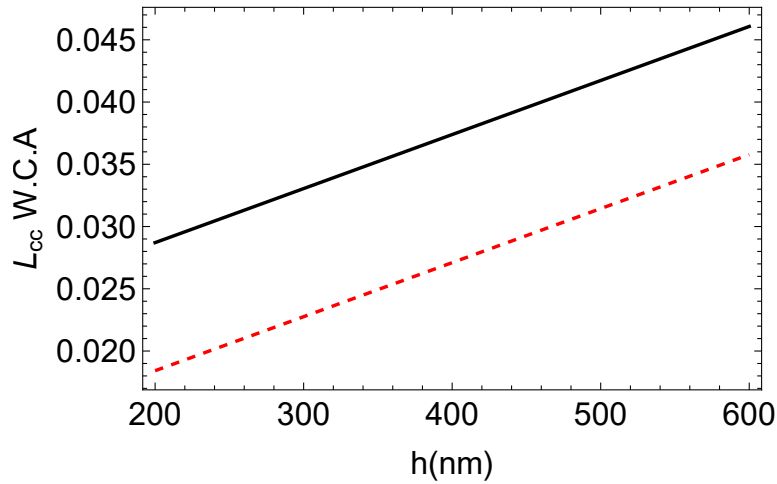


Figure 4.6: Plot of the conductivity coefficient L_{cc} as a function of h . The calculations are performed using (CC) boundary condition with $\sigma = 0.02\text{nm}^{-2}$ and $\lambda = 30\text{nm}$. $\alpha_{Na^+} = 0.19\text{nm}$, $\alpha_{Cl^-} = 0.13\text{nm}$ and the equivalent radius $\alpha = 0.15\text{nm}$. The black solid line shows L_{cc} variations in the case of similar mobilities while the dashed red line expresses the variations in the case of different mobilities.

The linear variations of the coefficient L_{cc} with respect to h , in WCA refers to the dominance of the bulk conductivity. The ions mobility in the case of similar mobilities (the counterions mobility) is smaller than the effective ions mobilities in the case of dissimilar mobilities. This difference translates the dominance of the black curve over the dashed curve in figure(4.6).

For the case of narrow channel the conductivity coefficient L_{cc} is given by,

$$L_{cc} = \frac{\sigma^2 h}{3} + \sum_{\pm} \mu_{\pm} \left(\pm \sigma + n_0 h \sqrt{1 + (\sigma/n_0 h)^2} \right). \quad (4.31)$$

As we did for the case of WCA, it is crucial to compare the electric conductivity in the case of similar and dissimilar mobilities, in order to highlight the effect of the mobility on L_{cc} for small separations. Figure (4.7) shows the plot of L_{cc} in the narrow channel approximation for both cases.

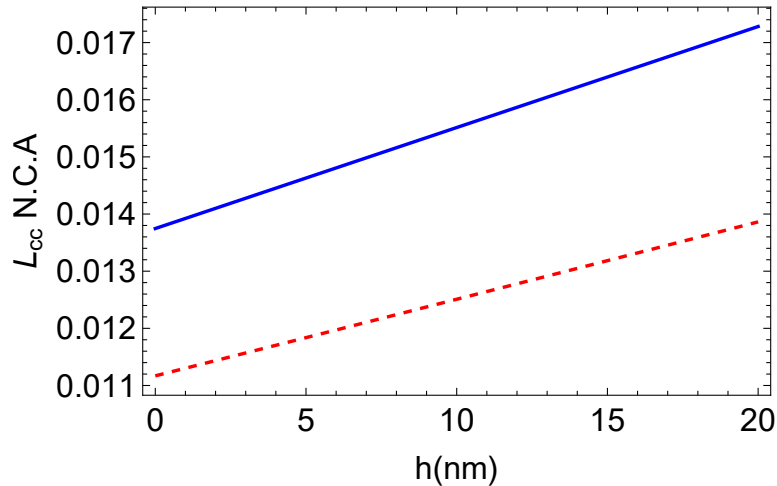


Figure 4.7: Plot of the conductivity coefficient on the narrow channel approximation as a function of h . The blue solid line shows L_{cc} variations for similar mobilities, while the dashed red color designate the variations under different mobilities.

For the case of narrow channel the linear behavior translates the dominance of the salt electrophoresis, the dominance of conductivity in the case of similar mobility (blue) due to an equivalent mobility smaller than the effective mobilities of ions (the same reason as in the case of the wide channel).

The difference in the conductivity L_{cc} due mobility effect in the case of NCA and WCA is very small, we consider from now on, that the mobility of the coions and counterions are similar in order to study the coupling parameter and the forces which depends on it.

4.5 The coupling parameter ξ

The coupling between the diffuse layer counterions and the liquid flow, may enhance the viscous damping acting on the vibrating sphere. In this section we aim to predict theoretically this enhancement and check the relevance of our model, to interpret the measured enhancement realized experimentally by coworkers.

For this purpose it is worth to mention that, the charge density profile remains always in the equilibrium state described by Poisson Boltzmann equation no matter the kind of the force acting on it. Given the importance of the electrostatic interaction in the vertical direction, the energy cost to be spent in order to move the charges in the radial direction is enormous, thus few counterions may be transported in the radial direction. Moreover the counterions transport leads to the establishment of a strong electric field which bring back the counterions to their equilibrium state, in a time $\tau \sim 10^{-6}s$ very small compared to the characteristic time of the sphere vibrations, thus the charge current vanishes very quickly and we write,

$$J_c = 0, \quad (4.32)$$

from this equation we can readily derive the expression of the electric field E , and insert it afterwards in the incompressibility condition (4.12) to evaluate the pressure gradient given by,

$$\nabla P = -\frac{6\eta r V}{h^3} \frac{1}{1 - \xi}, \quad (4.33)$$

where $6\eta rV/h^3$ is the pressure gradient in the absence of the charge density.

$$\xi = \frac{L_{cv}L_{vc}}{L_{vv}L_{cc}}, \quad (4.34)$$

ξ is the coupling parameter, which describes the coupling between the diffuse layer content and the flow, through the diagonal and off diagonal elements of the Onsager's matrix. In WCA the evaluation of this coefficient yields,

$$\xi = \frac{9\alpha\lambda\phi_0^2}{4h(\lambda\pi l_B^2(hn_0 + \sigma) + 3\alpha \sinh(\phi_0/4)^2)}, \quad (4.35)$$

where α is the equivalent hydrodynamic radius, equal to 0.15nm, σ the surface charge density and ϕ_0 is the potential value at the solid surface.

For sufficiently large distances, the coupling parameter varies with the separation distance as h^{-2} , whereas in the NCA the coupling parameter varies linearly with h ,

$$\xi = \frac{\pi\alpha\sigma^2}{(\pi\alpha\sigma^2 + n_0\sqrt{1 + (\sigma/n_0h)^2})}. \quad (4.36)$$

Figure (4.8) shows the variations of the charge-flow coupling parameter, as a function of the separation distance h in a logarithmic scale. For a surface surface charge density $\sigma = 0.02\text{nm}^2$ and a diffuse layer thickness $\lambda = 30\text{nm}$.

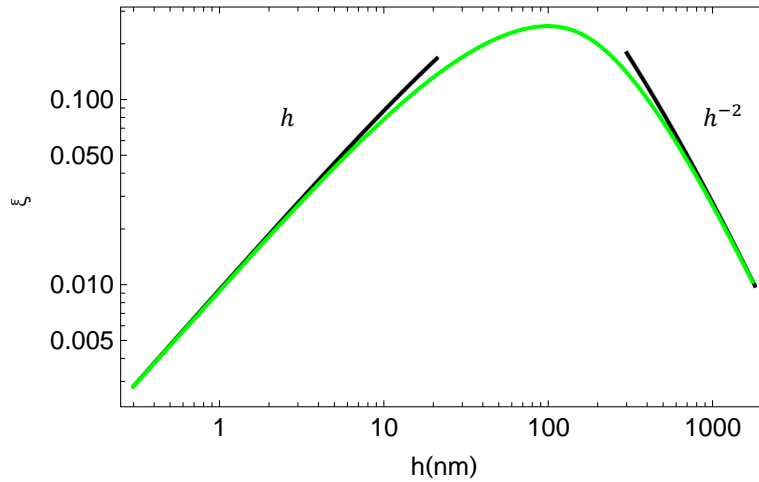


Figure 4.8: Charge-flow coupling parameter variations as function of the separation distance h on a logarithmic scale, the calculations are performed using (CC) boundary condition with $\sigma = 0.02\text{nm}^2$. The solid green line expresses the numerical calculations whereas the black lines expresses the analytique predictions for both narrow and wide channel approximations.

From figure (4.8), it is obvious that the numerical calculation (green solid line) and the analytical calculation (black solid lines) are well matched.

We can see that, the analytical curve is well aligned with the numerical one, for the case of NCA and WCA approximations. The coupling coefficient reaches its maximum value around $h \sim 3\lambda$, in this figure the maximum value is about 0.2, i.e. a correction of 20% compared to the non coupling case.

It is worth to mention the impossibility to describe analytically and in a complete way the phenomena linked to the electric double layer. We can clearly notice that the validity of the analytical approximations is limited just for the ranges where $h \gg \lambda$ for WCA and $h \ll \lambda$ for NCA. Thus we must rather consider numerical approaches for a better understanding of EDL, for more details on the numerical evaluations see appendix (7.10).

Regarding the impact of the boundary conditions on the coupling parameter ξ , it is important to evaluate this parameter within the (CC), (CP) and (CR) boundary conditions mentioned earlier, in order to compare and determine their influence on ξ .

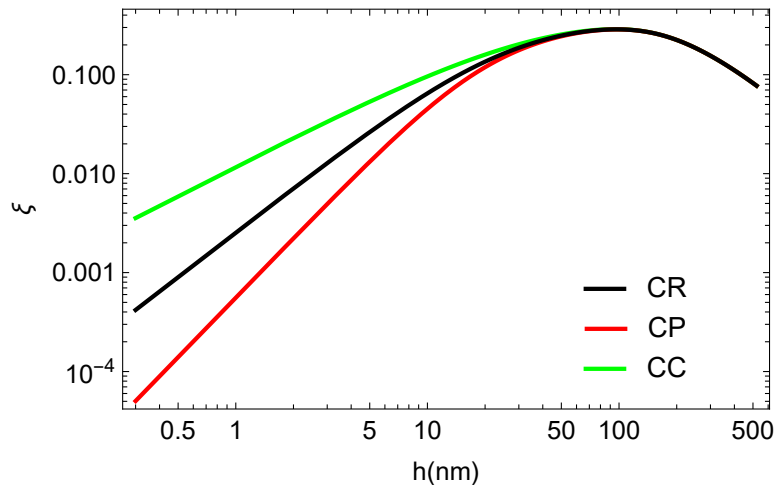


Figure 4.9: The coupling parameter ξ variations as function of h on a logarithmic scale, the calculations are performed using (CC), (CP) and (CR) boundary conditions, for (CC) the surface charge density $\sigma = 0.02\text{nm}^{-2}$, whereas for (CP) boundary condition the potential at the surface $\phi_0 = -3.39$, for (CR) the parameters as chosen in a way that for large separations the (CR) curve match the (CC) curve.

It is quite obvious that the various boundary conditions are relevant for very small separations, where we can see that the coupling coefficients take different values for each boundary condition, with more realistic values given by (CR) boundary condition.

All the curves converge towards the maximum value, meanings that the different boundary conditions have a very small effect on ξ , in the range of separations where $h \sim 3\lambda$ as shown in the figure (4.9). It is more convenient to use afterwards the constant charge boundary condition (CC) to evaluate the forces at the maximum value of ξ .

Since the charge-flow coupling may modify the physical characteristics of the system. Our following objective is to study the new properties that emerge from the coupling effect on the viscous damping force as well as the electrokinetic lifting force, applied on the lower surface of the sphere during its motion in the quasistatic case.

4.6 Electrostatic repulsive force

The static repulsive force is derived from the surface integration of the excess osmotic pressure [104–106] given by,

$$\Pi_O = k_B T (n_e - 2n_0) \quad (4.37)$$

$$= 2n_0 k_B T \left(\cosh \phi_m - 1 \right), \quad (4.38)$$

where $n_e = 2n_0 \cosh(\phi_m)$ and ϕ_m are the salt density excess and the electrostatic potential at midplane respectively. For more insights on the excess osmotic pressure see appendix (7.11)

Using the surface element of integration $dS = 2\pi R dh$ (Derjaguin approximation (3.7)), the static repulsive force can be given by [107],

$$K(h_0) = 2\pi R \int_{h_0}^{\infty} dh \Pi_O(h). \quad (4.39)$$

Note that for larger distances where $h \gg \lambda$ the potential vanishes, as a consequence the disjoining pressure as well as the repulsive force vanishes.

Experimentally the repulsive force is measured by simply making contact between the AFM sphere and the sample, we avoid any vertical or radial motion of the sphere, using small frequencies of the vibration.

This force is very useful to determine the surface charge density as well as the diffuse layer thickness, of the symmetric system used in the experiments. For this purpose we fit the static repulsive force which expresses the elastic behavior of the sample, with the theoretical predictions K .

Practically we change the values of the parameters λ and σ , until we get the right theoretical curve which fits well the experimental data figure (4.10), where the surface charge density of the lower sphere surface is estimated by 0.028nm^{-2} and the diffuse layer thickness by 47nm .

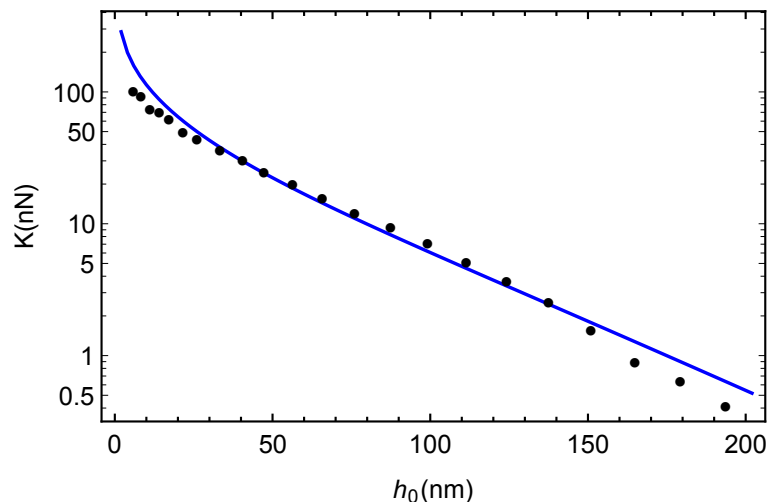


Figure 4.10: Plot of the static repulsive force K as a function of h_0 . The blue color designate the theoretical predictions while the black circles expresses the experimental findings. The experimental data are averaged so that each point corresponds to the average value of 100 measured values. The parameters used for the fitting are $\sigma = 0.028\text{nm}^{-2}$ and $\lambda = 47\text{nm}$ respectively.

The static repulsive force gives rise to a restoring force $-K_0Z$, which tends to counterbalance the static repulsive force, where K_0 is an effective spring coefficient [61].

Since the restoring force is a consequence of the static repulsive force, the spring coefficient can be established from the derivation of the repulsive force with respect to the radial coordinate r as,

$$K_0 = -\frac{dK}{dr} = 2\pi r\Pi_O. \quad (4.40)$$

The stiffness constant K_0 , which expresses the elastic effects of the electrolyte solution confinement is not going to be studied in this work, the focus is rather on the viscous effects only.

4.7 Electroviscous Force

The measurements of the electroviscous force, which rises from the electrolyte sample confinement, are made by an AFM sphere vibrating vertically near to its resonance frequency, with a sinusoidal motion $Z = A\sin(\omega_0 t)$. The constant amplitude of vibrations is very small compared to the film width h ($A \ll h$) [108],

The tip velocity can be expressed as,

$$V = \dot{Z}(t) = A\omega_0 \cos(\omega_0 t), \quad (4.41)$$

where ω_0 and A are the vibrations sphere frequency and amplitude respectively. The effect of the coupling parameter ξ , can be evaluated from the hydrodynamic pressure resulted from the integration of the modified pressure gradient over the channel height,

$$P(h) = 6\eta VR \int_h^\infty \frac{dh'}{h'^3} \frac{1}{1 - \xi(h')}, \quad (4.42)$$

we choose h as a variable of integration just for convenience. In the absence of the charge-flow coupling the Pressure reads as,

$$P_0(h_0) = \frac{-3\eta VR}{h_0^2}, \quad (\xi = 0), \quad (4.43)$$

this pressure vanishes quickly for large radial distances.

The electroviscous force is given simply by the surface integral of the pressure $P(h)$, with an elementary surface element of integration $dS = 2\pi R dh$,

$$F(h_0) = -2\pi R \int_{h_0}^\infty dh P(h), \quad (4.44)$$

this latter can be reexpressed as an electroviscous drag coefficient Γ , times the imposed velocity V and we write $F(h_0) = -\Gamma V$ [61] with,

$$\Gamma = -\pi\eta R \int_{h_0}^\infty dh \int_h^\infty \frac{dh'}{h'^3} \frac{1}{1 - \xi(h')}. \quad (4.45)$$

In the absence of the coupling the viscous force F_0 , is proportional to the hydrodynamic drag Γ_0 . Where $\Gamma_0 = 6\pi R^2\eta/h_0$ which is larger then the Stokes drag coefficient by a factor of R/h_0 ¹.

¹The drag force exerted on spherical objects with very small Reynolds numbers moving in a viscous fluid

To check the relevance of our theoretical model, which attempts to predict the viscous drag enhancement by mean of the charge density effect. We compare the electroviscous drag coefficient Γ measured experimentally from squeezing out the electrolyte solution sample, with the theoretical one resulting from equation (4.45).

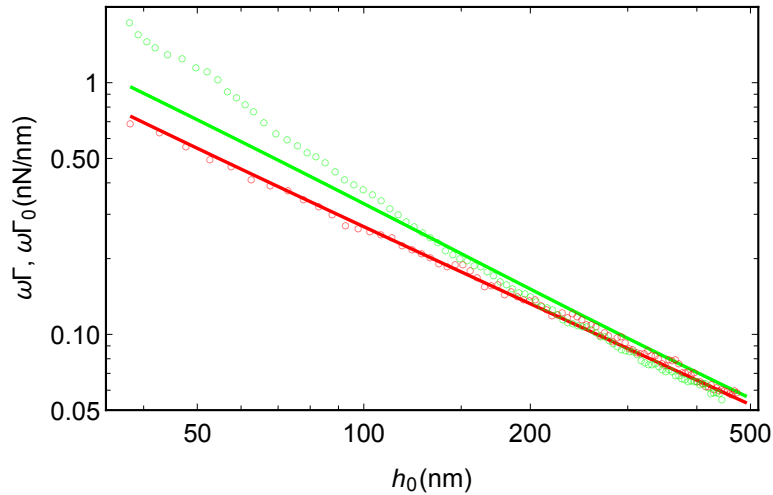


Figure 4.11: Plot of the drag coefficients variations as a function of h_0 on a logarithmic scale. With $\sigma = 0.028 \text{ nm}^{-2}$ and $\lambda = 47 \text{ nm}$. The red color refers to the viscous drag coefficient while the green color expresses the electroviscous drag coefficient. The open circles account for the experimental data while the solid lines on the theoretical predictions. The experimental data are averaged, so that each point corresponds to the average value of 100 measured values.

Figure (4.11) shows a comparison between the experimental (open circles) and theoretical (solid lines) drag coefficient, in the presence (green) and the absence (red) of the charge flow-coupling. For the case of viscous drag, we can notice good agreement between the experimental findings and the theoretical prediction.

For the electroviscous drag coefficient, we notice a disagreement between the experimental findings measured at $\omega_0 = 100 \text{ Hz}$ and the theoretical predictions. The measured coefficient is bigger than the theoretical one, especially for small separations. For larger separations the experimental curves tend towards the curve which describes the viscous drag coefficient, this translates the fact that the charge-flow coupling in the bulk tends towards zero, consequently the tip of the AFM measures the viscous force only.

The figure (4.11) provide a proof of the frequency dependence of the electroviscous response, especially for small separations. Since the relaxation time of the charge current is very small, the frequency dependence clearly indicates that the charge is not the relevant quantity to predict the experimental findings.

The missing quantity is the salt density of the electrolyte solution, in chapter 5 we deal with the effect of this quantity in details through the salt-charge-flow coupling parameter.

4.8 Electrokinetic lift force

Prieve and coworkers following their study on latex microspheres motion in a liquid solution, they noticed the generation of a repulsive force when a charged particle moves

parallel along a charged macroscopic surface. This force commonly known as electrokinetic lift force appears to act in the normal direction to the microspheres surface [73,74].

In this section we attempt to study this force, through a sliding motion of a sphere parallel to the substrate. In order to provide an analytic expression for this force in the wide and narrow channel approximations, to compare it afterwards with the lift force measured experimentally.

Let's consider a confined electrolyte solution between a substrate and a sphere, moving along the radial direction parallel to the substrate, both the lower sphere surface and the substrate carries the same charge density σ (symmetric geometry), figure 1.8.

The sliding motion induces a linear shear flow in the radial direction given by,

$$v_s = \frac{z}{h}V, \quad (4.46)$$

where V is the sphere vibrations velocity, considered negligible given the small frequencies $\omega_0 \sim 10Hz$ used in the experiment,

$$V = V_0 \cos(\omega_0 t) \quad (4.47)$$

$$V \simeq V_0. \quad (4.48)$$

The linear shear flow is associated with a pressure field, generated by the sphere motion, this latter is given by,

$$P_0 = \frac{\eta V}{R} \left(\frac{R}{h_0} \right)^{\frac{3}{2}} \left(\frac{6}{5} \hat{\rho} + \mathcal{O}\left(\frac{h_0}{R}\right) \right) \cos(\theta), \quad (4.49)$$

this equation represent the solution of the non linear Reynolds equation [109], where R is the radius of the sphere, η the dynamic viscosity, h_0 the minimum distance sphere-surface, θ the polar angle, \hat{r} is a reduced radial coordinate $\hat{r} = r/\sqrt{Rh_0}$ and \hat{h} the reduced separation distance [90] given by,

$$\hat{h} = \frac{h}{h_0} = 1 + \frac{\hat{\rho}^2}{2}, \quad (4.50)$$

this expression for \hat{h} is valid only in the lubrication zone where $h_0 \ll R$, regarding the speed of the sphere in the radial direction.

It is already known that the relaxation time of the charge current, is very small compared to the characteristic time of the sphere vibrations (see appendix (7.12) for more details on the charge current relaxation time), therefore we can say that the charge current is negligible $J_c = 0$ and we write,

$$eE = \frac{L_{cv}}{L_{cc}} \nabla P_0, \quad (4.51)$$

since the charge advection by the shear flow vanishes, in a symmetric geometry where the charge density on the lower sphere surface and the substrate is the same,

$$L_V = \frac{1}{h} \int_{-h/2}^{h/2} dz z \rho_1(z) - \sigma_2, \quad (4.52)$$

where σ_2 is the surface charge density of the sphere moving at the velocity V , and $\rho_1(z)$ is the charge density profile of the immobile substrate, with $\int \rho_1(z) dz = \int \rho_2(z) dz = \sigma_2$.

According to Bike and Prieve, the electrostatic contribution to the disjoining pressure is dominant. According to this assumption, we aim to determine the electric lift force generated from the radial electric field, then study the coupling between the charge density and the flow, to see whether the coupling has a significant effect on the lift force or not.

The lift force results from the normal component of the stress tensor acting on the sphere surface, which can be defined as,

$$\sigma_{nn} = P_0 + \frac{\epsilon}{2} E_{\parallel}^2, \quad (4.53)$$

where E_{\parallel} is the radial part of the electric field, and ϵ is the permittivity of the medium considered homogeneous and constant. The lift force is given by the surface integral of the stress tensor as,

$$F = \int dS \sigma_{nn} = -\frac{\epsilon}{2} \int r dr d\theta E_{\parallel}^2. \quad (4.54)$$

Owing to the dependence of P_0 on the angle θ ² the integral of the antisymmetric pressure over dS vanishes.

Inserting the coupling parameter calculated from Onsager coefficients, in the pressure gradient ∇P and performing the surface integral one gets,

$$F = -\frac{(24\sqrt{6}\eta V \phi_0 \alpha)^2 R \pi^3 \lambda^4}{125 h_0^3 k_B T l_B} \Gamma\left(\frac{\sigma}{n_0 h_0}\right). \quad (4.55)$$

The first term in (4.55) recovers the result of Bike and Prieve, that was found for a sufficiently large separations [73, 74]. The second term describes the surface charge correction to the lift force, for large distances where $h_0 \gg \sigma/n_0$, we get $\Gamma(0) = 1$, a full expression of the correcting function Γ is given by,

$$\Gamma(x) = \frac{(5x+4)}{x^2(2x+1)} [2x(3+6x+x^2) + 3(1+3x+2x^2) \ln(1/(x+1))], \quad (4.56)$$

where $x = \sigma/n_0 h_0$.

For small distances where $h_0 \ll \sigma/n_0$, using Taylor expansions one finds,

$$\Gamma(x) \sim \frac{16}{5x^2}, \quad (4.57)$$

thus the lift force at small separations varies as $1/h_0$,

$$F = -\frac{(3\eta V \phi_0 \alpha)^2 R \pi}{40 h_0 k_B T l_B^3 \sigma^2}. \quad (4.58)$$

Figure (4.12) shows the variations of the lift force predicted by our theoretical model, as a function of the separation between the lower sphere-substrate surfaces. The solid line refers to the total force given by equation (4.55).

The black dashed line translates the variations for sufficiently large separations where the force varies as $1/h_0^3$, the blue dashed line indicates the variations for very small separations where the force varies as $1/h_0$.

²The profile of the pressure is antisymmetric $P_0(r, \theta) = -P_0(r, \pi - \theta)$

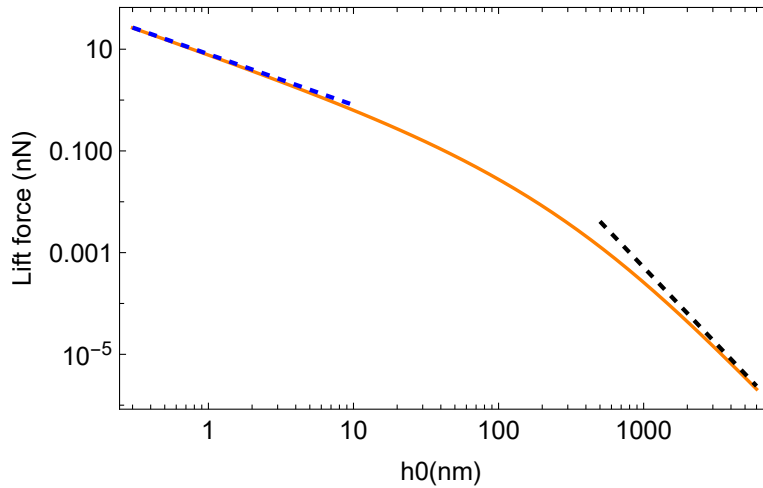


Figure 4.12: Plot of the theoretical lift force as a function of the channel height h_0 . Where the surface charge density $\sigma = 0.02\text{nm}^{-2}$ and the screening length $\lambda = 30\text{nm}$. The solid line refers the total force (4.55), whereas the black dashed line refers to Bike findings and the blue dashed line to the force at small separations.

The black dashed line in the figure expresses the analytic results found by Bike et al [74], for a force measured between two sufficiently distant spheres, this latter coincides perfectly with our analytic model.

As it has been mentioned before, the main interest for the forces study lies in the small separations range. For the case on the lift force, the theoretical predictions (4.55) have shown variations following the law h^{-1} , to check the relevance of these predictions, we compare them simply with the numerical calculations.

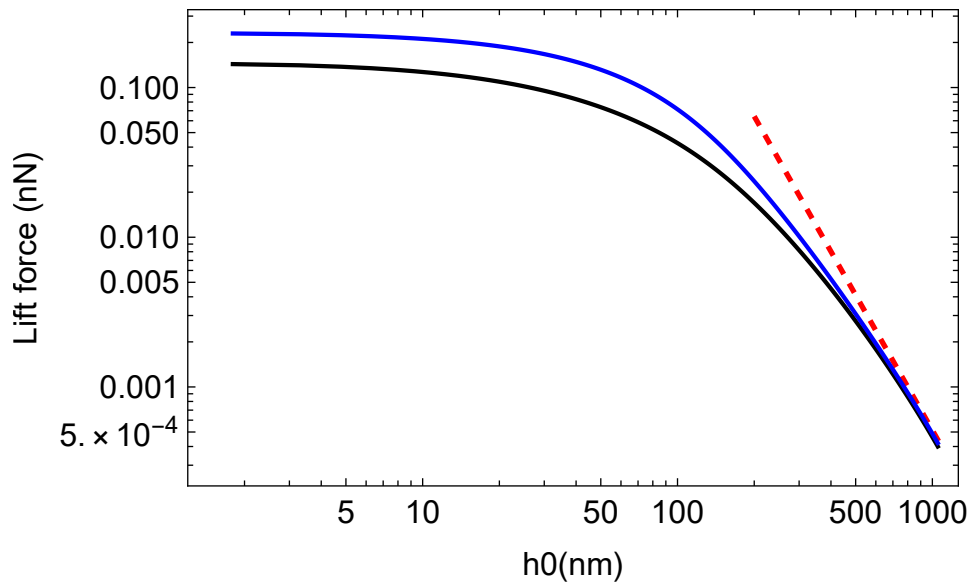


Figure 4.13: Plot of the lift force variations as a function of the channel height h_0 on a logarithmic scale. The black curve indicates the numerical evaluations without coupling effect, the blue one refers to the numerical lift force with the coupling effect, the dashed red line indicates the curve found by Bike and Prieve.

Figure (4.13) shows a comparison, between the curves of the lift force calculated analytically

ically and numerically, with arbitrarily chosen parameters $\sigma = 0.02\text{nm}^{-2}$ and $\lambda = 30\text{nm}$. For sufficiently wide separations we notice a good agreement between the analytical curve (red) and the numerical one, the variations of both curves follow the law $1/h_0^3$ predicted by Bike and Prieve [74].

For small separations we notice that the numerical curve shows a plateau, whereas the theoretical model revealed a variations as $1/h_0$. This means that the approximation used to calculate the analytical lift force for small distances is irrelevant and the law $1/h_0$ does not describe the physical reality.

The discrepancy obtained for small distances, is due to the effect of overlapping potentials, i.e. The analytical function of the lift force (4.58), for small separations is calculated from a potential, which does not take into account the effects of overlapping. While in the numerical calculation the overlapping is taken into account through Jacobi's functions (2.16).

The blue curve shows the coupling effect on the lift force, we notice an enhancement of the lift force for small separations where the charge-flow coupling is significant, this enhancement disappears in the bulk region for large separations.

Given that the numerical calculations are more relevant for small separations. In the following we rely on the numerical findings to fit the experimental curve of the lift force.

To fit the experimental data, it is necessary to find the right values of Debye length λ and the surface charge density σ . For that we proceed in the same way used to determine these two parameters in the case of the electroviscous force, i.e. We fit the static repulsive force measured experimentally by the theoretical model which describes the repulsive force K (4.39).

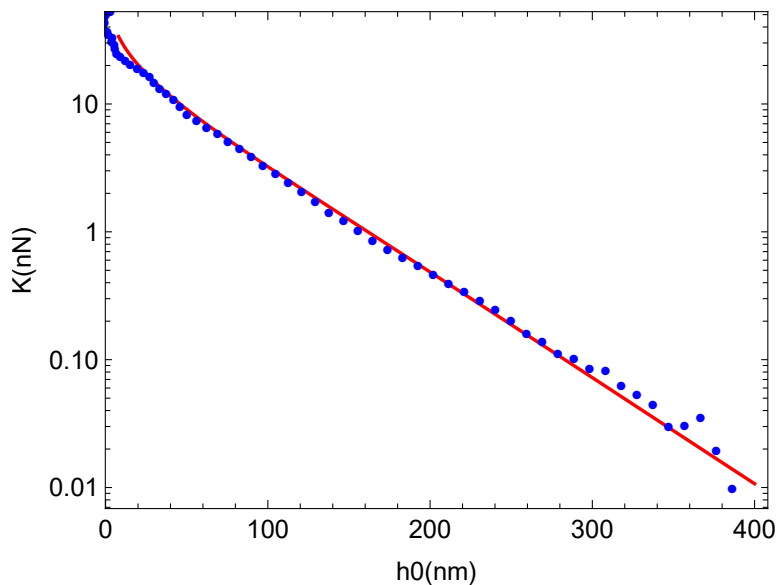


Figure 4.14: Plot of the static repulsive force K variations as a function of h_0 on a logarithmic scale. The blue circles refers to the averaged experimental data while the red one is account for the theoretical predictions. The parameters used for the fitting are $\sigma = 0.0055\text{nm}^{-2}$ and $\lambda = 52\text{nm}$. The experimental data are averaged so that each point corresponds to the average value of 100 measured values.

Figure (4.15) shows a comparison, between the experimental findings for the lift force

(black circles) and the numerical evaluations given by the solid (solid lines). The blue curve shows the effects of the charge-flow coupling on the lift force, the coupling effect is small and has a little effect on the force.

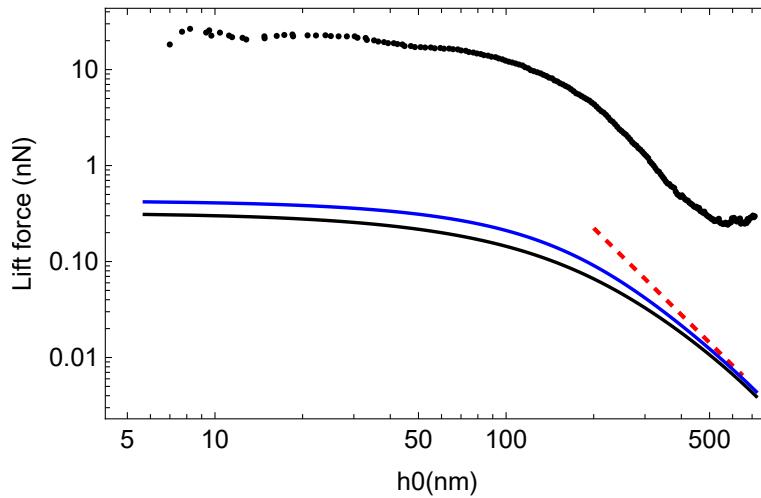


Figure 4.15: Comparison between the numerical evaluation and the measured lift force with respect to the separation distance h_0 on a logarithmic scale. With $\sigma = 0.0055\text{nm}^{-2}$ and $\lambda = 52\text{nm}$. The black circles indicates the averaged experimental findings where each point corresponds to the average value of 100 measured values, while the blue and the black curves designates the theoretical predictions with and without coupling respectively.

Despite the fact that the experimental curve follows the law of $1/h_0^3$ for very large separations, the difference between the latter and the numerical curve remains significant, this difference is noticed in previous works by Bike and Prieve [73,74] and it may be linked to the overestimation of the electrical conductivity of the medium expressed in our case by the coefficient L_{cc} .

This discrepancy between the theoretical predictions and the experimental findings confirms the previous results found by Bike and Prieve [73,74], Cox [66] and Schnitzer et al [75], and it shows that the charge-flow coupling is insufficient to describe the measured lift force.

From figure (4.15), one can conclude that the charge density only, is insufficient to interpret the experimental findings for the lift force, thus it is necessary to take into account the salt contained in the electrolyte solution to properly describe this force.

4.9 Conclusion

In this chapter, we first studied the effect of the charge-flow coupling on the electroviscous force, in the case of a sphere squeezing a sample of an electrolyte solution against a substrate, then we investigated the electrokinetic lift force due to the motion of a sphere parallel to a substrate.

The investigation of both phenomena, were based on an assumption which stipulates that the charge density profile always remains in the equilibrium state, thus the Onsager coefficients related to the charge density were calculated in the equilibrium state.

The first conclusion that can be drawn from this study, is the impossibility to study the forces generated from the perturbations of the electric double layer, by an analytical model that remains valid for all the separations between the sphere and the substrate.

As we have seen in the case of the electroviscous force, we notice a qualitative agreement between the theoretical predictions and the experimental findings. Quantitatively we have a difference for very small separations. This difference can be linked to our approach based only, on the charge density effects without including the compensated salt density effect.

For the case of the lift force also, we have a qualitative agreement regarding the variations of the force for large distances, but quantitatively we have a very important disagreement.

Our theoretical prediction, show clearly that the coupling between the charge and the flow only, is not sufficient to interpret the experimental findings on both forces. This discrepancy found between the experimental measurements and the theoretical findings, confirm the conclusions of Bike and Prieve [73, 74] and Schnitzer et al [75].

Before concluding on the relevance of our approach, which consists on evaluating the coupling parameter ξ from Onsager coefficients calculated at the equilibrium state. We take into consideration in the following chapter the salt density contained in the electrolyte solution, which is the missing quantity that the dynamic response interpretation has revealed, figure (4.11).

Regarding the calculation of Onsager coefficients and the different forces in the case of the salt-charge-flow coupling. We adopt the same approach which consists in calculating the coefficients in the equilibrium state. More details about these calculations are given in the following chapter.

Chapter 5

Salt-charge-flow coupling

This chapter describes a preliminary study about the salt-charge-flow coupling effect on the electroviscous force. Assuming at first that the deviations of the salt and charge densities are very small compared to the equilibrium state, this assumption allows the calculation of the transport coefficients at the equilibrium state.

Given the charge current relaxation time $\tau_c \sim 10^{-6}$ s, that is much smaller than the typical sphere vibrations time $\omega_0^{-1} \sim 10^{-2}$ s (Further details are in (7.12)).

Since the charge density is irrelevant to interpret the experimental findings for the electroviscous force as well as the lift force. The salt density contained in the electrolyte solution, could be the missing element that allows a better description of the electric double layer in the dynamic case. We define the salt density as the sum of the co-ions and counterions densities (97),

$$n_t = n_+ + n_- \quad (5.1)$$

$$= 2n_0 \cosh \phi. \quad (5.2)$$

Figure (5.1) shows the salt density profile variations in a symmetric geometry, where the variations of the electrostatic potential ϕ are given in the framework of (CC) boundary condition.

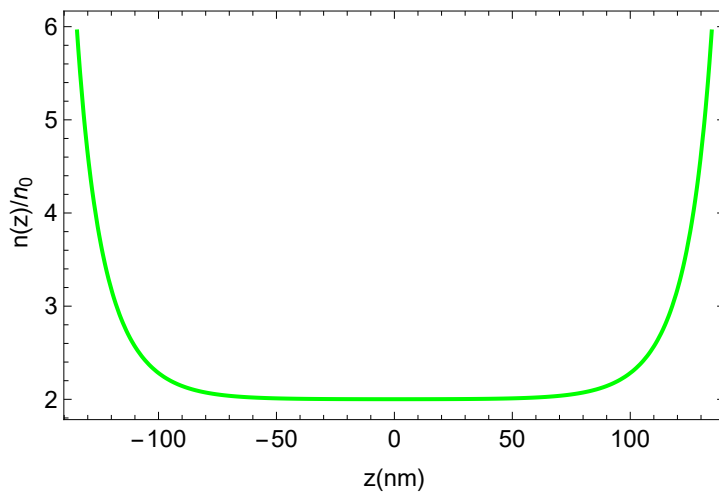


Figure 5.1: Salt density variations as a function of z on a linear scale. The profile is calculated in (CC) boundary condition where $\sigma = 0.02\text{nm}^{-2}$ and $\lambda = 30\text{nm}$. For sufficiently large distances the salt density equals to $2n_0$.

For two surfaces far enough apart, the salt profile consist of the counterions density close to the surfaces, plus the bulk density $2n_0$. This quantity is inert $n(0) = 2n_0$ therefore it must be substituted from the salt density, in order to determine the salt density at the equilibrium state, used afterwards to calculate Onsager coefficients. In the superposition approximation, the integration of the salt over the separation distance h yields $2\sigma + 2n_0h$.

We assume that the sphere motions force a small quantity of salt \hat{n}_0 (from the salt profile at the equilibrium state) to move in the radial direction, at the same time this latter diffuses and restore the equilibrium state. We consider that the salt density remains close to its equilibrium state at each moment and we write $J_s = 0$.

The quantity \hat{n}_0 is characterized by a non uniform variation in the radial direction, which makes its analytical derivation very tricky, how can we calculate this quantity? A relevant question that makes one think on a model that allows to evaluate it.

5.1 Salt-charge and volume currents

The currents J_v , J_c and J_s can be written in a matrix form as following,

$$\begin{pmatrix} J_v \\ J_c \\ J_s \end{pmatrix} = \begin{pmatrix} L_{vv} & L_{vc} & L_{vs} \\ L_{cv} & L_{cc} & L_{cs} \\ L_{sv} & L_{sc} & L_{ss} \end{pmatrix} \begin{pmatrix} -\nabla P \\ eE \\ X \end{pmatrix} \quad (5.3)$$

Same as the case of the charge-flow coupling, the diagonal coefficients of the matrix (\mathbf{L}), link each force with its conjugate current, whereas the off diagonal coefficients links the forces to the non conjugate currents.

The sphere's motion advects the salt, producing in turn various processes such as diffusioosmosis and diffusiophoresis, these processes are further detailed by Onsager coefficients in this chapter.

5.1.1 The volume current

The volume current can be given by the velocity field integrated over the channel height,

$$J_V = \int_{-h/2}^{h/2} v(z) dz, \quad (5.4)$$

where,

$$v(z) = v_p(z) + v_E(z) + v_s(z), \quad (5.5)$$

where $v_p(z)$ is the pressure driven velocity, $v_E(z)$ is the electroosmotic velocity generated from the body force eE acting on the ions.

$v_s(z)$ is the diffusioosmotic velocity induced from, the non equilibrium thermodynamic force X (2.32) acting on the ions. this latter force is an entropic force not a body force, it means that this force can be null on a given region on the system (3.31).

Given the negligible effect of the mobility on Onsager's coefficients (chapter 3, Mobility effect). We consider the case of similar mobilities and diffusion coefficients, i.e, the conduction and the diffusion of the coions and counterions, is done in the same way regardless their charge.

$$\mu_+ n_+ + \mu_- n_- = \mu(n_+ + n_-) = \mu n_t \quad (5.6)$$

$$D_+ n_+ + D_- n_- = D(n_+ + n_-) = D n_t \quad (5.7)$$

By taking into account the analytical expressions of the various velocity components (3.25,3.28, 3.32) and performing the integral (5.4) above one finds,

$$J_v = L_{vc} \frac{eE}{\eta} - L_{vv} \frac{\nabla P}{\eta} + L_{vs} \frac{X}{\eta}. \quad (5.8)$$

It is worth mentioning that the coefficients used in the charge-flow coupling remains the same in the case of salt-charge-flow coupling, by these coefficients we specify L_{vv} , L_{cc} , L_{vc} and its symmetrical coefficient L_{cv} .

L_{vs} account for the diffusioosmotic effect, this coefficient describe the advection of the liquid by mean of the diffusioosmotic velocity profile,

$$L_{vs} = \int_{-h/2}^{h/2} H(z) dz, \quad (5.9)$$

where the diffusiphoretic mobility is given by (3.32).

The relation (5.8) is closed by the incompressibility condition between the volume current and the imposed velocity $V(t)$.

$$\frac{rV(t)}{2} - J_v = 0. \quad (5.10)$$

In the absence of the charge and salt densities, the sphere vibrations with a velocity V give rise to a radial pressure gradient $\nabla P_0 = -3\eta RV/h_0^2$ generated from the liquid flow.

In the presence of the charge and salt densities this profile P_0 is subject to a modification that can be evaluated afterwards by mean of the coupling parameter ξ .

J_v is a surface density current, for more details about (5.10) see appendix (7.7).

5.1.2 Charge current

The charge current includes the charge density advection by the velocity field $v(z)$ integrated over the channel height, associated with the ions conduction integrated as well over the channel height,

$$J_c = \int_{-h/2}^{h/2} c(z)v(z)dz + \int_{-h/2}^{h/2} \mu \left(n_t(z)eE + \rho(z)X \right) dz. \quad (5.11)$$

Using the general formula of the velocity profile components (3.25,3.28, 3.32), and performing the integral one finds the expression of the charge current.

This equation is similar to (4.15), except for the third term described by the coefficients L_{cs} , which results from the advection of the charge density by the diffusioosmotic velocity.

$$J_c = L_{cc} \frac{eE}{\eta} - L_{cv} \frac{\nabla P}{\eta} + L_{cs} \frac{X}{\eta}, \quad (5.12)$$

L_{cs} expresses a contribution to the charge current induced by the diffusioosmotic velocity profile, combined to the conduction of the charge density by the thermodynamic force X .

$$L_{cs} = 2 \int_0^{h/2} dz \rho(z)H(z) + 2\mu \int_0^{h/2} dz \rho(z). \quad (5.13)$$

The relation (5.12) is closed by the continuity equation, allowing to calculate the forces generated by the charge current, the continuity equation read as,

$$\nabla \cdot J_c = -\partial_t c. \quad (5.14)$$

5.1.3 Salt current

The salt current consists of two contributions, a contribution from the salt current density j_s integrated over the channel height, combined with the conduction of the ions within the sample.

$$j_s = n(z)v_s(z) + \mu \left(\rho(z)eE + n_t(z)X \right). \quad (5.15)$$

$$J_s = \int_{-h/2}^{h/2} j_s dz, \quad (5.16)$$

with $n(z)$ the effective salt density, derived from the subtraction of the inert salt density at midplane $n(0)$ from the total salt density $n_t(z)$, $n(z) = n_t(z) - n(0)$.

Using the definition of the velocity components (3.25, 3.28, 3.32), and performing the integral given by (4.16), one can find,

$$J_s = L_{sc} \frac{eE}{\eta} - L_{sv} \frac{\nabla P}{\eta} + L_{ss} \frac{X}{\eta}. \quad (5.17)$$

L_{sv} account for salt flow or salt advection carried by Poiseuille flow.

$$L_{sv} = \int_0^{h/2} dz n(z) \frac{(h^2 - 4z^2)}{8}. \quad (5.18)$$

L_{ss} includes the salt flow generated by diffusioosmotic velocity $v_s(z)$, combined with ions conduction by X ,

$$L_{ss} = 2 \int_0^{h/2} dz \left(n(z)H(z) + \mu n_t(z) \right). \quad (5.19)$$

L_{sc} describes the salt flow induced by the electroosmotic velocity, combined to the conduction of the charge density by the body force eE ,

$$L_{sc} = 2 \int_0^{h/2} n(z)f(z)dz + 2\mu \int_0^{h/2} dz \rho(z). \quad (5.20)$$

The relation(5.17), is closed by the salt continuity equation (96,98) given by.

$$\nabla \cdot J_s = -\partial_t N, \quad (5.21)$$

where the radial salt density N , is given simply by the integration of the salt density over the film width $N = \int n(z)dz$. More details are given in (7.8)

5.2 Analytic expressions of Onsager's coefficients

In this section we give the analytical expressions of the coefficients, in the case of wide channel approximation where the channel height is greater than Debye length, and narrow channel approximation where the separation is comparable or even smaller than Debye length.

Afterwards we calculate the salt-charge-flow coupling parameter analytically, in order to compare it with the numerical evaluations, to see the relevance of our theoretical model.

5.2.1 Wide channel approximation WCA

As mentioned before the wide channel approximation, is an approximation used in order to get analytic expressions of the coefficients in case where $h \gg \lambda$. In this approximation the overlap between the potentials of the surfaces is not taken into account, because of the large distance which separates the two solid surfaces.

Given the larger separation between the surfaces, we neglect the effect of one of the surfaces, considering just a single solid surface located at $z = 0$, in a contact with an electrolyte solution where the counterions occupy the half plane $z > 0$ (infinite half space geometry). The analytic expression of the electrostatic potential remains the same as in (2.10).

It is worth to mention that the coefficient, which involve the salt density are calculated from the effective salt density at the equilibrium state, after subtracting the bulk salinity $2n_0$ from the total salt density $n_t(z)$.

Onsager Coefficients in WCA

From the salt profile given in figure (5.1), we have for small separations, the quantity of counterions close to the solid surfaces is very important and decrease exponentially, to reach its minimum for distances far enough from the surfaces.

The variations of the diffusiophoretic mobility profile [98], are linked to the salt density profile. In fact for very small separations the counterions remains close to the solid surfaces to ensure σ screening, therefore a very small quantity will be diffused. As one moves away from the solid surface the counterions get freer and freer, consequently the diffusion increases before reaching a stationary state where the ions diffusion attained its maximum.

This variations are well presented in figure (5.2), which illustrates the variations of the diffusiophoretic mobility $H(z)$ in linear scale as a function of the separation z .

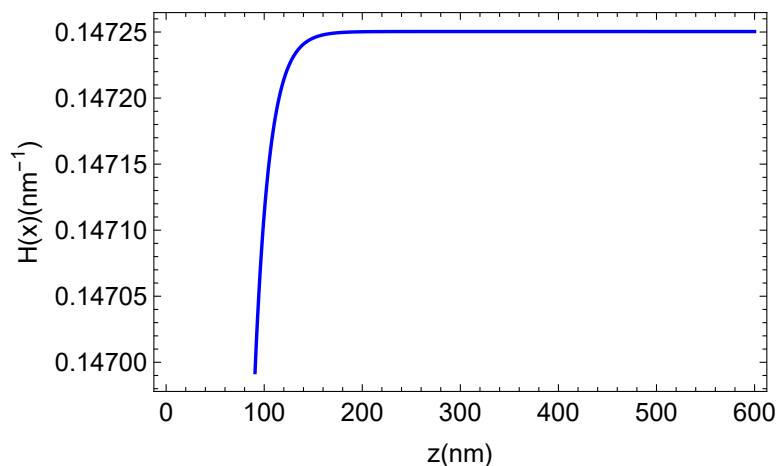


Figure 5.2: Diffusiophoretic mobility variations as a function of z on a linear scale. The profile is calculated in WCA, using the boundary condition (CC) with $\sigma = 0.02\text{nm}^{-2}$ and $\lambda = 30\text{nm}$. The variations are relevant in the range of separations where the WCA is valid $h \sim 5\lambda$.

The coefficient L_{vs} describe the diffusioosmotic effect [110], given simply by the diffu-

siophoretic mobility times the channel width h ,

$$L_{vs} = \frac{h}{\pi l_B} \ln(\cosh(\frac{\hat{\xi}}{4})), \quad (5.22)$$

these equation shows the linear variations of the diffusioosmotic, with respect to the channel height, i.e, the quantity of liquid dragged under the effect of salt diffusion depends only on the separation distance. Since the electrophoretic mobility $\frac{1}{\pi l_B} \ln(\cosh(\frac{\hat{\xi}}{4}))$ remains constant.

L_{sv} is the symmetric coefficient for L_{vs} , its account for salt flow carried by Poiseuille flow.

$$L_{sv} = \frac{h}{\pi l_B} \ln(\cosh(\frac{\hat{\xi}}{4})), \quad (5.23)$$

this coefficient describes, the contribution of the pressure gradient on the salt current generation, i.e, the advection of the salt density by mean of the Poiseuille flow caused by ∇P .

The figure 5.3 shows the variations of the coefficients L_{sv} and L_{vs} , as a function of h .

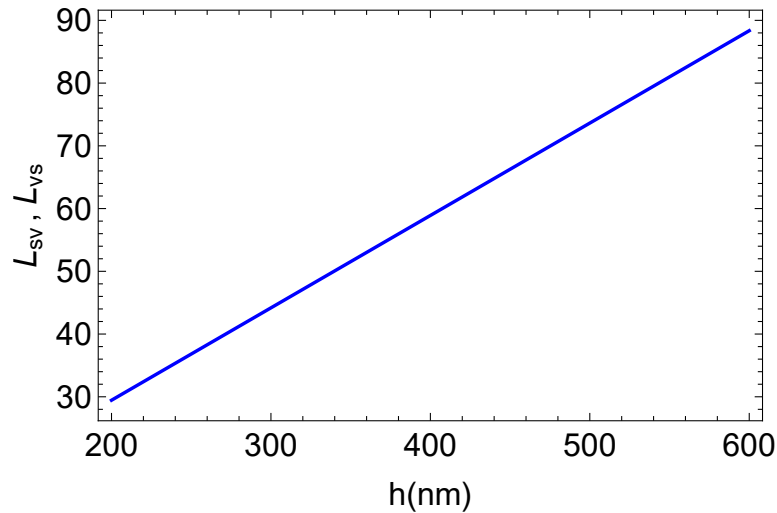


Figure 5.3: Plot of L_{vs} and L_{sv} as a function of h on a linear scale. the calculations are performed using (CC) boundary condition, with $\sigma = 0.02\text{nm}^{-2}$ and $\lambda = 30\text{nm}$. The variations are plotted in an range of values where WCA approximation is valid.

The coefficient L_{ss} combine the salt flow generated by diffusioosmotic velocity $v_s(z)$ [111], combined to ions conduction by mean of the thermodynamic force X ,

$$L_{ss} = 64n_0^2\lambda^3 \left(\ln(1 - \gamma^2) - \frac{\gamma^2}{\gamma^2 - 1} \right) + \frac{n_0h + \sigma}{3\pi a}. \quad (5.24)$$

The first term in (5.24), expresses the salt advection by mean of the diffusioosmotic velocity, it consists of the diffusioosmotic contribution proportional to the diffusiophoretic mobility $\ln(1 - \gamma^2)$. The second term represent the electroosmotic contribution proportional to the electrophoretic mobility $\gamma^2/\gamma^2 - 1$.

Note that the first term is independent on h , which means that the advection of salt by $v_s(z)$ in the WCA remains always constant.

The third term describes simply, the conduction of the salt content by the thermodynamic force X , it is characterized by two contributions, one from the surface charge density σ , and the other from to the bulk conduction $2\mu n_0 h$.

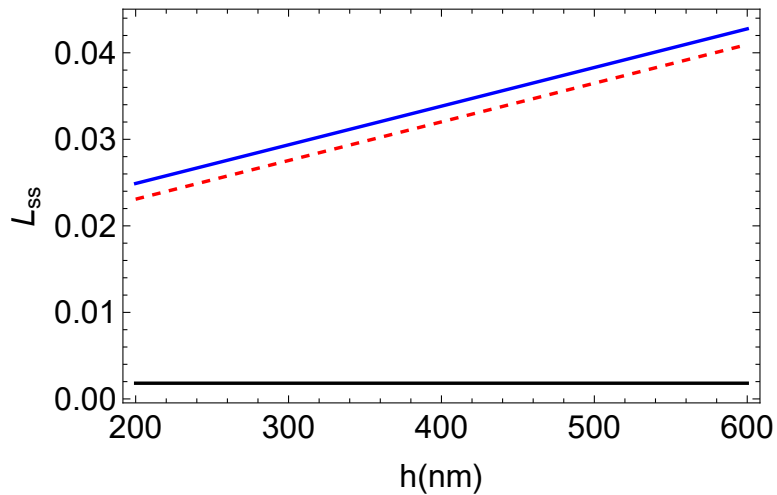


Figure 5.4: Plot of L_{ss} variations as a function of h on a linear scale. The calculations are performed using (CC) boundary condition, with $\sigma = 0.02\text{nm}^{-2}$ and $\lambda = 30\text{nm}$. The black solid line refers to the first term in (5.24), the dashed red line expresses the second term, whereas the blue solid line refers to the combination of both contributions. The variations are plotted in an range of values where the WCA approximation is valid.

The black solid line in the figure above, refers to the first term in L_{ss} , while the red dashed on to the second term which expresses the dominance of the bulk conduction for large separations. The blue solid line expresses the coefficient L_{ss} .

The coefficient L_{sc} describe salt advection by The electroosmotic velocity $v_E(z)$, combined to the charge density conduction by the body force eE ,

$$L_{sc} = -64n_0^2\lambda^3 \left(\frac{\gamma}{-1 + \gamma^2} + \text{arctanh}(\gamma) \right) + 2\mu\sigma. \quad (5.25)$$

The coefficient L_{cs} symmetric to L_{sc} , describe the charge advection by the diffusioosmotic velocity $v_s(z)$, combined to the charge density conduction by the thermodynamic force X .

$$L_{cs} = -64n_0^2\lambda^3 \left(\frac{\gamma}{-1 + \gamma^2} + \text{arctanh}(\gamma) \right) + 2\mu\sigma. \quad (5.26)$$

The variations of these two coefficients, which they are independent on the separation distance h are presented in the figure below.

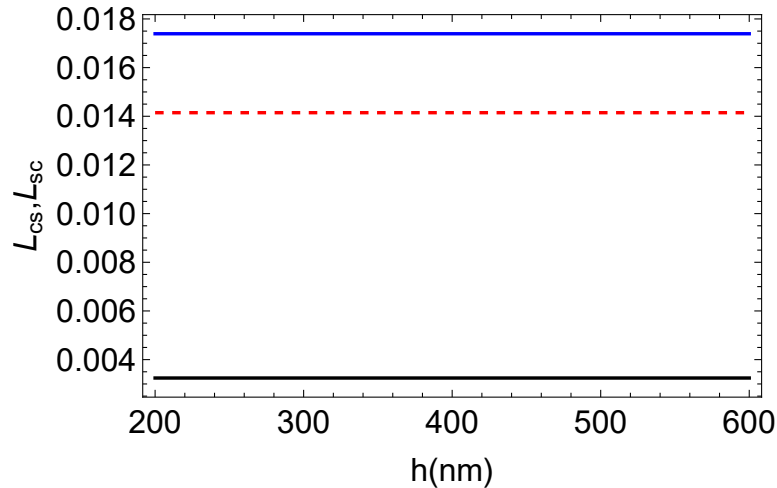


Figure 5.5: Plot of L_{sc} and L_{cs} variations as a function of h in a linear scale. The calculations are performed using (CC) boundary condition, with $\sigma = 0.02\text{nm}^{-2}$ and $\lambda = 30\text{nm}$. The black solid line refers to the first term in (5.26), the dashed red line expresses the second term, whereas the blue solid line refers to the combination of both contributions. The variations are plotted in an range of values where the WCA approximation is valid.

The black solid line in figure 5.5 refers to the first term in L_{cs} , while the red dashed one indicates the charge density conduction and the blue solid line expresses the combination of both contributions.

For more details on Onsager's coefficients expressions in the WCA, see appendix (7.9)

5.2.2 Narrow channel approximation NCA

The study of an electrolyte solution, confined at distances comparable or even smaller than the Debye length λ , is of a primary importance to highlight the new proprieties, that emerges from the electrostatic potential overlapping.

For this purpose let's consider a channel formed by two surfaces located at $z = -h/2$ and $z = h/2$ respectively, where $h \leq \lambda$. When we work on such distances new properties emerge from the overlapping, that occur between the potentials (2.16) of the surfaces, and affect the viscous and electrical properties of the liquid medium. To investigate these proprieties, we use the electrostatic potential given by the equation (2.16).

Since the salt density is involved in the coefficients calculation, it is necessary to remind that the inert quantity of salt must be subtracted from the salt density. We have seen that in the case of a wide channel approximation the subtracted quantity was $2n_0$ [110], for a symmetrical geometry and in the narrow channel approximation the quantity of salt that must be subtracted is $n(0, k)$ which represent the quantity of salt at midplane.

Onsager Coefficients in N.C.A

An approached method relies on Taylor expansions, can be used in order to get the analytic expressions for the coefficients, but this approach is limited just for very small separations h . By expanding the Jacobi's function cd in (2.16) to the second order in z one readily get,

$$\phi(z, k) = \ln(k) - 4\pi l_B \sigma \frac{z^2}{h}, \quad (5.27)$$

with the parameter k given by,

$$k = l_d + \sqrt{1 + l_d^2}, \quad (5.28)$$

$l_d = \sigma/n_0h$ is the Dukhin length, which expresses the ratio between the bulk to the surface charge density contributions, to the electric conductivity.

Like the case of charge-flow coupling, the surface charge $\rho(z)$ is considered to be an homogeneous gas in the NCA. Its analytical expression can be obtained, from the first order of $\sinh \phi$ (2.5) with respect to z ,

$$\rho = \epsilon \partial_z^2 \psi = 2\sigma/h. \quad (5.29)$$

For the effective salt density, we expand $\cosh \phi$ in (5.2) to the second order with respect to z ,

$$\hat{n} = \frac{\sigma^2}{n_0 h^2} \frac{z^2}{\lambda^2} \quad (5.30)$$

$$= n_0 \frac{l_d^2}{\lambda^2} z^2. \quad (5.31)$$

Using (5.29), (5.31) and the general definitions of the symmetrical coefficients (5.9) and (5.18), that translate the diffusioosmotic effect as well as the pressure induced salt current, we can easily derive their analytical expressions given by,

$$L_{sv} = L_{vs} = \frac{\sigma^2 h^3}{240 n_0 \lambda^2}, \quad (5.32)$$

we have seen in the case of the wide channel approximation, that both coefficients are simply given by the diffusiophoretic mobility times the channel height h . In the present case we notice that these coefficients varies as h^3 , these shifts in the height dependency between the two cases are due to overlapping effects.

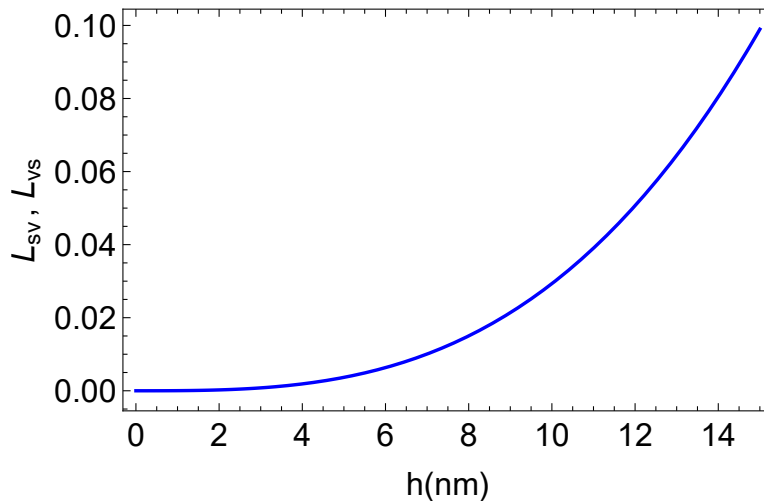


Figure 5.6: L_{sv} and L_{vs} variations as a function of h on a linear scale. The calculations are performed using (CC) boundary condition with $\sigma = 0.02\text{nm}^{-2}$ and $\lambda = 30\text{nm}$. The variations are plotted in an range of values where the NCA approximation is valid.

The advective part (first term) of the coefficient L_{ss} , varies with the separation distance as h^3 , while the second term varies linearly with h . The second term is not dominant as in the case of WCA, and has a little effect as shown in the figure (5.7) (red dashed line). The shift in the channel height dependency in NCA and WCA cases, is due to overlapping effects.

$$L_{ss} = \frac{\sigma^4 h^3}{4032 n_0^2 \lambda^4} + \frac{n_0 h \sqrt{1 + (\sigma/n_0 h)^2}}{3\pi\alpha}. \quad (5.33)$$

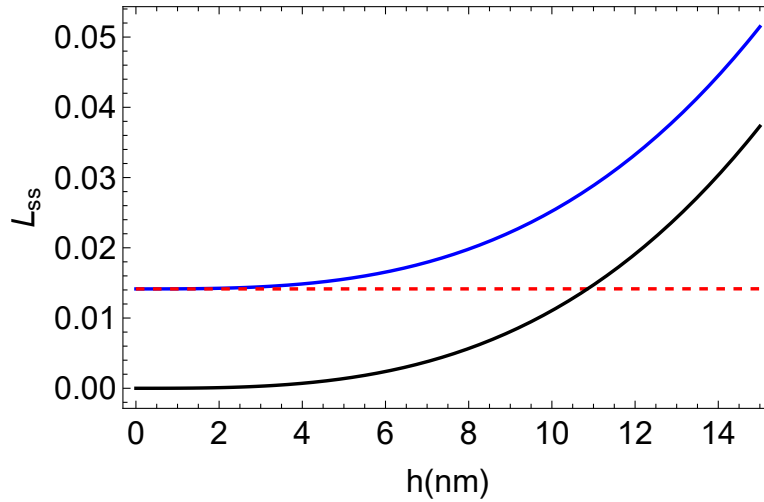


Figure 5.7: Plot of L_{ss} variations as a function of h on a linear scale. The calculations are performed using (CC) boundary condition, with $\sigma = 0.02\text{nm}^{-2}$ and $\lambda = 30\text{nm}$. The black solid line expresses the first term in (5.33), the dashed red line expresses the second term, while the blue solid line refers to the combination of both contributions. The variations of L_{ss} are plotted in an range of values where the NCA approximation is valid.

The same remark is applicable on the coefficients L_{cs} and L_{sc} . Indeed the advective part varies with the separation distance as h^2 , while the conductive part (second term in 5.34) remains the same as in WCA, since coulomb force eE conduction affect all the ions.

$$L_{cs} = L_{sc} = \frac{\sigma^3 h^2}{120 n_0 \lambda^2} + 2\mu\sigma. \quad (5.34)$$

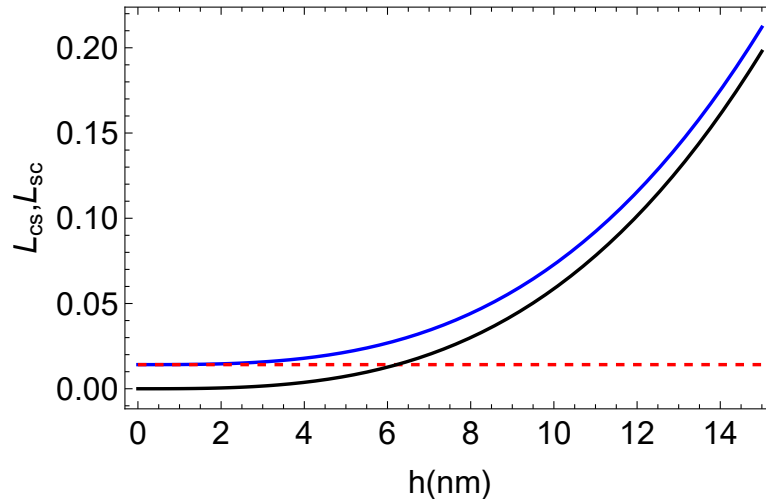


Figure 5.8: Plot of L_{sc} and L_{cs} variations as a function of h on a linear scale. The calculations are performed using (CC) boundary condition, with $\sigma = 0.02\text{nm}^{-2}$ and $\lambda = 30\text{nm}$. The black solid line refers to the first term in (5.34), the dashed red line expresses the second term, whereas the blue solid line refers to the combination of both contributions. The variations are plotted in an range of values where the NCA approximation is valid.

5.3 Salt-charge-flow coupling parameter ξ

After our attempt to interpret the experimental results, of the electroviscous force by the charge-flow coupling only. In the following step we take into account the effect of salt density, and we calculate the coupling coefficient of the salt-charge-flow to investigate its relevance to interpret the experimental findings.

As in the case of charge-flow coupling where we consider that $J_c = 0$. For the salt-charge-flow coupling we consider that the vertical profile of the salt density remains on its equilibrium state, assuming a relative motion of the sphere characterized by low frequencies, which advects a small amount of salt δn in the radial direction. This advected quantity diffuses back to restore the equilibrium state, and we write,

$$J_s = 0. \quad (5.35)$$

In the case of a liquid sample that contains neither charge nor salt, the radial pressure gradient that results from the vertical sphere motions is given by ∇P_0 ,

$$\nabla P_0 = -6\eta r V/h^3, \quad (5.36)$$

the presence of the charge and salt densities modifies the radial pressure gradient, this modification can be evaluated by mean of the coupling parameter ξ .

From the modified pressure gradient ∇P , we can calculate the pressure then the electroviscous force. The expression of the modified pressure gradient can be deduced using Onsager matrix,

$$\nabla P = \mathbf{L}_{vv}^{-1} J_v, \quad (5.37)$$

$J_v = L_{vv} \nabla P_0$ describes the volume current, induced only from the liquid flow in the absence of charge and salt. ∇P is the modified or enhanced pressure gradient. \mathbf{L}_{vv}^{-1} expresses the first element of Onsager's inverse matrix, only this element is taken into

account, since we deal only with the force ∇P , this component translates the effect of charge and salt on the force ∇P ,

$$\nabla P = \mathbf{L}_{vv}^{-1} L_{vv} \nabla P_0. \quad (5.38)$$

The coupling parameter which combine the effects of the charge, salt and volume currents, can be derived from the combination of the currents. The charge current relaxation time is very short compared to the oscillations sphere (7.12), thus the charge current vanishes very quickly $J_c = 0$.

For the salt current, the diffusion of δn advected under the sphere motion, allows the reestablishment of $n(z)$ equilibrium by backdiffusion, thus we write $J_s = 0$. The governing equations for the currents became,

$$J_v = L_{vc} \frac{eE}{\eta} - L_{vv} \frac{\nabla P}{\eta} + L_{vs} \frac{X}{\eta}. \quad (5.39)$$

$$0 = L_{cc} \frac{eE}{\eta} - L_{cv} \frac{\nabla P}{\eta} + L_{cs} \frac{X}{\eta}. \quad (5.40)$$

$$0 = L_{sc} \frac{eE}{\eta} - L_{sv} \frac{\nabla P}{\eta} + L_{ss} \frac{X}{\eta}. \quad (5.41)$$

A simple way to derive the expression of the coupling parameter ξ , is to reexpress the electric field from equation (5.41) as function of X and eE , and insert it in equation (5.40) and (5.39) to get,

$$J_v = - \left(L_{vv} - \frac{L_{cv} L_{vc}}{L_{cc}} \right) \frac{\nabla P}{\eta} + \left(L_{vs} - \frac{L_{vc} L_{cs}}{L_{cc}} \right) \frac{X}{\eta}. \quad (5.42)$$

$$J_s = - \left(L_{sv} - \frac{L_{sc} L_{cv}}{L_{cc}} \right) \frac{\nabla P}{\eta} + \left(L_{ss} - \frac{L_{cs} L_{sc}}{L_{cc}} \right) \frac{X}{\eta}, \quad (5.43)$$

the three equations have been reduced to two equations, which only depend on two forces ∇P and X , with four coefficients which account for the effects of charge, salt and the flow. We can reexpress these equations as,

$$J_v = -L_{VV} \frac{\nabla P}{\eta} + L_{VS} \frac{X}{\eta} \quad (5.44)$$

$$0 = -L_{SV} \frac{\nabla P}{\eta} + L_{SS} \frac{X}{\eta}, \quad (5.45)$$

The coefficients L_{VV}, L_{VS}, L_{SV} and L_{SS} , describe the Poiseuille flow, diffusioosmotic and the salt driven flow by ∇P and the salt advection coefficients. The corrections in (5.42) and (5.43) discard the contributions from the charges and salt to the main processes, therefore the coefficients listed in (5.44 and 5.45) are smaller than the uncorrected ones.

Figure (5.9) shows the variations of, the corrected and the uncorrected diffusioosmotic coefficients (right) as well as the salt conduction (left), as a function of h . The small difference between L_{ss} and L_{SS} is due to the small values of L_{cs} (5.5 and 5.8).

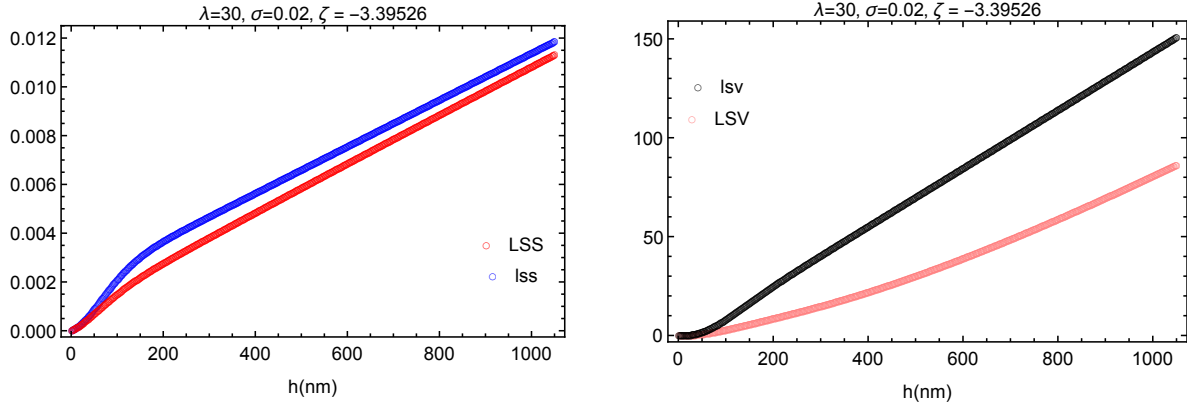


Figure 5.9: Plot of L_{ss} , L_{SS} (left) and L_{sv} , L_{SV} (right) variations as a function of h on a linear scale. The calculations are performed using (CC) boundary condition, with $\sigma = 0.02\text{nm}^{-2}$ and $\lambda = 30\text{nm}$. We notice in both figures that the variations of the corrected coefficients L_{SS} and L_{SV} are smaller compared to the uncorrected coefficients L_{ss} and L_{sv} .

Inserting the expression of X from (5.45) in (5.44) and using the incompressibility condition (7.7), one can readily derive the coupling parameter expression¹,

$$\begin{aligned} \xi &= \frac{L_{SS}(L_{vv} - L_{VV}) + L_{VS}L_{SV}}{L_{vv}L_{SS}} \\ &= \frac{L_{ss}L_{cv}L_{vc} - 2L_{cs}L_{cv}L_{sv} + L_{cc}L_{sv}L_{vs}}{L_{cc}L_{ss}L_{vv} - L_{vv}L_{cs}L_{sc}}, \end{aligned} \quad (5.46)$$

this result is general and it expresses the coupling between salt, charge and liquid flow.

Neglecting some of the off diagonal coefficients which describe the salt or the charge in (5.46), one can deduce the coupling parameters for the charge-flow coupling as well as salt-flow coupling. Indeed if we consider that the off-diagonal elements that describe the salt effect are zeros, we recover the expression of the charge-flow coupling ξ_c ,

$$\xi_c = \frac{L_{cv}L_{vc}}{L_{cc}L_{vv}}. \quad (5.47)$$

In case we consider that the off-diagonal elements which describe the charge effect are zeros, we deduce the expression of the salt-flow coupling ξ_s ,

$$\xi_s = \frac{L_{sv}L_{vs}}{L_{ss}L_{vv}}. \quad (5.48)$$

¹We can deduce the expression of the coupling parameter based on the matrix calculation from the relation $\xi = 1 - 1/L_{vv}\mathbf{L}_{vv}^{-1}$

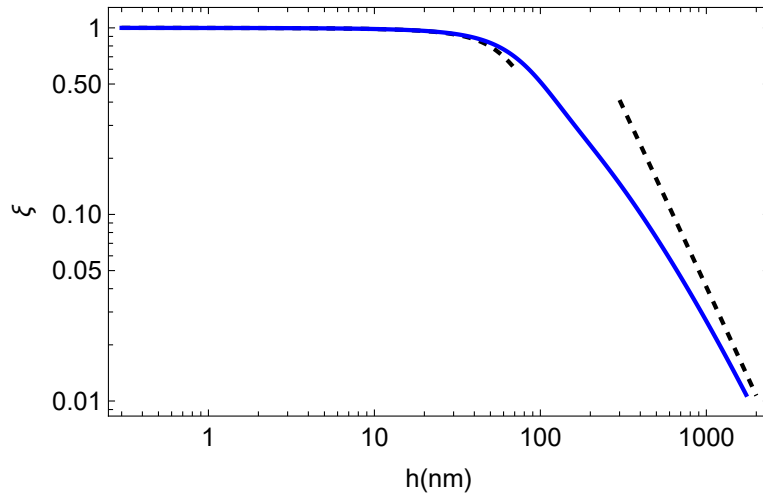


Figure 5.10: Plot of the salt-charge-flow coupling parameter ξ variations as a function of h on a logarithmic scale. The calculations are performed using (CC) boundary conditions with $\sigma = 0.02\text{nm}^{-2}$ and $\lambda = 30\text{nm}$. The dashed black lines refers to the analytic expression of ξ in WCA as well as NCA, whereas the blue solid line refers to the numerical evaluations (7.10).

The salt-charge-flow coupling coefficient varies as h^{-2} for sufficiently large distances as the black dashed line shows in (5.10). While for small separations the coefficient is marked by a plateau as indicated by the black dashed line. The analytic expressions for the parameter ξ in the WCA as well as NCA are given in the appendix (7.13).

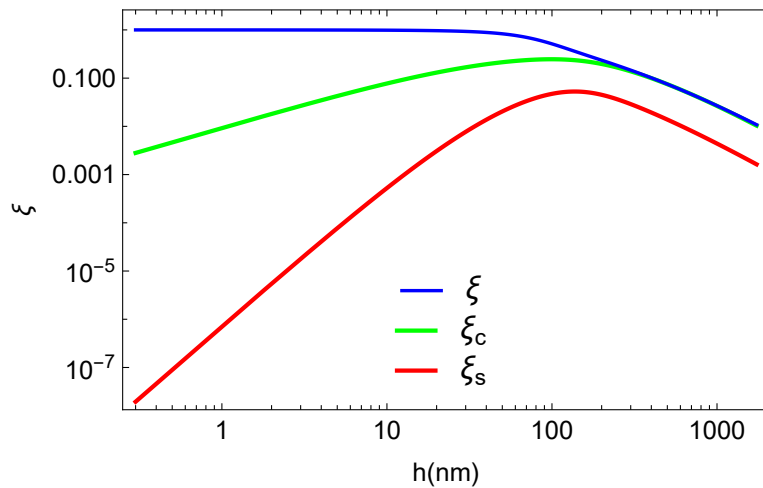


Figure 5.11: Coupling parameters ξ variations as a function of h on a logarithmic scale. the blue curve refers to the salt-charge-flow coupling, the green one to the charge-flow coupling and the red curve to the salt-flow coupling. The coefficients are calculated using (CC) boundary condition with $\sigma = 30\text{nm}^{-2}$.

Figure (5.12) shows the variations of the coupling parameter ξ as a function of h , the slopes of the curves shows that $\xi \propto h^{-2}$ in the case of wide channel approximation. For small separations the dependence in h is different from one curve to another.

It is also remarkable how the salt-flow coupling ξ_s is very weak, compared to ξ and ξ_c especially for small separations. This variations can be explained by the significant values

that $L_{ss}L_{vv}$ may take compared to the coefficients $L_{vs}L_{sv}$ (5.48) and slow back diffusion of the salt.

The salt-charge-flow coupling parameter take significant values and provide an enhancement of 99%, this value can be linked to very small values that the denominator ξ parameter may take, i.e. the values of the quantity $(L_{ss}L_{cc} - L_{cs}^2)$, in the denominator of the parameter ξ worth very small values for small separations.

In order to explain this findings, let's compare the variations of the salt as well as the charge densities. Since the effective salt density $n(z)$ is obtained by subtracting the midplane density from the total salt density, one can deduce that the salt density profile $n(z)$ is comparable to the charge density profile $\rho(z)$, particularly in the range of small separations, as shown in the figure below.

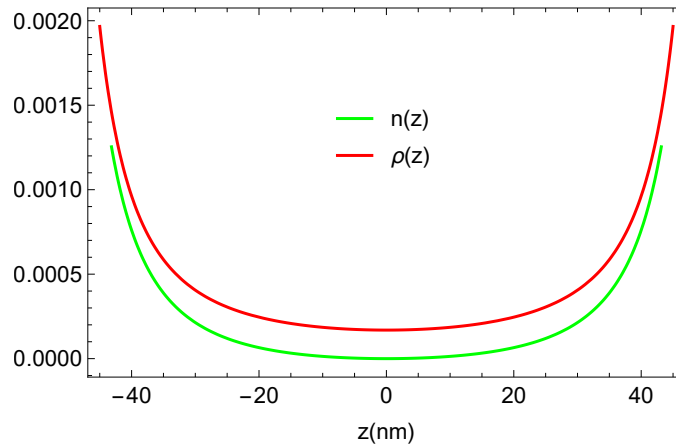


Figure 5.12: Comparison between the variations of $n(z)$ and $\rho(z)$ as a function of z on a linear scale. The calculations of the densities are performed using the (CC) boundary condition with $\sigma = 0.02\text{nm}^{-2}$ and $\lambda = 30\text{nm}$.

Considering the variations of $n(z)$ and $\rho(z)$ in figure (5.12), and the coefficients calculated at the equilibrium state. One can deduce easily that $L_{ss}L_{cc} \sim L_{cs}^2$ (5.46), which explain the small values of the quantity $(L_{ss}L_{cc} - L_{cs}^2)$.

5.4 Electroviscous force

In order to calculate the viscous force enhancement resulting from the salt-charge-flow coupling, we follow the same approach used in the case of charge-flow coupling. Starting from the enhanced gradient of pressure given by,

$$\nabla P = \nabla P_0 \frac{1}{1 - \xi}, \quad (5.49)$$

and calculating the corrected pressure by integrating (5.49), then go up to the viscous force [61], used afterwards to fit the experimental findings,

$$F(h_0) = -2\pi R \int_{h_0}^{\infty} dh P(h). \quad (5.50)$$

From (5.49) one can deduce that the higher coupling effect occur when $\nabla P > \nabla P_0$, and the lower effect when $\nabla P \sim \nabla P_0$. The coupling parameter ξ must be less than 1 in order to maintain the system stable.

The lower sphere surface charge density σ as well as the diffuse layer thickness λ , used in the experiment can be determined by fitting the electrostatic repulsive force with the analytical predictions K (4.39) as we did in the case of charge-flow coupling, illustrated in figure (4.10).

The electroviscous force theoretical predictions based on the salt-charge-flow coupling are compared to the experimental findings used in the previous chapter. For this purpose, we use the same fitting parameters $\sigma = 0.028\text{nm}^{-2}$ and $\lambda = 47\text{nm}$ derived from the figure (4.10).

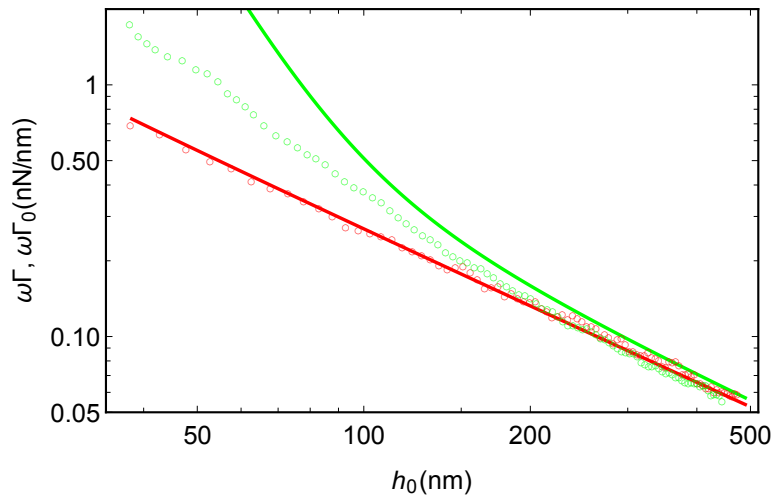


Figure 5.13: Plot of the drag coefficient variations as a function of the separation h_0 on a logarithmic scale. The surface charge density $\sigma = 0.028\text{nm}^{-2}$ and the diffuse layer thickness $\lambda = 47\text{nm}$. The red color refers to the hydrodynamic drag coefficient, while the green color expresses the electroviscous drag coefficient generated from the salt-charge-flow coupling. The open circles account for the averaged experimental data, where each point corresponds to the average value of 100 measurements. The solid lines refers to the theoretical predictions.

Figure (5.13) shows a comparison between the experimental findings (open circles), and the theoretical predictions of the drag coefficient (solid lines), in the presence (green) and the absence (red) of the coupling effects. The experimental hydrodynamic drag match the theoretical predictions, whereas the theoretical prediction over estimate the electroviscous drag especially for small separations where the coupling parameter $\xi \sim 1$. For larger separations the electroviscous drag curve tends to the hydrodynamic drag curve, which characterizes the drag in the bulk region.

The theoretical over estimation of the electroviscous drag coefficient, is simply linked to high values of the parameter ξ therefore to the quantity $(L_{ss}L_{cc} - L_{cs}^2)$ which take very small values.

The small values of $(L_{ss}L_{cc} - L_{cs}^2)$ in ξ , are the result of our assumptions on the salt density profile as well as the salt current. Therefore we can say that the sphere vibrations lead to a significant and permanent deviation of the salt density from its equilibrium state, resulting in a significant salt current $J_s \neq 0$, given the slow back diffusion of the salt.

The only possible way to increase the value of the quantity $(L_{ss}L_{cc} - L_{cs}^2)$, is by evaluating the coefficients depending on the salt in the non equilibrium state, since $\rho(z)$ remains always in the equilibrium state.

It is worth noting that the theoretical predictions of the lift force calculated using the salt-charge-flow coupling parameter, shows an overestimated values compared to the experimental results, in the same way as in the case of the electroviscous force, illustrated in the figure above.

5.5 Conclusion

In this chapter we studied the effect of the salt-charge-flow coupling, on the electroviscous force resulting from the confinement of an electrolyte solution sample between an AFM sphere and a substrate.

The transport coefficients are calculated, using the assumption of a charge and salt densities at the equilibrium state in the normal direction to the substrate.

The first conclusion that can be drawn from this study, is the impossibility to study the forces generated from the perturbations of the electric double layer, by an analytical model which remains valid for all the separations between the sphere and the substrate.

The salt-charge -flow coupling parameter ξ calculated from the transport coefficients in the equilibrium state, revealed an over estimation of the coupling especially for small separations, this over estimation is due to the low values of the quantity $(L_{ss}L_{cc} - L_{cs}^2)$, this conductivity must be increased in order to fit well the the experimental findings of the electroviscous force.

The discrepancy between theory and experiment, clearly indicates the irrelevance of our assumptions, based on a salt density profile which remain on its equilibrium state, under the sphere vibrations. Thus we conclude that the coefficients which depend on the salt density, must be calculated in the non equilibrium state.

In the following chapter we show that the dynamics of the salt content is significantly more complex. In particular we characterize the non equilibrium state of the compensated ions. and we give a method which may lead to a better calculation of the coefficients in the non equilibrium state.

Chapter 6

Perspectives

In this chapter we discuss the out-of-equilibrium state of the ions in thin film. We show that salt density deviates too much from their equilibrium state, under the effect of the sphere vibrations. As a consequence, the transport coefficients L_{ij} must be calculated in the out-of-equilibrium state. Meaning that, Onsager relations that link the currents to the forces, depend in a non linear way to the sphere vibrations.

Finally propose an iterative method to calculate Onsager coefficients, which depend on salt in the out of equilibrium state.

6.1 Out-of-equilibrium ion densities in a narrow channel

It has been concluded from the results of the previous chapter, that the quantity of salt advected from the salt profile in the lubrication zone, is very important and gives rise to significant exchanges with the outer zone .

That is to say that the densities n_{\pm} in the lubrication zone, are significantly modified and remain always far from their equilibrium state, since it depends strongly on the sphere vibrations (time dependence $\partial_t n \neq 0$). Therefore the out of equilibrium salt profile often does not reach its steady state.

The salt density remains far from the equilibrium state, because of the weak thermodynamic force X which does not succeed in counteracting the salt advection, given the slow backdiffusion of the salt.

In the case of sliding motion for example, the sphere according to its radial motion drags a significant quantity of salt. This leads to an accumulation of the salt density in the outer zone as shown in figure (6.1), this difference is due to the very slow backdiffusion of the salt.

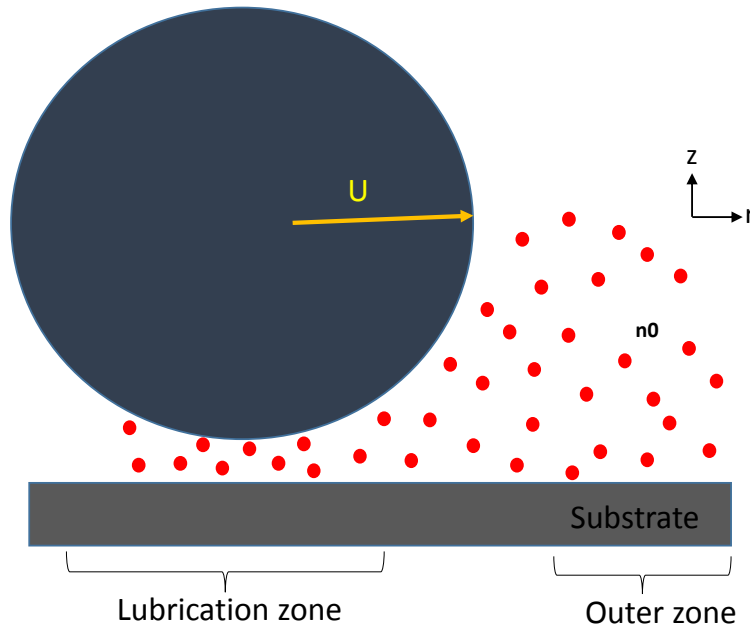


Figure 6.1: Schematic view of the salt advection in the case of a sliding motion. The red circles refer to the salt density in and out the lubrication zone.

Another aspect that must be taken into account for a complete description of the salt content, is the density of the compensated salt which can be defined as,

$$2n_- = n_t - \rho, \quad (6.1)$$

where n_t is the total salt density and ρ is the charge density. The compensated salt (described by the coions density) shows a significant lack compared to the counterions density as shown in figure (6.1),

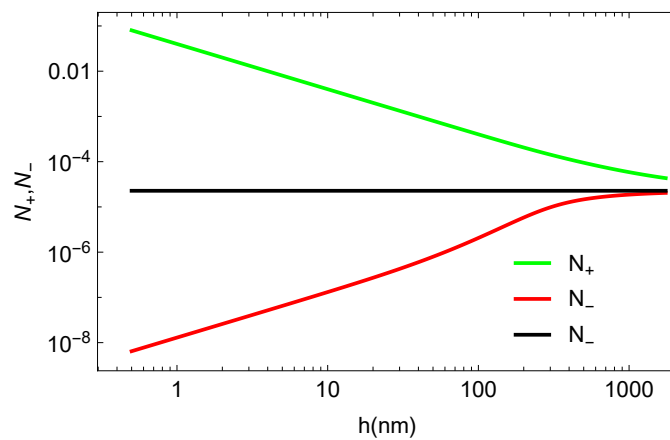


Figure 6.2: Plot of the mean ions densities N_{\pm} as a function of h on a linear scale. N_{\pm} expresses the mean density of coions and counterions, integrated over the channel height. The calculations are performed using (CC) boundary conditions with $\sigma = 0.02\text{nm}^{-2}$ and $\lambda = 30\text{nm}$.

The red lines refers to the counterions density, whereas the green solid lines indicates the coions density. For small separations $h \sim 1\text{nm}$ the counterions density is thousand time smaller than the bulk value, whereas the density of counterions is thousand time larger. For sufficiently large distances $h \sim 1000\text{nm}$ the coions reach the bulk density while the counterions are still more.

The salt advected from the outer zone to the inner zone (the lubrication zone) by mean of the sphere decompression, leads to an increase in the density of the compensated salt in the lubrication zone, consequently an increase in the salt-charge-flow coupling.

6.2 Out of equilibrium Onsager coefficients

Knowing that the salt density in the radial direction is mainly in the non equilibrium state. We can express the salt content as a profile which remains in the steady state following the vertical coordinate z , times a radial salt density that remains in non equilibrium state. Thus Onsager coefficients dependent on the salt can be reexpressed as,

$$L_{sv} = NM_{sv}, \quad L_{ss} = NM_{ss}^{(1)} + N^2M_{ss}^{(2)}, \quad L_{sc} = NM_{sc}, \quad (6.2)$$

where N express the salt density integrated over the channel height h . M_{ij} is a profile independent on the radial salt, but depend on the vertical coordinate z . If the coefficient L_{ss} for example, we have the first term which express the salt advection by mean of the diffusioosmotic velocity, and a second term account for the conduction by mean of the force X .

The coefficients M_{ij} are calculated from the mean value of $\cosh \hat{\Psi}$, integrated over the separation distance h . Where the function $\cosh \hat{\Psi}$ is given by,

$$\cosh \hat{\Psi} = \hat{k} \text{cd} \left(\frac{z}{\sqrt{\hat{k}\lambda}} | \hat{k}^2 \right)^2 + \hat{k}^{-1} \text{cd} \left(\frac{z}{\sqrt{\hat{k}\lambda}} | \hat{k}^2 \right)^{-2}, \quad (6.3)$$

where the electric potential Ψ expressed in term of Jacobi's functions, is evaluated in the out of equilibrium state, i.e the salt density variations between the inner and outer zone modifies the salinity in the lubrication zone, thus the diffuse layer thickness expressed by Debye length λ and the parameter k in (2.16) varies. As a consequence Ψ must be calculated in the out of equilibrium state.

Once the coefficients are calculated in the out of equilibrium state, one use the corrected gradient pressure in order to calculate the electroviscous force with the correction parameter ξ as we did in the chapter 4 and 5.

6.3 Slow relaxation of excess salinity

We define the relaxation time as the time required for the salt to recover its equilibrium state after advection. The radial relaxation time can be estimated by,

$$\tau_r = \frac{r^2}{D}, \quad (6.4)$$

r is the distance of the particle from its starting position at time t , which can be approximated by $r \sim \sqrt{R\bar{h}_0}$.

For $R = 47\mu\text{m}$, $h_0 = 50\text{nm}$ for a narrow channel, and a diffusion coefficient $D \sim 10^{-9}\text{m}^2/\text{s}$ one find $\tau_s = 2.35 \times 10^{-3}\text{s}$ which is slightly smaller than the sphere vibrations frequencies $\omega_0^{-1} \sim 10^{-2}\text{s}$.

We notice a big difference between the relaxation time of the charge density compared to the salt density relaxation time, we have $\tau_c \ll \tau_s$. This difference can be explained by, the weakness of the thermodynamic force X compared to Coulomb force generated after the charge advection.

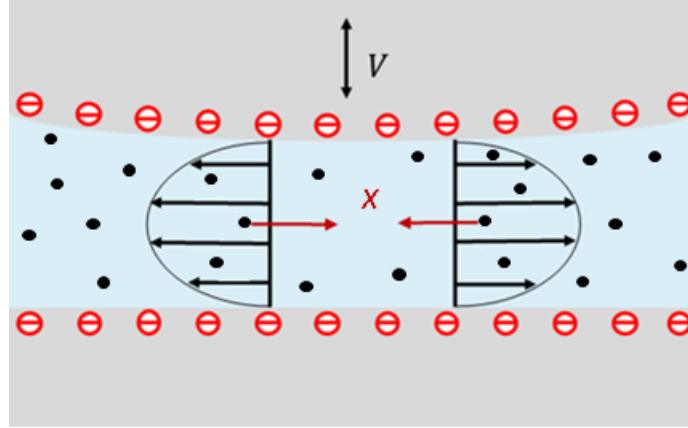


Figure 6.3: Schematic view of the thermodynamic force X effect, on the salt density. The black circles refers to the salt density. The black arrows to the salt advection, whereas the red arrows designate the effect of the force X , generated from the salt backdiffusion

Figure (6.4) shows a comparison between the variations of the elastic response in the static case as well as the dynamic case,

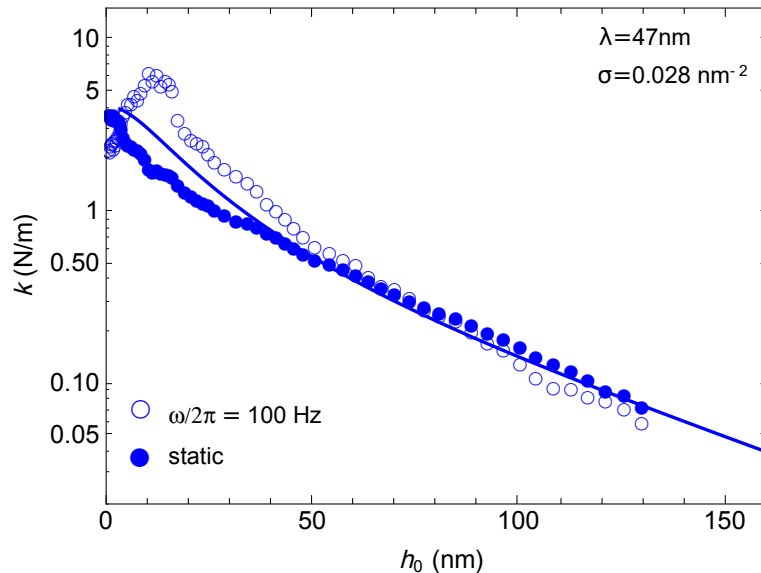


Figure 6.4: Elastic response variations as a function of h_0 on a log-linear scale. The calculations are performed using (CC) boundary condition with $\sigma = 0.028\text{nm}^{-2}$. The solid line refers to the theoretical predictions for the static response. The filled and the empty circles refers to the measured elastic response in the static and the dynamic case respectively.

For small separations where $h_0 < \lambda$, the measured elastic response at $\omega_0 = 100\text{Hz}$ shows a difference from the response measured at the static state. The figure shows the evidence of the elastic response dependence of the sphere vibration frequencies, this dependence is the result of the phase shift between the vibration time and the salt diffusion.

6.4 Discretization of the salt dynamics

Let's consider a radial salt current density generated from the relative motion of the sphere, the current combine the salt advection by the velocity field with the conduction of the salt,

$$J_s = n_t(z)v(z) + \mu n_t X - D\nabla n_t, \quad (6.5)$$

where n_t is the salt density, $D = k_B T \mu$ the diffusion coefficient, v the velocity profile and X is the thermodynamic force (2.32), we choose the radial coordinate for convince in order to evaluate the continuity equation given by,

$$\partial_t n = -\nabla \cdot J_s = -\frac{\partial_r(r J_s)}{r}. \quad (6.6)$$

The discretization consist of evaluating the continuity equation, as well as the salt current density, on a lattice which expresses the radial distance r in a discrete way as $r_q = qa$, where a the step and q the number of steps. The salt current density can be written following this model as,

$$J_q = v_q n_q + \mu f_q n_q - D(n_{q+1} - n_q). \quad (6.7)$$

From the continuity equation we can deduce the local variation of the salt density, in every site in the lattice during a given times τ as,

$$\delta n_q = \tau \partial_t n_q = \tau \frac{r_{q-1} J_{q-1} - r_q J_q}{r_q}. \quad (6.8)$$

The salt density in the steady state can be determined, by iterating equation (6.7) and (6.8) with the iteration step $n_q \rightarrow n_q + \delta n_q$.

The salt density in the steady state expresses the salt density which remain unchanged, in the lubrication area regardless the exchanges that can take place between the reservoirs and the lubrication area.

we consider that the force X as well as the velocity profile v vanishes out of the lubrication zone (the reservoirs). For this purpose we set an upper value m for the number of steps in which this conditions for X and v comes true, at the steady state and far enough of the solid surfaces the salt density equals the bulk density $n_m = n_0$ this condition closes the equations (6.7) and (6.8).

This iterative method allows to calculate the new out-of-equilibrium salt density $N = \int n ds$ and calculate afterwards the values of the non-equilibrium Onsager coefficients.

Chapter 7

Appendices

7.1 Osmotic pressure

In the introduction we gave a brief discussion on the osmotic pressure process, which occurs when two solutions characterized by two different concentrations are separated by a permeable membrane.

Solvent molecules are transferred from the solution, with a lower concentration to the solution with a higher concentration of solute, this transfer continues until reaching the equilibrium.

In a confined geometry its already known, that the distribution of the counter ions is governed by the electrostatic interactions and the entropy between them. The counter ions radial pressure in the gape between two flat surfaces can be given by [21],

$$\partial_z P = \rho \partial_z \mu, \quad (7.1)$$

where μ is the chemical potential and ρ is the charge density. We know that the charge density profile variations occur between the solid surface and the bulk, where the charge density is almost zero in the bulk.

From these considerations we integrate the equation (7.1) from the position of the solid surface a to the bulk (∞), the evaluation of these integral yields,

$$P(\infty) - P(a) = \int_a^\infty \left(\rho \partial_z \phi(z) dz + k_B T \partial_z \rho dz \right) \quad (7.2)$$

$$P(\infty) - P(a) = \int_a^\infty \left(\rho \partial_z \phi(z) dz + k_B T d\rho \right), \quad (7.3)$$

with $\phi(z)$ the electrostatic potential given by (2.10), in the bulk region where the charge density vanishes, we consider that the osmotic pressure vanishes as well. Using Poisson's equation we get,

$$P(a) = - \int_a^\infty \left(- \partial_z^2 \phi(z) \partial_z \phi(z) dz + k_B T d\rho \right), \quad (7.4)$$

the first term of integration in equation(7.4) can be simplified by mean of the equation,

$$\partial_z \phi(z) \partial_z^2 \phi(z) = \frac{1}{2} \partial_z (\partial_z \phi(z))^2, \quad (7.5)$$

equation (7.4) and (7.5) yields,

$$P(a) = \left(- \frac{1}{2} (\partial_z \phi(z))_\infty^2 + k_B T \rho_\infty \right) - \left(- \frac{1}{2} (\partial_z \phi(z))_a^2 + k_B T \rho_a \right), \quad (7.6)$$

its already known that Boltzmann distribution, relates the charge distribution to the electrostatic potential by mean of Boltzmann factor. Thus in order to simplify (7.6) we differentiate the charge density with respect to z ,

$$\partial_z \rho = \rho_0 \partial_z \phi(z) e^{-\phi(z)} \quad (7.7)$$

$$= \rho \partial_z \phi(z), \quad (7.8)$$

using equation (7.5) and Poisson's relation on ρ , one readily get,

$$\partial_z \rho = \frac{-1}{2} \partial_z (\partial_z \phi(z))^2, \quad (7.9)$$

the integration of the equation above reflects the relationship, between the charge density variations and the generated electrostatic pressure. The difference between the charge density in the vicinity of the solid surface and the bulk give rise to an electrostatic pressure.

$$\rho = \rho_0 + \frac{1}{2} (\partial_z \phi(z))^2, \quad (7.10)$$

by associating equation (7.6) to (7.10) and considering the charge density in the bulk equal to zero, we find the expression of the osmotic pressure given by,

$$P_O = \rho k_B T, \quad (7.11)$$

in the case of the osmotic pressure generated by the salt content, the expression (7.11) remains the same except that, instead of taking the charge density as a source of pressure, we take the effective salt density $n(z)$ we get,

$$P_0 = n(z) k_B T, \quad (7.12)$$

with $n(z)$ is simply given by,

$$n(z) = n_t(z) - n_0, \quad (7.13)$$

where n_0 is the inert quantity of salt in the present case of (infinite half-space), for the case of two surfaces confining a sample of an electrolyte solution the inert quantity equal to the quantity of salt at midplane $n(0)$.

7.2 Diffusioosmotic pressure gradient

To give more insights about the diffusioosmosis effects, let's consider an electrolyte solution interacting only with a solid surface through a potential $\kappa(z)$. At the thermal equilibrium the salt content is governed by Boltzmann distribution given by,

$$n(z) = n_0 e^{-\kappa(z)/k_B T}, \quad (7.14)$$

where n_0 is the bulk density, k_B Boltzmann constant and T is the temperature. The interaction is assumed to be in the normal direction to the solid surface along the diffuse layer length λ .

If the potential of interaction $\kappa(z)$ is positive, the quantity of salt in the vicinity of the solid surface is much smaller then the bulk quantity n_0 (a depletion near the solid surface), meaning that for a positive potential the interaction is repulsive. For a negative

potential the interaction is attractive and therefore there is an accumulation of salt near to the solid surface [110].

The application of a salt gradient ∇n_0 parallel to the solid surface generate a salt current but do not induces a flow, in fact this applied gradient in the bulk give rise to an osmotic pressure, balanced by the hydrostatic pressure P_h , thus the pressure in the radial direction in the bulk remains always steady, hence the absence of a flow in the region far from the solid surface (the bulk),

$$k_B T n(r) - P_h = \text{constant}. \quad (7.15)$$

However near the solid surface, within the diffuse layer thickness λ in the normal direction to the solid surface, the equilibrium between salt density and pressure can be reached in a time very small compared to the relaxation time of the salt gradient. Hence equation (7.14) can be reexpressed as a radial density n_0 times a given function which describes as,

$$n(r, z) = n_0(r) e^{-\kappa(z)/k_B T}, \quad (7.16)$$

where the fast variations of the exponential function, describe the interactions between the salt gradient and the solid surface and $n_0(r)$ account for the radial extension of the salt.

In the normal direction, the equilibrium between the pressure gradient and the osmotic pressure gradient yields,

$$-\partial_z P(r, z) - \partial_z \kappa(z) n(r, z) = 0, \quad (7.17)$$

the association of equation (7.16) with the equation (7.17), integrated with respect to z yields,

$$P(r, z) - k_B T n(r, z) = P_h - k_B T n(r) = \text{constant} \quad (7.18)$$

Equation (7.18) describe the pressure variations, induced from the salt content variations near and far from the solid surface.

In order to highlight the effect of these variations on the flow generation, we need simply to differentiate this equation with respect to the radial coordinate r .

$$\partial_r P = k_B T \partial_r \left(n(r, z) - n_0(r) \right) \quad (7.19)$$

7.3 AFM measurement

In this section we give a brief description of the Atomic force microscopy (AFM) functioning. The technique used by our colleague in the group MAALI Abdelhamid, to carry out the experimental measurement on the electroviscous force as well as the electrokinetic lift force. The data from his measurements are used afterwards to compare the relevance of our theoretical model based on the charge-flow as well as the salt-charge-flow evaluated in the equilibrium state.

The experimental setup consists of an electrolyte solution, confined between a flat solid substrate (mica) and a lower surface of a vibrating sphere with $47\mu\text{m}$ radius R mounted on the cantilever of an AFM. For a general functioning the assembly sphere/cantilever commonly referred to as the probe scans the sample surface by up and down, side to side motion. The probe is monitored through a laser beam reflected from the cantilever to a photo-detector as shown in the figure (7.1).

The detector measure the cantilever deflections and covert it to an electrical signal, the intensity of the signal is proportional to the cantilever displacement [112].

In order to measure the force which rises from the contact between the tip and the electrolyte sample, we consider that the tip is vibrating vertically near to its resonance frequency with a sinusoidal motion,

$$Z = A \sin(\omega_0 t), \quad (7.20)$$

a feedback loop is used in this mode to ensure a constant amplitude of vibrations, very small compared to the film width h_0 ($A \ll h_0$).

The tip velocity given by the black arrow in the figure (7.1) can be expressed as,

$$V = \dot{Z}(t) = A\omega_0 \cos(\omega_0 t), \quad (7.21)$$

where ω_0 and A are the vibrations sphere frequency and amplitude respectively.

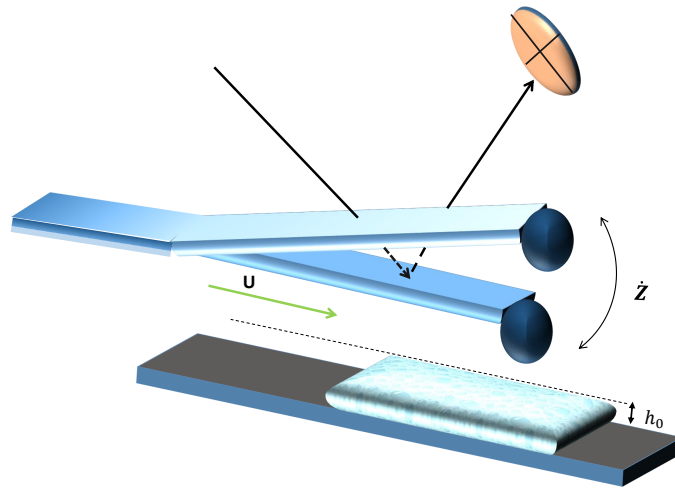


Figure 7.1: Experimental setup scheme

The tip vibrations induce a flow that disturb the static equilibrium of the diffuse layer content. The distortion of the EDL lead to many dynamic effects, thus the generation of different type of forces sensed by the tip. It is worth to mention that the AFM measurements can be extended for the study of two parallel sliding surfaces effects, using a tip with a transnational motion in the radial direction, with respect to the subtract as shown in the figure above (green arrow), U is the radial velocity which characterizes the sliding motion.

7.4 PB equation solution in asymmetric geometry

We can get the solution of the equation 2.6 by multiplying both sides by $2\nabla\phi$ to get,

$$2\nabla\phi\nabla^2\phi = 2\nabla\phi\frac{1}{\lambda^2}\sinh\phi, \quad (7.22)$$

with $\phi = e\psi/k_B T$ is a normalized potential, the integration of the left side yields,

$$2\nabla\phi\nabla^2\phi = \nabla(\nabla\phi)^2, \quad (7.23)$$

inserting (7.23) in (7.22) and performing integration of it, one gets,

$$\nabla\phi = \pm\sqrt{\frac{2}{\lambda^2}(\cosh(\phi) + c_1)}, \quad (7.24)$$

in order to determine the constant c_1 , we consider the limits where $z \rightarrow \infty$, in this case $\phi \rightarrow 0$ and $\nabla\phi \rightarrow 0$, yielding,

$$\nabla\phi = \pm\frac{2}{\lambda}\sinh\frac{\phi}{2}, \quad (7.25)$$

here the surface charge σ is a negative quantity, so $\phi < 0$ and $\nabla\phi > 0$, thus we choose the negative solution,

$$\nabla\phi = -\frac{2}{\lambda}\sinh\frac{\phi}{2}, \quad (7.26)$$

The integration of the equation (7.26) yields the analytic expression of the electrostatic potential [21,31],

$$\begin{aligned} \phi &= \int \frac{d\phi}{\sinh(\frac{\phi}{2})} = -\frac{2}{\lambda} \int dz \\ &= 2 \ln \left(\frac{1 + \gamma e^{-\frac{z}{\lambda}}}{1 - \gamma e^{-\frac{z}{\lambda}}} \right). \end{aligned} \quad (7.27)$$

In order to define the integration constant γ , we use the charge constant boundary condition (CC) given by,

$$\phi'(0) = \frac{-\sigma}{\epsilon}, \quad (7.28)$$

evaluating the equation (7.4) at $z = 0$, one can get the equation which relates γ to the potential at the surface ϕ_0 .

$$\phi_0 = -4\text{arcth}(\gamma), \quad (7.29)$$

with,

$$\gamma = \sqrt{(b/\lambda)^2 + 1} - b/\lambda. \quad (7.30)$$

7.5 PB equation solution in symmetric geometry

In order to establish the electrostatic potential in the symmetric case, we consider an electric field that vanishes at the midplane [82],

$$-\frac{\partial\phi}{\partial z}\Big|_{z=0} = 0 \quad (7.31)$$

applying this condition on (7.24) one gets,

$$\nabla\phi = \pm\sqrt{\frac{2}{\lambda^2}(\cosh(\phi) + \cosh\phi(0))}, \quad (7.32)$$

by introducing the variable,

$$\Phi = e^{\phi/\kappa} \quad (7.33)$$

$$\kappa = e^{\phi(0)}, \quad (7.34)$$

and considering a negative surface charge density, including (7.33) and (7.34) in (7.32) one gets,

$$\frac{d\Phi}{\sqrt{\Phi(1-\Phi)(1-\kappa^2\Phi)}} = \frac{-dz}{\lambda\kappa}, \quad (7.35)$$

considering $\Phi = \sin^2 \theta$ and insert it in (7.35), one gets after integration,

$$\frac{-z}{\lambda\kappa} = \int_{\pi/2}^{\arcsin \sqrt{\Phi}} \frac{d\theta}{\sqrt{1-\kappa^2 \sin^2 \theta}} \quad (7.36)$$

with $\varphi = \arcsin \sqrt{\Phi}$, we define the incomplete elliptic integral of a first kind as,

$$u = \int_0^\varphi \frac{d\theta}{\sqrt{1-k \sin^2 \theta}} = F(\varphi|k) \quad (7.37)$$

with the corresponding complete integral $F(\pi/2|k)$. The inversion of the Jacobi amplitude u , yields the function $sn(u|k)$ given by,

$$\text{sn}(u|k) = \sin \varphi \quad (7.38)$$

with,

$$\text{cn}(u|k) = \sqrt{1 - \text{sn}^2(u|k)} \quad (7.39)$$

$$\text{dn}(u|k) = \sqrt{1 - \text{cn}^2(u|k)} \quad (7.40)$$

$$\text{cd}(u|k) = \text{cn}(u|k)/\text{dn}(u|k), \quad (7.41)$$

performing the integral of (7.36) one gets,

$$\int_{\pi/2}^{\arcsin \sqrt{\Phi}} \frac{d\theta}{\sqrt{1-\kappa^2 \sin^2 \theta}} = \int_0^\varphi \frac{d\theta}{\sqrt{1-\kappa^2 \sin^2 \theta}} - \int_0^{\pi/2} \frac{d\theta}{\sqrt{1-\kappa^2 \sin^2 \theta}} \quad (7.42)$$

$$\frac{-z}{\lambda\kappa} = -u = \text{sn}^{-1} \sqrt{\Phi} - K(\kappa), \quad (7.43)$$

using the periodicity condition $\text{cd}(u|k) = \text{sn}(K(k) - u|k)$ we find,

$$\Phi = \text{sn}^2(K(k) - u) = \text{cd}^2(u|k^2) \quad (7.44)$$

using (7.33) and applying the logarithm function \ln , we recover the electrostatic potential given by

$$\phi = \ln k + 2 \ln \text{cd}(u|k^2), \quad (7.45)$$

using(7.43) we get the argument $u = z/2\lambda\sqrt{k}$, thus for the function cd we get,

$$\text{cd}(z, k) = \text{JacobiCD}\left(\frac{z}{2\lambda\sqrt{k}}, k^2\right) \quad (7.46)$$

7.6 Velocity profile components

This section provides the complete calculation of the velocity profile $v(z)$ components, and gives more details on the double integration calculation of the velocity $v(z)$ from Stokes equation. We privilege the symmetric geometry where the lower sphere surface is located at $z = h/2$ and the immobile substrate surface at $z = -h/2$.

The velocity profile components are derived from the double integration of the Stokes equation given by (3.21).

7.6.1 Pressure driven velocity

The first component is the pressure driven velocity obtained from (3.21). Considering the situation where a viscous liquid is confined between two uncharged solid surfaces, this is practically realized by setting both eE and $\nabla \ln \hat{n}_0$ equal to zero,

$$\eta \partial_z^2 v_p = \nabla P, \quad (7.47)$$

this equation requires the performance of a double integration taking into account two boundary conditions. The first is the variations of the shear stress which we consider null at the midplane of the channel, where the velocity profile reaches its maximum value $v(0) = v_{max}$,

$$\tau = \eta \partial_z v_{max} = 0, \quad (7.48)$$

this condition is the result of the symmetry in the velocity profile, imposed the non slip condition (the second boundary condition) on the two surfaces $v(\pm h/2) = 0$,

$$\eta \int_0^{z'} \partial_{z''}^2 v_p(z'') dz'' = \int_0^{z'} dz'' \nabla P \quad (7.49)$$

$$\eta \left(\partial_{z'} v_p(z') - \partial_{z'} v_p(0) \right) = z' \nabla P, \quad (7.50)$$

where $\eta \partial_{z'} v_p(0)$, is the dynamic constraint which vanishes at the midplane, the first integration yields,

$$\eta \partial_{z'} v_p(z') = z' \nabla P, \quad (7.51)$$

and the second integration yields,

$$\int_z^{h/2} \partial_{z'} v_p(z') dz' = \frac{1}{\eta} \int_z^{h/2} z' dz' \nabla P \quad (7.52)$$

$$v_p(h/2) - v_p(z) = \frac{h^2 - 4z^2}{8\eta} \nabla P, \quad (7.53)$$

using the non slip boundary condition, one readily finds that $v_p(h/2) = 0$. Thus the pressure driven velocity is simply given by [96],

$$v_p(z) = -\frac{h^2 - 4z^2}{8\eta} \nabla P. \quad (7.54)$$

The type of substrate used in liquid confinement, can significantly affect the velocity profile at the liquid/solid interface. In such cases we use the slip boundary condition related to a slip length b , defined as an extrapolated distance relative to the wall where the tangential velocity component vanishes. This length relates the velocity profile near the wall to the shear rate,

$$v_p(h/2) = b \partial_z v_p(z)|_{h/2} \quad (7.55)$$

$$= -b \frac{h}{2\eta} \nabla P, \quad (7.56)$$

therefore the pressure driven velocity in the case of slip length can be given by,

$$v_p(z) = -\frac{h^2 - 4z^2}{8\eta} \nabla P - b \frac{h}{2\eta} \nabla P. \quad (7.57)$$

7.6.2 Electroosmotic velocity

The electroosmotic velocity $v_E(z)$ describes the profile generated from the diffuse layer content, this latter can be derived from (3.21), by taking both the forces ∇P and $\nabla \ln \hat{n}_0$ equal to zero,

$$\eta \partial_z^2 v_E = \rho e E, \quad (7.58)$$

the integration and boundary conditions used to determine the profile of the electroosmotic velocity, remain the same as the case of the pressure driven velocity $v_p(z)$. In order to simplify the integration, let's use Poisson's equation which allow to replace the charge density ρ , by the second derivative of the electrostatic potential ϕ

The first integration provides the shear stress variations which vanishes at midplane,

$$\eta \int_0^{z'} \partial_{z''}^2 v_E(z'') dz'' = \epsilon \int_0^{z'} \partial_{z''}^2 \phi(z'') dz'' e E \quad (7.59)$$

$$\eta \left(\partial_{z'} v_E(z') - \partial_{z'} v_E(0) \right) = \epsilon \left(\partial_{z'} \phi(z') - \partial_{z'} \phi(0) \right) e E, \quad (7.60)$$

where $\eta \partial_{z'} v_p(0)$ and $\partial_{z'} \phi(0)$ is the shear stress and the electric field respectively, which vanishes at the midplane, thus the first integration yields,

$$\eta \partial_{z'} v_E(z') = \epsilon \partial_{z'} \phi(z') e E, \quad (7.61)$$

performing the second integration one can readily finds,

$$\int_z^{h/2} \partial_{z'} v_p(z') dz' = \frac{\epsilon}{\eta} \int_z^{h/2} \partial_{z'} \phi(z') e E \quad (7.62)$$

$$v_E(h/2) - v_E(z) = \frac{\epsilon}{\eta} (\phi_0 - \phi(z)) e E, \quad (7.63)$$

using the non slip boundary condition $v(h/2) = 0$, and the electrostatic potential value at the solid/liquid interface $\hat{\psi}(\pm h/2) = \phi_0$, one finds [97],

$$v_E(z) = \frac{\epsilon}{\eta} (\phi(z) - \phi_0) e E. \quad (7.64)$$

In the case of slip boundary condition. The velocity profile near the wall is related to the shear rate by,

$$v_E(h/2) = b \partial_z v_E(z)|_{h/2} \quad (7.65)$$

$$= -b \frac{\epsilon}{\eta} \phi'(h/2) e E, \quad (7.66)$$

therefore the electroosmotic velocity in the case of slip length can be given by,

$$v_E(z) = \frac{\epsilon}{\eta} (\phi(z) - \vartheta) e E, \quad (7.67)$$

where $\vartheta = \phi_0 \left(1 - b \frac{\phi'(h/2)}{\phi_0} \right)$, is the new value of the electrostatic potential at the solid/liquid interface ϑ shows the effect of the slip length b on ϕ_0 potential.

7.6.3 Diffusioosmotic velocity

The last component is the diffusioosmotic velocity, which describe the profile generated from the salt density profile, derived from (3.21) by taking both forces ∇P and eE equal to zero,

$$\eta \partial_z^2 v_E = n(z)X, \quad (7.68)$$

with $n(z)$ the effective salt density derived from the subtraction of the inert salt density, at midplane from the total salt density.

Unlike the electroosmotic velocity profile, the establishment of a general and simple analytic expression for the diffusioosmotic velocity $v_s(z)$ is impossible, since the salt density can not be linked to the electrostatic potential by Poisson's equation. Thus the diffusioosmotic velocity profile can be calculated as,

$$v_s(z) = \frac{H(z)}{\eta} X, \quad (7.69)$$

where $H(z)$ is the diffusiophoretic mobility [98] calculated from the Stokes equation. By performing the double integration of the salt density taking in account the boundary conditions related to the shear stress and the non slip conditions,

$$H(z) = \int_z^{h/2} dz' \int_0^{z'} dz'' n(z''). \quad (7.70)$$

The diffusioosmotic velocity can be calculated as well in the case of a slip length by evaluating the equation,

$$v_s(h/2) = b \partial_z v_s(z)|_{h/2}. \quad (7.71)$$

7.7 Incompressibility condition

The channel height modulated by the sphere vibrations can be expressed as,

$$h(r, t) = h_0 + Z(t) + \frac{r^2}{2R}, \quad (7.72)$$

where h_0 is the minimum channel height and $Z(t)$ is the tip-sample surface.

In case where the sphere moves in the normal direction to the substrate (squeezing motion) as well as in the radial direction (sliding motion), we express the sphere velocity by,

$$\frac{dh}{dt} = v = \frac{\partial Z}{\partial t} + U \frac{\partial h}{\partial r}, \quad (7.73)$$

for the squeezing motion, only the vertical oscillations of the sphere are retained. Thus the volume flow J_v can be given simply by integrating the velocity profile v over the channel height [91],

$$J_V = \int v dz, \quad (7.74)$$

locally the divergence of the volume flow yields the velocity profile $\nabla \cdot J_v = v = dZ/dt$. Expressing the divergence operator in the radial coordinate we get,

$$\frac{\partial Z}{\partial t} = \frac{1}{r} \frac{\partial r J_V}{\partial r}, \quad (7.75)$$

performing the integration of (7.75) one get,

$$J_V = \frac{rV}{2}. \quad (7.76)$$

7.8 Charge and salt profiles in the WCA

In the wide channel approximation (infinite half-space), where the solid surface at a position $z = 0$ we consider that $h \gg \lambda$, thus we can set $h \rightarrow \infty$.

The radial counterions density determined simply by performing the integral of n_+ from the solid surface position $z = 0$ to infinity,

$$\int_0^\infty n_+(z)dz = \int_0^\infty n_0 \left(\frac{1 + \gamma e^{-z/\lambda}}{1 - \gamma e^{-z/\lambda}} \right) dz \quad (7.77)$$

$$= n_0 h - 2n_0 \lambda + \sigma + \frac{1}{2} \sqrt{16n_0^2 \lambda^2 + \sigma^2}, \quad (7.78)$$

and the radial coions density yields,

$$\int_0^\infty n_-(z)dz = \int_0^\infty n_0 \left(\frac{1 - \gamma e^{-z/\lambda}}{1 + \gamma e^{-z/\lambda}} \right) dz \quad (7.79)$$

$$= n_0 h - 2n_0 \lambda - \sigma + \frac{1}{2} \sqrt{16n_0^2 \lambda^2 + \sigma^2}, \quad (7.80)$$

yielding a radial charge density,

$$C = 2\sigma, \quad (7.81)$$

and a radial salt density ,

$$N = 2n_0 h - 4n_0 \lambda + \sqrt{16n_0^2 \lambda^2 + \sigma^2}, \quad (7.82)$$

after subtraction of the integrated inert salt value $2n_0 h$ one get,

$$N = -4n_0 \lambda + \sqrt{16n_0^2 \lambda^2 + \sigma^2} \quad (7.83)$$

In case where the electrostatic potential is very weak. One use Debye Hückel approximation to derive the analytic expression of C and N , see appendix (7.14)

7.9 Onsager coefficients in WCA

In this section we provide an illustration of how to calculate the analytical expressions of Onsager's coefficients. Taking as a first example the coefficient L_{cv} which is relatively simple to calculate compared to other coefficients.

L_{cv} account for the charge flow carried by the Poiseuille flow. In the infinite half-space geometry where the solid surface is located in $z = 0$, L_{cv} is given by,

$$L_{cv} = \int_0^h \rho(z) \frac{z(h-z)}{2} dz, \quad (7.84)$$

the code used to calculate L_{cv} is given in the figure below,

```

Clear[γ, λ, h, np, nm];
|efface
Element[{γ, λ, nθ, h}, Reals];
|élément |nombres réels
np[z_] := nθ  $\left(\frac{(1 + \gamma * \text{Exp}[-z / \lambda])}{(1 - \gamma * \text{Exp}[-z / \lambda])}\right)^2$ ; (* counter-ions density*)
nm[z_] := nθ  $\left(\frac{(1 - \gamma * \text{Exp}[-z / \lambda])}{(1 + \gamma * \text{Exp}[-z / \lambda])}\right)^2$ ; (* co-ions density*)

ρ[z_] := np[z] - nm[z]; (* charge density*)

lcv[h_] := Integrate[ρ[z] * z * (h - z), {z, 0, h}];
|intègre
Print[" lcv = ", lcv[h]];
|imprime

```

Figure 7.2: Screen shot of the code used to calculate the coefficient L_{cv} .

This code yields the result,

$$\begin{aligned}
L_{cv} &= 8n_0\lambda^2 \left[h \left(\operatorname{arccoth}(\gamma) + \operatorname{arccoth}(\gamma e^{-h/\lambda}) \right) \right. \\
&= \left. + \lambda \left(\operatorname{Li}_2\left(\frac{-1}{\gamma}\right) + \operatorname{Li}_2\left(\frac{1}{\gamma}\right) + \operatorname{Li}_2\left(\frac{-e^{h/\lambda}}{\gamma}\right) - \operatorname{Li}_2\left(\frac{e^{h/\lambda}}{\gamma}\right) \right) \right],
\end{aligned} \tag{7.85}$$

considering that for large separations $e^{-h/\lambda} \rightarrow 0$ and using the relation,

$$\operatorname{arccoth}(\gamma) = \operatorname{arcth}(\gamma) + i\pi, \tag{7.86}$$

One gets the analytic expression of L_{cv} in the case of wide channel approximation. Using the relation $\phi_0 = -4\operatorname{arcth}(\gamma)$ and taking just the real part of (7.85),

$$L_{cv} = \frac{-h\phi_0}{4\pi l_B}. \tag{7.87}$$

The calculation of the coefficients L_{cc} is more complicated compared to L_{cv} . We define the electric conductivity L_{cc} in the infinite half-space geometry as,

$$L_{cc} = \int_0^h \left(\rho(z)f(z) + \mu n(z) \right) dz, \tag{7.88}$$

with the electrophoretic mobility $f(z)$ given by,

$$f(z) = \int_0^z dz' \int_{z'}^{h/2} dz'', \tag{7.89}$$

the second term in (7.88) is very simple to derive $\int n dz = 2n_0 h + 2\sigma$, whereas the first term is more delicate. We can calculate it using the code,

```

Clear[λ, γ, h, np, nm];
|efface
Element[{λ, γ, h, n0}, Reals]
|élément |nombres réels
np[z_] := n0 ((1 + γ * Exp[-z / λ])^2 / (1 - γ * Exp[-z / λ]));
nm[z_] := n0 ((1 - γ * Exp[-z / λ])^2 / (1 + γ * Exp[-z / λ]));
c[z_] := np[z] - nm[z];
I1[h_, zp_] := Integrate[c[zpp], {zpp, zp, h/2}];
|intégrè
I2[h_, z_] := Integrate[I1[h, zp], {zp, 0, z}];
|intégrè
Lcc[h_] := Integrate[(c[z] * I2[h, z]), {z, 0, h}];
|intégrè
Lcc[h]

```

Figure 7.3: Screen shot of the code used to calculate the first term of the electric conductivity L_{cc} .

This code yields,

$$\begin{aligned}
L_{cc} := & 32 n_0^2 \gamma (e^{h/\lambda} + \gamma^2) \lambda^3 \\
& \left(\frac{2(-1 + e^{h/\lambda}) \operatorname{ArcCoth}\left[e^{-\frac{h}{\lambda}} \gamma\right]}{\left(e^{\frac{2h}{\lambda}} - \gamma^2\right)(-1 + \gamma^2)} + \frac{2(-1 + e^{h/\lambda}) \operatorname{ArcTanh}[\gamma]}{\left(e^{\frac{2h}{\lambda}} - \gamma^2\right)(-1 + \gamma^2)} - \frac{\gamma + 2 e^{h/\lambda} \operatorname{ArcCoth}[\gamma] + 2 e^{h/\lambda} \operatorname{ArcTanh}\left[e^{-\frac{h}{\lambda}} \gamma\right]}{\left(e^{\frac{2h}{\lambda}} - \gamma^2\right)(e^{h/\lambda} + \gamma^2)} - \right. \\
& \frac{1 + 2 \gamma \operatorname{ArcCoth}[\gamma] + 2 \gamma \operatorname{ArcTanh}\left[e^{-\frac{h}{\lambda}} \gamma\right]}{\gamma(-1 + \gamma^2)(e^{h/\lambda} + \gamma^2)} - \frac{2 e^{h/\lambda} \gamma \operatorname{Log}\left[e^{\frac{2h}{\lambda}} - \gamma^2\right]}{(e^{h/\lambda} - \gamma^2)(e^{h/\lambda} + \gamma^2)^2} + \\
& \frac{e^{\frac{4h}{\lambda}} - 2 e^{\frac{4h}{\lambda}} \gamma^2 + 2 e^{\frac{2h}{\lambda}} \gamma^6 - \gamma^8 + 2 e^{h/\lambda} \gamma^2 \left(e^{\frac{2h}{\lambda}} - \gamma^2\right)(-1 + \gamma^2) \operatorname{Log}[1 - \gamma^2] - 2 e^{h/\lambda} \gamma^2 \left(e^{\frac{2h}{\lambda}} - \gamma^2\right)(-1 + \gamma^2) \operatorname{Log}\left[e^{\frac{2h}{\lambda}} - \gamma^2\right]}{\gamma(-1 + \gamma^2)(-e^{h/\lambda} + \gamma^2)(e^{h/\lambda} + \gamma^2)^2 \left(-e^{\frac{2h}{\lambda}} + \gamma^2\right)} + \\
& \left. \frac{2 e^{h/\lambda} \gamma \operatorname{Log}\left[-e^{-\frac{2h}{\lambda}}(-1 + \gamma^2)\right]}{(e^{h/\lambda} - \gamma^2)(e^{h/\lambda} + \gamma^2)^2} \right);
\end{aligned}$$

Figure 7.4: Analytic expression of the first term in L_{cc} calculated in WCA.

To simplify this expression we proceed as follows,

- we get rid of the terms proportional to $e^{-h/\lambda}$ since $h \gg \lambda$ in the WCA.
- we further simplify the new expression by rearranging the terms to have a very simple analytical expression given by,

$$L_{cc} = \frac{\sinh\left(\frac{\phi_0}{4}\right)^2}{\lambda \pi^2 l_B^2} + \frac{n_0 h + \sigma}{3 \pi a}. \quad (7.90)$$

For the coefficients calculated in the chapter salt-charge-flow coupling coefficients. We used the same approach and we can give as an example of coefficient involving the salt

density the coefficients L_{sv} given by,

$$L_{sv} = \int_0^h n(z) \frac{z(h-z)}{2} dz, \quad (7.91)$$

the code used to calculate L_{sv} is given in the figure below,

```

Clear[ $\gamma$ ,  $\lambda$ , h, np, nm];
|efface
Element [{ $\gamma$ ,  $\lambda$ , n0, h}, Reals];
|élément |nombres réels
np[z_] := n0  $\left( \frac{(1 + \gamma * \text{Exp}[-z / \lambda])}{(1 - \gamma * \text{Exp}[-z / \lambda])} \right)^2$ ; (* counter-ions density*)
nm[z_] := n0  $\left( \frac{(1 - \gamma * \text{Exp}[-z / \lambda])}{(1 + \gamma * \text{Exp}[-z / \lambda])} \right)^2$ ; (* co-ions density*)

nn[z_] := np[z] + nm[z] - 2 n0; (* salt density*)

lsv[h_] := Integrate[nn[z] * z (z - h), {z, 0, h)];
|intègre

```

Figure 7.5: Screen shot of the code used to calculate L_{sv} in the WCA.

This code yields,

$$L_{sv} = 4n_0\lambda^2 \left[-h \left(\ln\left(1 - \frac{1}{\gamma^2}\right) + \ln\left(1 - \frac{e^{h/2\lambda}}{\gamma^2}\right) \right) + \lambda \left(Li_2\left(\frac{1}{\gamma^2}\right) + Li_2\left(\frac{e^{h/2\lambda}}{\gamma^2}\right) \right) \right], \quad (7.92)$$

taking into account the real and imaginary parts of the polylog functions Li_2 , the dependencies in h^2 are simplified. Thus we find after rearrangements of the terms,

$$L_{sv} = \frac{h}{\lambda l_B} \ln \left(\cosh\left(\frac{\phi_0}{4}\right) \right). \quad (7.93)$$

7.10 Numerical evaluations

For the sake of simplicity we choose the symmetric geometry where the immobile surface at position $z = -h/2$, and the lower sphere surface at $z = h/2$. This choice is very convenient to exploit the symmetric proprieties of the system, and set up the right boundary conditions in order to determine Jacobi's function parameter k .

To determine the parameter k we can use the boundary conditions (CC), (CP) or (CR) depending on the results seeking for. To give an example let's consider the constant charge boundary condition given by the equation (2.21) in the symmetric case, where the electric field is proportional to the surface charge density σ at $z = h/2$,

$$\frac{\sigma}{\varepsilon} = \frac{1}{\beta q} \phi'\left(\frac{h}{2}, k\right), \quad (7.94)$$

performing the derivation of the electrostatic potential with respect to z , yields the electric field linked to the surface charge density by the simple relation,

$$S = \frac{k^2 - 1}{\sqrt{k}} \frac{nd(\frac{h}{2}, k) sd(\frac{h}{2}, k)}{cd(\frac{h}{2}, k)} \quad (7.95)$$

The right hand of this equation depend on the channel height, while the left hand quantity is given by $S = \sigma\lambda q/k_B T\epsilon$, which depends on the surface charge density and the diffuse layer thickness, thus we can reexpress S as,

$$S = \frac{2\lambda}{b} \quad (7.96)$$

$$= 4\pi l_B \sigma \lambda, \quad (7.97)$$

Using the code that we developed,

```

Clear[ψ, λ, cd, sn, sd, cn, nc, nd];
|efface
(* Jacobi's functions *)
cd[z_, k_] := JacobiCD[ $\frac{z}{2\lambda\sqrt{k}}$ , k^2]; sd[z_, k_] := JacobiSD[ $\frac{z}{2\lambda\sqrt{k}}$ , k^2]; nd[z_, k_] := JacobiND[ $\frac{z}{2\lambda\sqrt{k}}$ , k^2];
|nd de Jacobi |sd de Jacobi |nd de Jacobi
(* Potential with parameter k *)
ψ[z_, k_] := Log[k] + 2 Log[cd[z, k]];
|logarithme |logarithme
(* S expression *)
s := -4 π σ lB λ;
γ :=  $\frac{2}{s} + \sqrt{\frac{4}{s^2} + 1}$ ;
ξ := 4 * ArcTanh[γ];
|arc tangente hyperbolique
(* the parameters values *)
n = 5; λ = 30; σ = 0.01; lB = 0.7; dd = 0.01 * λ; hmin = 0.01 * λ; k0 = 0.01;
n0 =  $\frac{1}{8\pi lB \lambda^2}$ ;
(*****)
Do[hh = hmin + dd * i; (* channel height*)
|boucle do
f :=  $\frac{k^2 - 1}{\sqrt{k}} \frac{nd[\frac{hh}{2}, k] \times sd[\frac{hh}{2}, k]}{cd[\frac{hh}{2}, k]}$ ; (* Implicit eq for k as a function of s *)
a := FindRoot[{f == s}, {k, k0}];
|trouve racine
Rk := Evaluate[Re[k] /. a];
|évalue |partie réelle
k0 = Rk; (* the parameters values *)
, {i, 0, n}];

```

Figure 7.6: Screen shot of the code used to calculate the parameter k .

We can get the value of k by choosing some experimental values for λ , σ , h and evaluate numerically the implicit equation (7.95). To find the root of it which represent the parameter k , this latter equals 0 for $h = 0$ and 1 for $h \rightarrow \infty$ see figure (2.3).

Once we have determined the values of k for the different values of h , we can evaluate Onsager coefficients numerically and compare them with the analytic results.

The figure below shows a comparison, between the analytic and the numeric evaluations of Onsager's coefficients L_{cc} and L_{ss} .

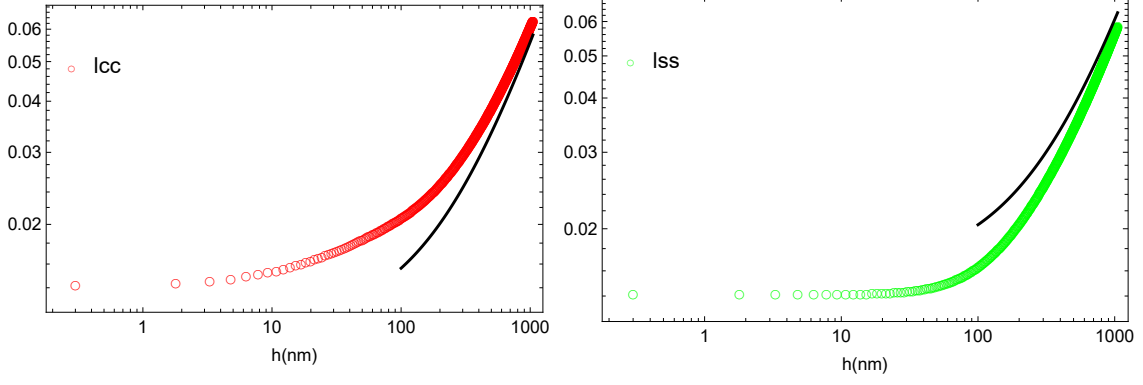


Figure 7.7: L_{cc} and L_{ss} variations as a function of h on a logarithmic scale. The black solid line refers to the analytic expressions calculated in the case of WCA, whereas the open circles refers to the numerical evaluations using the potential (2.16). The calculations are performed using the (CC) boundary condition with $\sigma = 0.02\text{nm}^{-2}$

From this figures we can see good agreement between the analytic expressions, and the numerical evaluations of the coefficients L_{cc} and L_{ss} , this agreement is valid also for all the other coefficients.

7.11 Electrostatic repulsion between two solid surfaces

Let's consider two solid surfaces similarly charged and brought sufficiently close to each other. The surfaces are located at position $z = \pm h/2$, the energy of the counterions cloud in the gap between the two surfaces can be described, in term of their free energy which consist of the electrostatic energy (the electrostatic interactions between the ions) and the entropy of the ions in the medium, which tends to maximizes their configurations in order to reach the system stability. We can express the free energy [21,31] as,

$$\begin{aligned}\mathbb{F} &= U - TS \\ &= A \int \Omega dz.\end{aligned}\tag{7.98}$$

Performing the integration of energy density Ω , over a volume element is equivalent to perform the integration with respect to z times a given area A , where Ω is given by,

$$\Omega = \frac{\epsilon}{8\pi}(\nabla\phi)^2 + k_B T \left(n_+ \ln \frac{n_+}{n_0} + n_- \ln \frac{n_-}{n_0} - (n_+ + n_- - 2n_0) \right).\tag{7.99}$$

The osmotic pressure can be derived from the variations of \mathbb{F}/A with respect to the separation distance between the surfaces h .

$$\Pi = -A \frac{d\mathbb{F}}{dh},\tag{7.100}$$

note that the temperature and the chemical potential are considered to be constant, since we have two similarly charged surfaces. The electric field at midplane is zero, thus the derivation above yields the expression of the pressure between the surfaces which is given simply by the excess osmotic pressure as,

$$\Pi = k_B T (n_m - 2n_0),\tag{7.101}$$

where n_m is the salt density at midplane and n_0 is the bulk density at the equilibrium state.

7.12 Charge current relaxation time

In this section we give an approximation of the relaxation time of the charge current, using the continuity equation,

$$\partial_t C = \nabla \cdot J_c \quad (7.102)$$

we discard the diffusion term amusing that the diffusion time in the radial direction (2.28) of the channel is much longer then the charge relaxation time. We couple the above equation to Gauss law given by,

$$\nabla \cdot E = \frac{\rho}{\epsilon}, \quad (7.103)$$

integrating (7.103) over the channel height one get,

$$h \nabla \cdot E = \frac{C}{\epsilon}, \quad (7.104)$$

Inserting (7.104) in (7.102) one get,

$$\nabla \cdot \partial_t E = \frac{1}{h\epsilon} \nabla \cdot J_c, \quad (7.105)$$

since the variations of the channel height are very small (linear response-regime) are very small compared to the minimum value h_0 . We can consider that the coefficients are constant, thus we write,

$$\partial_t E = \frac{1}{h_0\epsilon} (L_{cv} \nabla P - L_{cc} e E), \quad (7.106)$$

using Fourier transformation the time derivative $\partial_t E$ reads as $i\omega E$. Inserting this latter expression in (7.106) one get,

$$\frac{e\tilde{E}}{\eta} = \frac{L_{cv}}{L_{cc}} \frac{\nabla\tilde{P}}{\eta} \frac{1}{1 + i\omega\tau} \quad (7.107)$$

with the relaxation time,

$$\frac{1}{\tau} = \frac{e^2 L_{cc}}{h_0 \epsilon \eta}, \quad (7.108)$$

using the term in L_{cc} (the dominant term) one gets,

$$\frac{1}{\tau} = \frac{k_B T}{6\pi\alpha\eta\lambda^2}, \quad (7.109)$$

for an equivalent hydrodynamic radius $\alpha = 0.15\text{nm}$, $\lambda = 30\text{nm}$ and a dynamic viscosity of water at an ambient temperature one get $\tau \sim 2.6 \times 10^{-7}\text{s}$. Which is very small compared to the sphere vibrations time $\omega_0^{-1} \sim 10^{-2}\text{s}$, as well as the diffusion time given by (2.28), which validate our assumption.

Fore more details on the charge currents relaxation time see Marcela Rodriguez Matus thesis.

7.13 Salt-charge-flow coupling parameter ξ

The expressions of the salt-charge-flow coupling parameter in the WCA as well as NCA, are given by,

$$\xi_{WCA} = \frac{3 \left(\xi^2 \left(\frac{h n \theta + \sigma}{3 \pi \alpha} + 64 n \theta^2 \lambda^3 \left(-\frac{\gamma^2}{-1 + \gamma^2} + \text{Log}[1 - \gamma^2] \right) \right) - 8 \xi \left(\frac{\sigma}{3 \pi \alpha} - 64 n \theta^2 \lambda^3 \left(\frac{\gamma}{-1 + \gamma^2} + \text{ArcTanh}[\gamma] \right) \right) \text{Log} \left[\text{Cosh} \left[\frac{\xi}{4} \right] \right] + \frac{16 \text{Log} \left[\text{Cosh} \left[\frac{\xi}{4} \right] \right]^2 \left(\frac{\pi (h n \theta + \sigma)}{\alpha} + \frac{3 \text{Sinh} \left[\frac{\xi}{4} \right]^2}{16^2 \lambda} \right)}{3 \pi^2} \right)}{4 h 16^2 \pi^2 \left(-\left(\frac{\sigma}{3 \pi \alpha} - 64 n \theta^2 \lambda^3 \left(\frac{\gamma}{-1 + \gamma^2} + \text{ArcTanh}[\gamma] \right) \right)^2 + \frac{\left(\frac{h n \theta + \sigma}{3 \pi \alpha} + 64 n \theta^2 \lambda^3 \left(-\frac{\gamma^2}{-1 + \gamma^2} + \text{Log}[1 - \gamma^2] \right) \right) \left(\frac{\pi (h n \theta + \sigma)}{\alpha} + \frac{3 \text{Sinh} \left[\frac{\xi}{4} \right]^2}{16^2 \lambda} \right)}{3 \pi^2} \right)}$$

$$\xi_{NCA} = \frac{\pi \alpha \left(4 h^2 \pi \alpha \sigma^6 + 33 600 n \theta^3 \lambda^4 \sigma^2 \sqrt{1 + \frac{\sigma^2}{h^2 n \theta^2}} + 21 n \theta \sigma^4 \left(-80 \lambda^2 + h^2 \sqrt{1 + \frac{\sigma^2}{h^2 n \theta^2}} \right) \right)}{33 600 n \theta^4 \lambda^4 + 4 h^2 \pi^2 \alpha^2 \sigma^6 + 33 600 n \theta^3 \pi \alpha \lambda^4 \sigma^2 \sqrt{1 + \frac{\sigma^2}{h^2 n \theta^2}} + 5 n \theta \pi \alpha \sigma^4 \left(-336 \lambda^2 + 5 h^2 \sqrt{1 + \frac{\sigma^2}{h^2 n \theta^2}} \right)}$$

With σ the surface charge density, α the equivalent hydrodynamic radius, and $\zeta \equiv \phi_0$ the electrostatic potential at the solid surfaces.

7.14 Debye Hückel approximation

The approximation of Debye Hückel is applicable in the case of monovalent counterions,¹ where the electrostatic potential is very weak. In this case we can develop the second term of (2.6) ($\sinh \phi$) as Taylor's series [21, 31],

$$\sinh \phi(z) \simeq \phi(z), \quad (7.110)$$

thus the resolution of (2.6) yields the potential $\phi(z)$ given by,

$$\phi(z) = C e^{-\frac{z}{\lambda}}, \quad (7.111)$$

the constant of integration C is determined using (CC) boundary condition,

$$\phi'(0) = \frac{-\sigma}{\varepsilon} \quad (7.112)$$

where σ is the surface charge density, therefore we get,

$$\phi(z) = \frac{2\lambda}{b} e^{-\frac{z}{\lambda}}, \quad (7.113)$$

where b is the Gouy Chapman length,

$$b = \frac{e}{2\pi l_B \sigma}, \quad (7.114)$$

the counter and coions expressions, can be derived using Boltzmann distribution,

$$n_{\pm}(z) \simeq n_0 (1 \pm \pi l_B \sigma \lambda e^{-\frac{z}{\lambda}}). \quad (7.115)$$

The integration of the charge density ρ in Debye Hückel approximation yields,




$$C = 2\sigma \quad (7.116)$$

And the radial salinity as,

$$N = 2n_0 h \quad (7.117)$$

¹This approximation is not suitable for divalent and trivalent counterions [113, 114].

Electroviscous drag on squeezing motion in sphere-plane geometry

Marcela Rodríguez Matus ^{1,*}, Zaicheng Zhang ^{1,*}, Zouhir Benrahla^{1,*}, Arghya Majee ²,
Abdelhamid Maali ^{1,†} and Alois Würger ^{1,‡}

¹Université de Bordeaux & CNRS, Laboratoire Ondes et Matière d'Aquitaine, 33405 Talence, France

²Max Planck Institute for Intelligent Systems, 70569 Stuttgart, Germany

and IV. Institute for Theoretical Physics, University of Stuttgart, 70569 Stuttgart, Germany



(Received 13 December 2021; accepted 27 May 2022; published 16 June 2022)

Theoretically and experimentally, we study electroviscous phenomena resulting from charge-flow coupling in a nanoscale capillary. Our theoretical approach relies on Poisson-Boltzmann mean-field theory and on coupled linear relations for charge and hydrodynamic flows, including electro-osmosis and charge advection. With respect to the unperturbed Poiseuille flow, we define an electroviscous coupling parameter ξ , which turns out to be maximum where the film height h_0 is comparable to the Debye screening length λ . We also present dynamic atomic force microscopy data for the viscoelastic response of a confined water film in sphere-plane geometry; our theory provides a quantitative description for the electroviscous drag coefficient and the electrostatic repulsion as a function of the film height, with the surface charge density as the only free parameter. Charge regulation sets in at even smaller distances.

DOI: [10.1103/PhysRevE.105.064606](https://doi.org/10.1103/PhysRevE.105.064606)

I. INTRODUCTION

Solid surfaces in contact with water are mostly charged, resulting in intricate interactions of the diffuse layer of counterions with liquid flow along the solid boundary [1–3]. Charge-flow coupling is at the origin of various electrokinetic and electric-viscous effects [4]. Besides classical applications of capillary electrophoresis ranging from microfluidics to medical analysis, recently ac charge-induced electro-osmosis has been used for the assembly of active materials. From micron-size colloidal building blocks [5], surface osmotic effects have been discussed in view of energy applications and desalination of sea water [6].

The underlying physical mechanisms operate on the scale of the Debye screening length [7], which is of the order of a few tens of nanometers. Following the derivation of the electro-osmotic coefficient by Helmholtz [8] and Smoluchowski [9], electrokinetic effects have been extensively studied in the limit of thin double layers, where the screening length is much smaller than the depth of the liquid phase. Thus Bikerman and Dukhin [10] derived the surface contribution to the electric conductivity of a salt solution, and Hückel [11] and Henry [12] showed the colloidal electrophoretic mobility to depend on the ratio of particle size and screening length. Gross and Osterle studied charged membranes separating two electrolyte solutions at different pressure and electrochemical potentials, and numerically calculated the transport coefficients of nanopores comparable to the screening length [13].

Prieve and collaborators studied charge effects on the motion of a colloidal sphere moving close to a solid surface [14–18]. For a particle sliding parallel to the surface at velocity V , they observed a normal lift force proportional to V^2 . This dependence suggests as an underlying mechanism the Maxwell stress ϵE^2 , with permittivity ϵ and the parallel electric field arising from the streaming potential, $E \propto V$ [15]. Yet the measured lift force [17] by far exceeds the calculated value [18]; this discrepancy has not been elucidated so far.

Quite a different situation occurs for the squeezing motion of a colloidal sphere vibrating in normal direction with a sinusoidal displacement $Z(t)$, as shown schematically in Fig. 1. The velocity $V = dZ/dt$ is by orders of magnitude smaller than that of sliding motion, resulting in a negligibly weak electrokinetic lift. For uncharged surfaces, the only force at work is the hydrodynamic drag $-\gamma_0 V$ with coefficient γ_0 . The presence of electric double layers gives rise to several electrokinetic forces,

$$K - kZ - \gamma V, \quad (1)$$

where the electrostatic repulsion K is well known from static atomic force microscopy (AFM) experiments [19]. For a mechanically driven system as in Fig. 1, the dynamic response consists of a restoring force $-kZ$ with an effective spring constant k and an enhanced drag coefficient γ , due to the coupling of the charged diffuse layers to the radial flow profile [20,21]. Bike and Prieve calculated the charge contribution $\gamma - \gamma_0$ for the case where the sphere-plane distance h_0 is much larger than the Debye screening length λ [15]. Subsequent numerical studies discussed the enhancement factor for both narrow and wide channels, and found a maximum to occur at $\lambda/h_0 \approx 1$ [22,23]. The first unambiguous experimental observation of the electroviscous effect was reported very recently by Liu *et al.*, who performed dynamic AFM experiments in weak electrolyte solutions [21].

*M.R.M., Z.Z., and Z.B. contributed equally to this work.

†abdelhamid.maali@u-bordeaux.fr

‡alois.wurger@u-bordeaux.fr

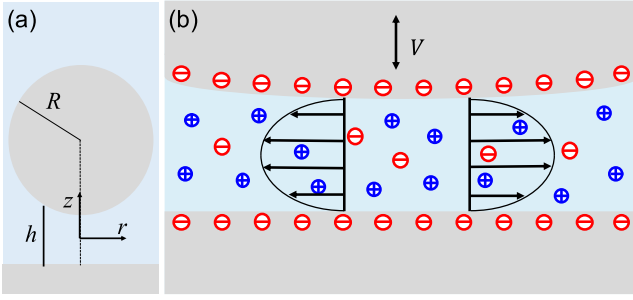


FIG. 1. Schematic view of charge-flow coupling in sphere-plane geometry. (a) A colloidal sphere of radius R is placed above a solid surface. The film height h varies with the radial coordinate r and takes its minimum value h_0 at $r = 0$; this distance satisfies $h_0 \ll R$. (b) The sphere vertically vibrates with velocity $V(t)$. This squeezing motion induces a radial Poiseuille flow in the confined water film containing mobile ions of either sign.

The present work intends to clarify whether charge-flow coupling accounts quantitatively for the electroviscous drag on the squeezing motion illustrated in Fig. 1. Section II provides a brief reminder of Poisson-Boltzmann theory, and the static repulsive force K and the spring constant k . In Sec. III we develop the formal apparatus for charge-flow coupling, relying on Onsager's phenomenological relations for generalized fluxes and forces, without resorting to the linearization approximation in the electroviscous coupling parameter. We derive the electroviscous drag coefficient γ in terms of the Onsager transport coefficients L_{ij} . In Sec. IV we compare analytical approximations for the limiting cases of narrow and wide channels with the numerical computation. Section V is devoted to a discussion of the effect of charge regulation on both electrostatic and electroviscous properties. In Sec. VI we present dynamic-AFM measurements and compare with our theoretical findings.

II. ELECTROSTATICS

Here we briefly discussed the electrostatic properties in the absence of external driving. Solid materials in contact with water in general carry surface charges. Due to electrostatic screening, the released counterions are confined in a diffuse layer of charge density ρ , which is related to the electrostatic potential ψ through Gauss's law:

$$\nabla^2 \psi = -\frac{\rho}{\epsilon}. \quad (2)$$

In the framework of Poisson-Boltzmann mean-field theory, the concentrations of monovalent ions read $n_{\pm} = n_0 e^{\mp e\psi/k_B T}$, where the bulk value n_0 corresponds to dissolved salt, to carbonic acid absorbed from air, or to the dissociation of water. The resulting expression for the charge density,

$$\rho = e(n_+ - n_-) = 2en_0 \sinh \frac{e\psi}{k_B T}, \quad (3)$$

then closes Gauss's law.

A. 1D Poisson-Boltzmann theory

This work deals with thin films as in Fig. 1, where the minimum height is much smaller than the radius of the vibrating sphere, $h_0 \ll R$. Then electrostatic and hydrodynamic properties are relevant in the lubrication area only, which corresponds to the range where the radial coordinate r takes values much smaller than R and where the height $h(r)$ of the aqueous film is a slowly varying function of r . For notational convenience we define the origin of the vertical coordinate z such that the solid boundaries are at $z = \pm h/2$.

Throughout this paper we assume a homogeneous surface charge and use the 1D Poisson-Boltzmann equation where ψ and ρ depend on the vertical coordinate z only,

$$\frac{e}{k_B T} \frac{d^2 \psi}{dz^2} = \lambda^{-2} \sinh \frac{e\psi}{k_B T}. \quad (4)$$

Here we introduce two characteristic length scales: the Debye screening length

$$\lambda = \frac{1}{\sqrt{8\pi n_0 \ell_B}}, \quad (5)$$

which gives the thickness of the diffuse layer in an electrolyte solution [24], and the Bjerrum length

$$\ell_B = \frac{e^2}{4\pi \epsilon k_B T}, \quad (6)$$

which gives the distance where the electrostatic interaction of two elementary charges is equal to the thermal energy. Typical values in water are $\lambda = 1 \dots 300$ nm and $\ell_B = 0.7$ nm.

For fixed surface charge density $-\epsilon\sigma$, the potential satisfies the boundary condition

$$\frac{e\sigma}{\epsilon} = \mp \frac{d\psi}{dz} \Big|_{z=\pm h/2}. \quad (7)$$

For fixed surface potential one has $\psi(\pm h/2) = \zeta$. Note that the potential $\psi(z)$ and its surface value ζ depend on the film height h and thus on r .

B. Disjoining pressure and repulsive force

For the sake of notational simplicity we assume a symmetric system with the same charge density σ on the two opposite surfaces. Then the disjoining pressure is given by the excess osmotic pressure of the mobile ions at $z = 0$, which reads $\Pi = (n_m - 2n_0)k_B T$. With the excess number density $n_m = 2n_0 \cosh[\psi(0)/k_B T]$, one readily finds

$$\Pi = 2n_0 k_B T \left(\cosh \frac{e\psi(0)}{k_B T} - 1 \right). \quad (8)$$

The dependence of the osmotic pressure on the film height h arises from the potential $\psi(z = 0)$ [24]. At distances h larger than the screening length λ , this potential vanishes, and so does the disjoining pressure.

The repulsive force K between the two surfaces is obtained as the surface integral the osmotic pressure. The film height being much smaller than the curvature radius, we use the Derjaguin approximation [25]. For distances much smaller than the radius of the oscillating sphere, the height of the water

film $h = h_0 + R - \sqrt{R^2 - r^2}$ is well approximated by

$$h(r) = h_0 + \frac{r^2}{2R}, \quad (r \ll R). \quad (9)$$

Writing the surface element as $dS = 2\pi r dr = 2\pi R dh$, one readily obtains

$$K(h_0) = \int dS \Pi = 2\pi R \int_{h_0}^{\infty} dh \Pi(h). \quad (10)$$

The disjoining pressure gives rise to a static restoring force $-kZ$, with spring constant

$$k(h_0) = -\frac{dK}{dh_0} = 2\pi R \Pi(h_0). \quad (11)$$

The discussion and numerical evaluation of the force K and the rigidity k are postponed to Sec. V below.

III. CHARGE-FLOW COUPLING: FORMAL APPARATUS

Here we derive the formal expression for the electroviscous drag coefficient γ defined in (1). Resorting to lubrication approximation, we give the coupled hydrodynamic and charge flows in radial direction, which are imposed by the mechanical driving, as illustrated in Fig. 1. Then we derive expressions for the hydrodynamic pressure and the resulting drag force.

We consider charged surfaces in sphere-plane geometry in contact with an electrolyte solution, as shown schematically in Fig. 1. The vertical distance varies with time according to $h_0 + Z(t)$, with a small sinusoidal amplitude $|Z| \ll h_0$ and frequency ω , resulting in the velocity $V = dZ/dt$. Experimentally, this is realized by a vibrating sphere of radius R mounted on the cantilever of an atomic force microscope.

A. Lubrication approximation

The vertical oscillation modulates the hydrodynamic pressure P in the film and imposes a flow J_V . For an incompressible fluid, there is a simple geometrical relation between the vertical velocity V of the cantilever and the volume flow carried by the radial fluid velocity v ,

$$\pi r^2 V = 2\pi r J_V = 2\pi r \int_{-h/2}^{h/2} dz v(z, r). \quad (12)$$

Note that the height $h(r)$ varies with the radial position r according to (9).

The fluid mechanical problem simplifies significantly when resorting to the lubrication approximation [26]. In the range of validity of Eq. (9), the vertical component of the velocity field is negligible, and the radial component v obeys a simplified Stokes equation,

$$\eta \partial_z^2 v = \partial_r P - \rho E, \quad (13)$$

with the viscosity η and where only the vertical component of the Laplace operator $\nabla^2 v$ has been retained. The right-hand side comprises the radial pressure gradient $\partial_r P$ and the force exerted by a radial electric field E and the charge density ρ of the diffuse layer.

B. Nonequilibrium fluxes and forces

Using the Derjaguin approximation, the electrostatic properties can be calculated from the one-dimensional (1D) Poisson-Boltzmann equation (4) with slowly varying gap height $h(r)$. Yet this equilibrium state is perturbed by charge-flow coupling. Indeed, advection of counterions by the radial velocity v results in a radial charge distribution and an electric field E . Through the electro-osmotic force ρE in (13), the field backreacts on the flow properties.

For an axisymmetric geometry, both E and the pressure P depend on the radial coordinate r only, and the velocity field $v = v_P + v_E$ and charge current $j = j_P + j_E$ point in radial direction. Integrating over the vertical variable z we obtain the fluxes of volume and charge,

$$J_V = \int_{-h/2}^{h/2} dz (v_P + v_E) \equiv -L_{vv} \nabla P + L_{vc} E, \quad (14)$$

$$J_C = \int_{-h/2}^{h/2} dz (j_P + j_E) \equiv -L_{cv} \nabla P + L_{cc} E, \quad (15)$$

where the second identity defines the linear transport coefficients L_{ij} with respect to the generalized forces $-\nabla P = -dP/dr$ and eE .

The first term in Eq. (14) arises from the pressure-driven flow profile $v_P(z)$. Assuming no-slip boundary conditions $v_P(\pm h/2) = 0$, the Stokes equation (13) with $E = 0$ is readily integrated,

$$v_P = -\frac{h^2 - 4z^2}{8\eta} \nabla P, \quad (16)$$

resulting in

$$L_{vv} = \frac{h^3}{12\eta}. \quad (17)$$

The second term in (14) accounts for the electro-osmotic velocity profile [27]

$$\begin{aligned} v_E(z) &= -\frac{1}{\eta} \int_z^{h/2} dz' \int_0^{z'} dz'' \rho(z'') E \\ &= \frac{\varepsilon}{\eta} [\psi(z) - \zeta] E, \end{aligned} \quad (18)$$

where the second identity follows from twice integrating Gauss' law $\varepsilon \partial_z^2 \psi = -\rho$. This leads to the electro-osmotic transport coefficient

$$L_{vc} = \frac{1}{E} \int_{-h/2}^{h/2} dz v_E(z). \quad (19)$$

The electric current (15) consists of advection of counterions in the Poiseuille flow profile v_P ,

$$L_{cv} = \frac{1}{\eta} \int_{-h/2}^{h/2} dz \rho(z) \frac{h^2 - 4z^2}{8}, \quad (20)$$

and Ohm's law with the conductivity L_{cc} . This latter coefficient reads as

$$L_{cc} = \int_{-h/2}^{h/2} dz \left(\rho \frac{\varepsilon}{\eta} (\psi - \zeta) + e^2 (\mu_+ n_+ + \mu_- n_-) \right), \quad (21)$$

where the first term accounts for advection by the electro-osmotic velocity field v_E and the second one for electrophoresis of salt ions, with mobilities μ_{\pm} .

Electrokinetic phenomena in a channel between two electrolyte reservoirs at different electrochemical potential are characterized by a constant streaming current $J_C \neq 0$ [6,13,14]. Contrary to this open geometry, the periodically driven squeezing motion of Fig. 1 does not allow for a steady current but gives rise to the electric field E . Strictly speaking, there is a small current which develops the space charges related to the electric field, $\delta\rho = \varepsilon \operatorname{div} E$, and which vanishes when averaged over one cycle. Because of the strong electric interactions, the space charges develop almost instantaneously such that the electric field is in phase with the pressure gradient, and that advection and conduction currents cancel each other in (15),

$$J_C = 0. \quad (22)$$

This relation holds true as long as the charge relaxation time τ is much shorter than the period of the external driven, $\omega\tau \ll 1$.

C. Drag force

With the above condition of zero charge current, Eq. (15) implies a relation between the radial electric field and the pressure gradient,

$$E = \frac{L_{cv}}{L_{cc}} \nabla P. \quad (23)$$

Inserting this in the volume current (14) and solving for the pressure gradient, we find

$$\nabla P = -\frac{6\eta r V}{h^3} \frac{1}{1 - \xi}, \quad (24)$$

where the coupling of the double layer to the flow is accounted for by the ratio of off-diagonal and diagonal transport coefficients L_{ij} ,

$$\xi = \frac{L_{vc}L_{cv}}{L_{vv}L_{cc}}. \quad (25)$$

From (24) it is clear that the dimensionless parameter ξ describes the effect of charge-flow coupling on the hydrodynamic pressure. For $\xi = 0$ one recovers the well-known expression for the pressure gradient in capillary. The stability of the dynamic equations (14) and (15) requires a positive determinant of the matrix of the transport coefficients L_{ij} , that is, $\det \mathbf{L} > 0$ or $\xi < 1$.

When integrating the excess hydrodynamic pressure in the capillary, it turns out to be convenient to use the variable h instead of r . In the lubrication approximation (9) one has $dh = dr r/R$ and

$$P(h) = 6\eta RV \int_h^\infty \frac{dh'}{h'^3} \frac{1}{1 - \xi(h')}. \quad (26)$$

Finally, the viscous force on the cantilever is given by the surface integral of the pressure. With $dS = 2\pi dr r = 2\pi R dh$ one finds for the drag coefficient

$$F(h_0) = -2\pi R \int_{h_0}^\infty dh P(h). \quad (27)$$

In Eq. (1) we have defined the electroviscous drag coefficient through $F = -\gamma V$; the above relations give

$$\gamma = 12\pi\eta R^2 \int_{h_0}^\infty dh \int_h^\infty \frac{dh'}{h'^3} \frac{1}{1 - \xi(h')}. \quad (28)$$

In the absence of electroviscous coupling, one readily obtains the pressure

$$P_0(h) = \frac{3\eta VR}{h^2}, \quad (\xi = 0), \quad (29)$$

which is maximum at the center of the film and vanishes as $P_0 \propto r^{-4}$ at large radial distance. The corresponding lubrication drag coefficient [28],

$$\gamma_0 = \frac{6\pi\eta R^2}{h_0}, \quad (\xi = 0), \quad (30)$$

is by a factor R/h_0 larger than the Stokes drag coefficient $6\pi\eta RV$ on a sphere of radius R in a bulk liquid.

IV. ELECTROVISCIOUS DRAG COEFFICIENT

As a main formal result of this paper, Eq. (28) expresses the electroviscous drag enhancement in terms of the coupling coefficient ξ which quantifies the charge-flow coupling. Here, we evaluate Eq. (28) both analytically and numerically.

A. Wide-channel approximation $h \gg \lambda$

If the height of the water film is much larger than the Debye length, the electrostatic potential is given by [24]

$$\psi = -\frac{4k_B T}{e} \operatorname{arctanh}(\beta e^{-z/\lambda}), \quad (31)$$

where the parameter

$$\beta = \frac{\sqrt{1 + (2\pi \ell_B \lambda \sigma)^2} - 1}{2\pi \ell_B \lambda \sigma} \quad (32)$$

depends on the Debye length λ and the surface charge density $-\sigma$, with $\sigma > 0$.

In this case there are analytical expressions for the transport coefficients L_{ij} . The off-diagonal terms are given by the Helmholtz-Smoluchowski electrophoretic mobility,

$$L_{vc} = -\frac{h\varepsilon\xi}{e\eta} = -\frac{h\hat{\zeta}}{4\pi\eta l_B}, \quad (33)$$

where in the second identity we define the dimensionless ζ potential in units of the thermal energy $\hat{\zeta} = e\zeta/k_B T$. The electrical conductivity reads

$$L_{cc} = \frac{\sinh(\hat{\zeta}/4)^2}{\pi^2 \eta \lambda \ell_B^2} + \sum_{\pm} \mu_{\pm} n_0 \left(h - \frac{4\beta\lambda}{\beta \mp 1} \right), \quad (34)$$

where the first term accounts for electro-osmotic advection and the second for ion electrophoresis, with surface contributions parameterized by β .

For wide channels, $h \gg \lambda$, the conductivity is dominated by bulk-ion electrophoresis. Discarding the electro-osmotic and surface terms, and using the definition of the screening length (5), results in the coupling parameter

$$\xi = \frac{\lambda_*^2}{2h^2}, \quad (35)$$

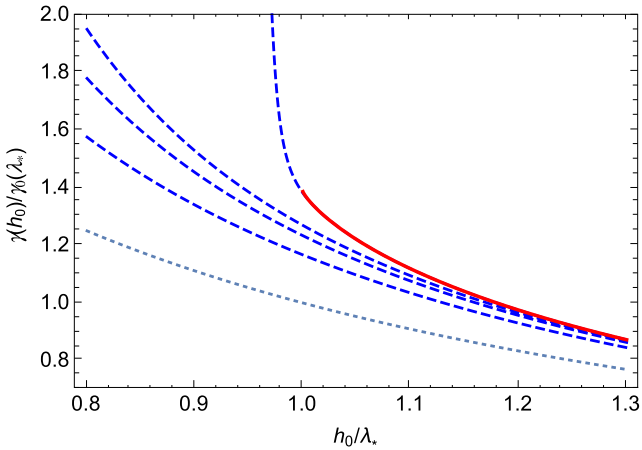


FIG. 2. Electroviscous enhancement of the drag coefficient $\gamma(h_0)$, in units of the purely viscous coefficient γ_0 at $h_0 = \lambda_*$. In the absence of charge-flow coupling as in (30), the dotted line gives $\gamma_0(h_0)/\gamma_0(\lambda_*) = \lambda_*/h_0$. Dashed lines are calculated from the perturbation series (38) for γ , truncated at $(\lambda_*/h_0)^{2n}$ with $n = 1, 2, 3, 100$. The full line represents the complete series (37), which is defined for $h > \lambda_*$ only.

with the length scale

$$\lambda_* = 6\hat{\zeta} \sqrt{\frac{a}{\ell_B}} \lambda. \quad (36)$$

Here and in the following, the mobilities are expressed through ion radii, $\mu_{\pm} = 1/6\pi\eta a_{\pm}$, with the mean value $1/a = 2/a_+ + 2/a_-$.

Then the pressure (26) and the drag coefficient (28) can be integrated in closed form,

$$\frac{\gamma}{\gamma_0} = \frac{h_0}{\lambda_*} \ln \frac{h_0 + \lambda_*}{h_0 - \lambda_*} + \frac{h_0^2}{\lambda_*^2} \ln \frac{h_0^2 - \lambda_*^2}{h_0^2}. \quad (37)$$

In Fig. 2 we plot γ as a (red) solid line. At the distance $h_0 = \lambda_*$ the electroviscous coupling parameter ξ is equal to unity and, as a consequence, a logarithmic branch point appears in the pressure integral (26), resulting in $\gamma/\gamma_0 = 2 \ln 2 \approx 1.39$. At smaller distances the wide-channel approximation for pressure and force integrals is not defined.

It turns out instructive to rewrite (37) as a series in powers of λ_*/h_0 ,

$$\frac{\gamma}{\gamma_0} = 1 + \frac{1}{6} \frac{\lambda_*^2}{h_0^2} + \frac{1}{15} \frac{\lambda_*^4}{h_0^4} + \frac{1}{28} \frac{\lambda_*^6}{h_0^6} + \dots \quad (38)$$

In Fig. 2 we plot this series truncated at $(\lambda_*/h_0)^{2n}$ with $n = 1, 2, 3, 100$ and compare both with (37) and with the uncoupled lubrication drag coefficient (30). Retaining a few terms only suggests a smooth behavior, whereas Eq. (37) is defined for $h_0 \geq \lambda_*$ only. The first correction term, proportional to λ_*^2/h_0^2 , corresponds to the electroviscous coefficient of Bike and Prieve [15].

Noting that the ion radius is usually smaller than the Bjerrum length $\ell_B = 0.7$ nm and $\hat{\zeta}$ of the order of unity, one finds that λ_*/λ takes values between 1 and 10.

B. Narrow-channel approximation

In the case of a narrow channel, $h \ll \lambda$, the overlapping double layers of the surfaces result in a constant charge density

$$\rho = -\varepsilon \partial_z^2 \psi = 2\sigma/h, \quad (39)$$

in other words, the counterions form a homogeneous gas [24]. The electrostatic potential is readily integrated,

$$\psi(z) = \frac{k_B T}{e} \left(\ln m - \frac{4\pi \ell_B \sigma}{h} z^2 \right), \quad (40)$$

where the parameter m describes the finite value of the potential $\psi(0) = (k_B T/e) \ln m$ at $z = 0$.

With these expressions for ρ and ψ the transport coefficients are readily calculated. Retaining contributions of leading order in h only, we find

$$L_{vc} = \frac{e\sigma h^2}{6\eta}, \quad L_{cc} = \frac{e^2 \sigma}{3\eta a_+}, \quad (41)$$

resulting in the coupling parameter

$$\xi = \sigma a_+ h. \quad (42)$$

Note that for narrow channels the conductivity is independent of salinity and gap height [29], whereas the parameter ξ is linear in h .

C. Numerical evaluation of ξ and γ

In the general case, the electrostatic potential is obtained in terms of the Jacobi elliptic function $\text{cd}(u|m^2)$ [30],

$$\psi(z) = \frac{k_B T}{e} \left[\ln m + 2 \ln \text{cd} \left(\frac{z}{2\lambda\sqrt{m}} \middle| m^2 \right) \right]. \quad (43)$$

Because of $\text{cd}(0|m^2) = 1$, the second term vanishes at $z = 0$, and the potential at $z = 0$ is determined by $\ln m$. The parameter m depends on the ratio of the channel height and the Debye length: For $h \gg \lambda$ one has $m = 1$ and recovers the analytic expression (31) for a charged surface limiting an infinite half-space. In the narrow-channel limit one finds

$$m = \frac{h n_0}{2\lambda\sigma}, \quad (h n_0 \ll \sigma), \quad (44)$$

and expanding the Jacobi function to second order in z , one recovers the potential defined in Eq. (40) above.

The electric potential is calculated numerically from (43) with the boundary condition (7). Then the electroviscous coupling parameter ξ defined in (25) is obtained by performing the integrals (20) and (21) for a given film distance h . The numerical results are given in terms of the gap height h_0 , the surface charge density σ , and the Debye screening length λ . We use the viscosity of water at room temperature, $\eta = 0.9 \times 10^{-3}$ Pa s, and the ion mobilities $\mu_{\pm} = 1/6\pi\eta a_{\pm}$ with the radii of sodium $a_+ = 1.9$ Å and of chlorine $a_- = 1.3$ Å [31].

Figure 3 shows the variation of ξ as a function of h for different values of surface charge concentration σ in comparison with narrow-channel and wide-channel approximations. As a surprising feature, ξ is roughly linear in σ . The log-log plot shows the power laws $\xi \propto h$ and $\xi \propto h^{-2}$ in the limits of narrow and wide channels, respectively. The maximum occurs at $h_{\text{max}} \approx 3\lambda$. The narrow-channel result (42) provides a good

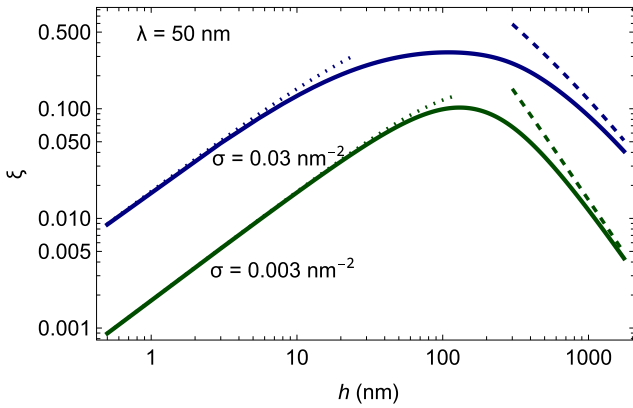


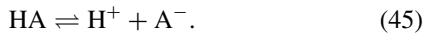
FIG. 3. Numerical calculation of the electroviscous coupling parameter ξ as a function of h , for surface charge density $\sigma = 0.003$ and 0.03 nm^{-2} , and Debye length $\lambda = 50 \text{ nm}$. Dotted and dashed lines correspond to the approximations of narrow and wide channels, respectively, whereas the solid lines give the numerical solution.

description for $h \leq \lambda$, whereas the wide-channel expression (VII A) converges for $h \gg \lambda_*$ only. In the intermediate range, which covers at least one decade in h , neither of them is valid.

In Fig. 4 we plot the enhancement factor $\gamma/\gamma_0 - 1$ of the viscous force (27), with parameters as in Fig. 3. As expected for the electroviscous coupling parameter ξ , there is a maximum at $h_0 \approx \lambda$. The enhancement factor depends equally strongly on the surface charge and the Debye length.

V. CHARGE REGULATION

So far we have assumed that the surface charge density σ remains constant upon varying the film height h_0 . This is not the case, however, for weakly dissociating acidic groups HA which release and recover protons according to [32]



For narrow channels the potential (43) takes a finite value $\psi(0) = (k_B T/e) \ln m$ at $z = 0$, which favors recombination of the surface groups, thus reducing the effective charge density σ and surface potential ζ .

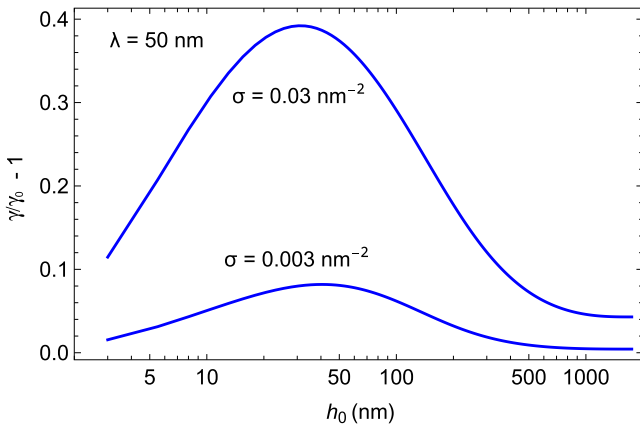


FIG. 4. Electroviscous drag enhancement $\gamma/\gamma_0 - 1$ as a function of h_0 for different values of the surface charge density σ .

A simple and widely studied model relies on the dissociation constant

$$\mathcal{Z} = \frac{[\text{H}^+][\text{A}^-]}{[\text{HA}]} = n_s \frac{\alpha}{1 - \alpha}, \quad (46)$$

where we have defined the dissociated fraction α and the hydronium concentration at the surface $n_s = e^{-e\zeta/k_B T} [\text{H}^+]_\infty$. Solving for α , one finds the fraction of dissociated sites

$$\alpha = \frac{1}{1 + n_s/\mathcal{Z}}, \quad (47)$$

and the number density of surface charges

$$\sigma = \frac{\alpha}{S}. \quad (48)$$

The electrostatic potential is obtained by closing the above relations with the boundary condition (7). The area per site S is chosen such that at large distance (where $\zeta = \zeta_\infty$), σ takes the value indicated for the case of constant charge. An alternate charging procedure which is often used for systems with more complex charging procedure but essentially leads to the same results, is via a proper minimization of the relevant thermodynamic potential [33].

In the following we compare the electrostatic and electroviscous properties calculated at constant charge (cc) with the charge-regulated case (cr), and also with that of constant potential (cp), where the boundary condition (7) is replaced with

$$\psi(\pm h/2) = \zeta_\infty. \quad (49)$$

Here ζ_∞ is the surface potential at large distance, calculated with the surface charge σ according to (31). All curves labeled “cr” are calculated with $\mathcal{Z} = 10^{-3} \text{ M}$.

A. Electroviscous coupling

In Fig. 5 we plot the coupling parameter ξ for the cases of constant charge and constant surface potential, and observe a behavior similar to what has been reported previously for the disjoining pressure [34]. At distances smaller than the screening length, $h < \lambda$, the curves of ξ for different boundary

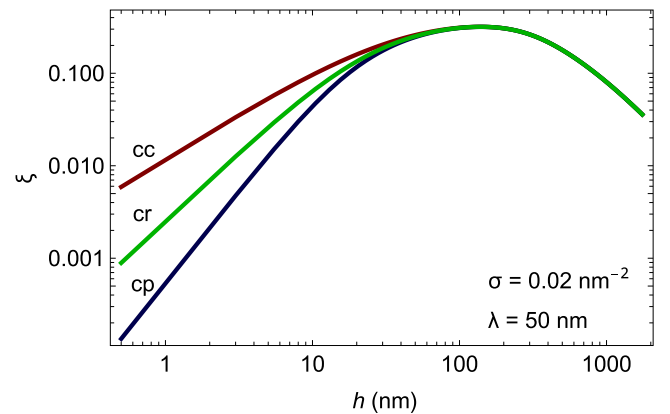


FIG. 5. Electroviscous coupling parameter ξ as a function of the distance h for constant charge (cc), charge regulation (cr), and constant potential (cp).

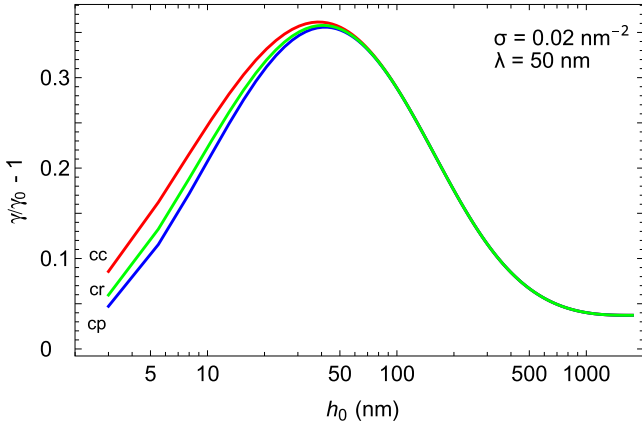


FIG. 6. Electroviscous enhancement $\gamma/\gamma_0 - 1$ as a function of the distance h_0 for different boundary conditions.

conditions diverge significantly. Yet note that the electroviscous coupling is strongest in the range $\lambda < h < 10\lambda$, where charge regulation is of little importance.

The electroviscous enhancement of the drag force γ with respect to the uncoupled expression γ_0 is shown in Fig. 6. The maximum occurs at a distance slightly below the screening length. For the given electrostatic parameters, it reaches a value of about 35%, which depends little on the electrostatic boundary condition. The electroviscous drag component disappears at much higher distances of about 10λ .

B. Disjoining pressure and static repulsion

Now we consider the static repulsive force arising from the overlap of the diffuse layers on the opposite surfaces and which is independent of the external driving. According to (43), the potential at $z = 0$ reads as $\psi(0) = (k_B T/e) \ln m$, and the disjoining pressure (8) is determined by the parameter m ,

$$\Pi = n_0 k_B T \left(m + \frac{1}{m} - 2 \right). \quad (50)$$

In Fig. 7 we plot Π calculated for constant charge (cc), constant potential (cp), and charge regulation (cr). For distances shorter than the screening length, these different boundary conditions result in significant differences. In agreement with previous work, we find a constant pressure for cp [24] and power laws $\Pi \propto h^s$ with $s = -1$ and $-\frac{1}{2}$ for cc and cr, respectively [34].

The dashed line corresponds to the widely used approximation [1]

$$\Pi_s(h) = 64\beta^2 n_0 k_B T e^{-h/\lambda}, \quad (h \gg \lambda), \quad (51)$$

which relies on the linear superposition of the double layers at the opposite surfaces, and where the parameter $\beta = \tanh(e\zeta_\infty/4k_B T)$ is given by the surface potential ζ_∞ at $h_0 \rightarrow \infty$, as defined in Eq. (32).

The repulsive force (10) between the two surfaces is calculated in Derjaguin approximation, in analogy to (27), resulting in

$$K = 2\pi R \int_{h_0}^{\infty} dh \Pi(h). \quad (52)$$

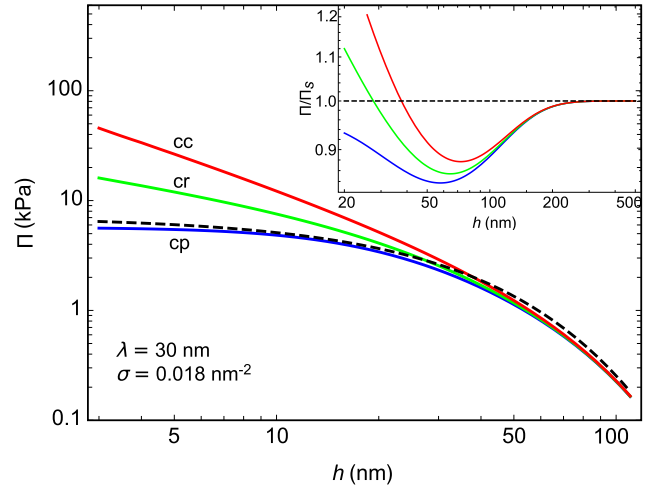


FIG. 7. Disjoining pressure between charged surfaces as a function of the distance h_0 . The solid curves give the numerical solution (8) for constant surface charge $\sigma = 0.018 \text{ nm}^{-2}$ (cc), constant potential ζ (cp), and the charge-regulated intermediate case (cr) with dissociation constant $\mathcal{Z} = 10^{-3} \text{ M}$. The approximative expression (51) is plotted as a dashed line. The inset shows the ratio Π/Π_s , highlighting the deviation of the disjoining pressure Π from the approximate expression Π_s , which sets in well above 200 nm.

For the pressure in superposition approximation we obtain $K_s = 2\pi R \lambda \Pi_s(h_0)$ and, after expressing the salt content through the Debye length,

$$K_s = \frac{16R\beta^2 k_B T}{\lambda \ell_B} e^{-h_0/\lambda}, \quad (h_0 \gg \lambda). \quad (53)$$

A comparison of the numerically exact force K with the exponential approximation K_s is given in Fig. 8. Both expressions agree beyond 200 nm, or $h_0 > 7\lambda$. The inset shows that the force calculated for constant potential (cp) remains about 10% below K_s , whereas those for constant or regulated charge (cc or cr) show a more complex behavior: they first decrease below K_s yet at even smaller h_0 by far exceed the analytic approximation K_s [1].

VI. AFM FORCE MEASUREMENT

A. Experimental detail

We performed a dynamic AFM measurement with colloidal probe following the method described in [35]. A spherical borosilicate particle (MO-Sci Corporation) with a radius of $R = 47 \pm 1 \mu\text{m}$ was glued at the end of a cantilever (CSG30, NT-MDT) using epoxy (Araldite, Bostik, Coubert). The stiffness of the ensemble of cantilever and particle was calibrated by the drainage method [36], resulting in $k_c = 0.8 \pm 0.1 \text{ N/m}$. The resonance frequency and bulk quality factor were obtained from the thermal spectrum as $\omega_0/2\pi = 3340 \text{ Hz}$ and $Q = 4.7$, respectively.

The experiment was performed using an atomic force microscope (Bioscope, Bruker, USA) equipped with a liquid cell (DTFML-DD-HE) which allows us to work in liquid environment. The mica surface was driven by a piezo (Nano T225, MCL Inc., USA) to approach the particle with a very small

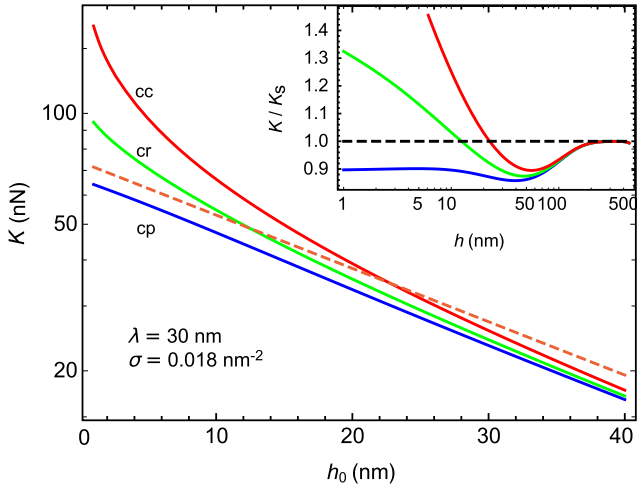


FIG. 8. Static force between charged surfaces as a function of the distance h_0 . The solid curve gives the numerical solution (10) for constant charge (upper red), constant potential (lower blue), and charge regulation (middle green). The approximative expression (53) is plotted as a dashed line. The inset shows the ratio K/K_s ; note that all curves coincide at large distance, which is not visible in the main figure.

velocity such that the drainage force can be neglected, and meanwhile the probe was also driven with a base oscillation amplitude $A_b = 3.5$ nm and frequency of $\omega/2\pi = 100$ Hz. The amplitude A and phase φ of the cantilever deflection were measured by a lock-in amplifier (Signal Recovery, model 7280), and the dc component of the cantilever deflection was also recorded, from which the separation distance h_0 and electrostatic force K between the sphere and the mica surface were extracted. The mica surface and cantilever probe are immersed in low-salinity water. We also performed control experiments at large salinity. All measurements were done at room temperature, 21 °C.

B. Static force

Figure 9 shows the electrostatic repulsive force between the mica surface and the colloidal probe. The data roughly show an exponential behavior, as expected for a screened double-layer interaction. The upper (red) curve is calculated from Eq. (52) for constant charge number density $\sigma = 0.028$ nm $^{-2}$ and the lower (blue) one for constant surface potential $\zeta = -95$ mV. In the range where both curves coincide, $h_0 > \lambda$, the best fit is obtained with a screening length $\lambda = 47$ nm, corresponding to an electrolyte strength $n_0 = 43$ μ M.

C. Spring constant and drag coefficient

Driving of the probe induces an oscillation of the tip-surface distance according to $h_0 + Z(t)$. Modeling the cantilever as a damped harmonic oscillator [21] and solving its equation of motion for the force F exerted by the surrounding liquid, we obtain in complex notation

$$F = -k_c Z \left[1 - \left(\frac{\omega}{\omega_0} \right)^2 + i \frac{\omega}{\omega_0 Q} \right] \frac{A e^{i\varphi} - A_\infty e^{i\varphi_\infty}}{A e^{i\varphi} + A_b}, \quad (54)$$

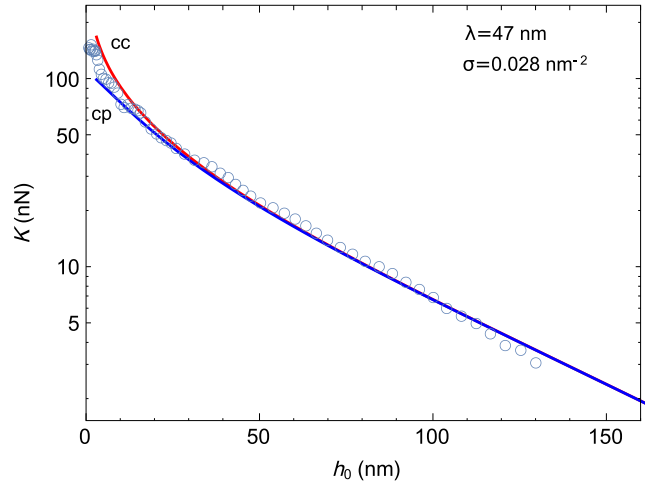


FIG. 9. Static repulsion K between the AFM sphere and the solid surface as a function of the distance h_0 . The squares give experimental data. The blue and red curves are calculated from (52) for constant potential and constant surface charge, respectively, with the parameter values $R = 55$ μ m, surface charge density $\sigma = 0.028$ nm $^{-2}$, and screening length $\lambda = 47$ nm.

with amplitude A and phase φ of the mica surface. The tip-surface distance reads as $Z(t) = e^{i\omega t} (A e^{i\varphi} + A_b)$, and the values A_∞ and φ_∞ are measured far from the surface, where the viscoelastic force F is negligible. All measurements are done in the linear-response regime $|Z| \ll h_0$.

In view of Eq. (1) we split F/Z in its real and imaginary components. Writing the velocity as $V = i\omega Z$, we readily obtain the complex response function,

$$F = -(k + i\omega\gamma)Z, \quad (55)$$

where the “spring constant” k and the drag coefficient γ account for the elastic and viscous components of the tip-surface interactions.

In Fig. 10 we plot the measured real and imaginary coefficients as a function of the separation distance h_0 at low or high salinity, at the oscillation frequency of $\omega/2\pi = 100$ Hz. At large salinity electrokinetic effects disappear because of

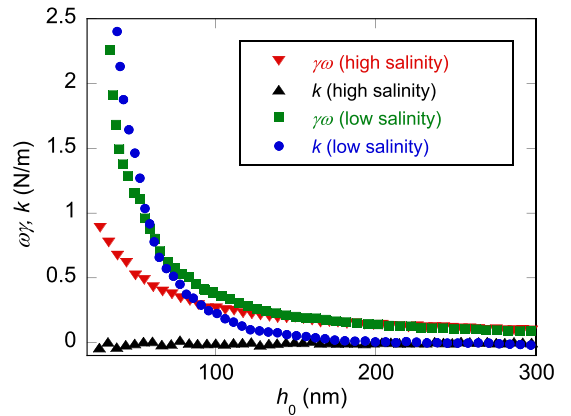


FIG. 10. Real and imaginary parts k and $\omega\gamma$ of the response function, measured at a vibrational frequency $\omega/2\pi = 100$ Hz and at low or high salinity, as a function of the distance h_0 .

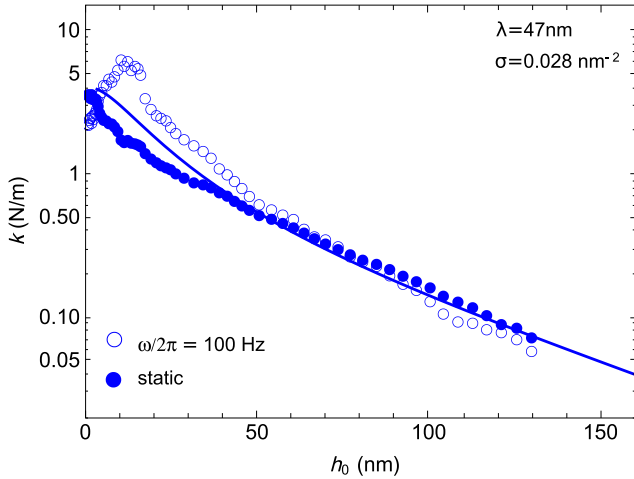


FIG. 11. Elastic response k measured at $\omega/2\pi = 100$ Hz (open symbols) and for the static case (full symbols) as a function of h_0 . The solid line gives the static rigidity k , calculated from Eq. (11), for constant potential. The experimental data are binned such that each point corresponds to the mean value of 100 measured values.

electrostatic screening, and k vanishes accordingly, whereas the drag coefficient follows the law $\gamma_0 \propto 1/h_0$, expected from Stokes hydrodynamics [26]. Quite a different behavior occurs at low salinity, where we observe a strong elastic component k which decays roughly exponentially with h_0 , and an electroviscous enhancement of the drag coefficient.

In Figs. 11 and 12, the experimental findings are compared with theory. Regarding the elastic response, Fig. 11 shows both the static stiffness $-dK/dh_0$ (full symbols) and the dynamic response $k(\omega)$ at finite frequency $\omega/2\pi = 100$ Hz (open symbols). The theory curve represents the spring constant (11), which is related to the variation of the disjoining pressure with distance and which is calculated from (8) at constant potential (cp). The data roughly follow the expo-

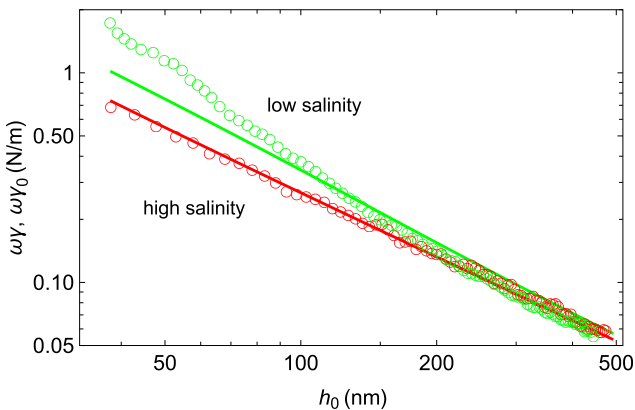


FIG. 12. Comparison of the drag coefficient measured at $\omega/2\pi = 100$ Hz (circles) with theory (solid curves). At high salinity ($\lambda < 1$ nm, red), the data are well fitted by $\omega\gamma_0$ with the drag coefficient given by (30). At low salinity ($\lambda = 47$ nm, green) we observe a significant electroviscous enhancement, which is qualitatively accounted for by $\omega\gamma$ calculated from (28). For narrow gaps the measured data exceed the theory curve by up to 60%.

nential law expected for double-layer interactions, and they provide strong evidence that the dynamic elastic response $k(\omega)$ comprises a frequency-dependent contribution which is most significant at small distances, $h_0 < \lambda$, and which is not captured by the electrostatic disjoining pressure Π .

In Fig. 12 we plot the viscous response function $\omega\gamma$. At high salinity, the electric double layer is thin ($\lambda < 1$ nm), such that charge-flow coupling effects are absent. Indeed, the drag coefficient is well fitted by the viscous contribution $\gamma_0 = 6\pi\eta R^2/h_0$, as expected from (30). At low salinity, the large screening length $\lambda = 47$ nm, comparable to h_0 , results in charge-advection and electro-osmotic flow, which increase the hydrodynamic pressure and thus enhance the drag coefficient. The theory curve is calculated numerically from Eq. (28), with the same parameters $\sigma = 0.028$ nm² and $\lambda = 47$ nm as in Figs. 9 and 11. If the overall behavior of the data is rather well described by the theoretical expression, a significant discrepancy occurs for small gaps, where the data exceed the theoretical curve by up to 60%. Comparison with the elastic coefficient shown in Fig. 11 suggests a frequency dependence of the dynamic response function $k(\omega) + i\omega\gamma(\omega)$, which is not captured by the quasistatic coefficients k and γ derived in the present work.

VII. DISCUSSION

A. Validity of the wide-channel approximation

If the double layers on either side of the water film do not overlap, their properties are given by the Poisson-Boltzmann potential (31) calculated for an infinite half-space. As the surfaces get closer, the diffuse layers start to interact, resulting in electrostatic repulsion and electroviscous coupling. In the range where the distance h_0 is moderately larger than the Debye length λ , widely used approximations result in an exponentially screened electrostatic repulsion [37] and in a power-law dependence of the electroviscous drag [15].

Its range of validity is obviously related to the Debye length λ , yet our analysis shows that in reality it is limited by a significantly larger distance λ_* , defined in (36). With typical values of the ζ potential ranging from 25 to 100 mV, the parameter λ_* may be up to 10 times larger than the actual screening length λ . This is clearly displayed by the electroviscous coupling parameter plotted in Fig. 3. The wide-channel approximation converges only at $h_0 \gg \lambda$. As a consequence, at distances of the order of or smaller than λ_* , the force can be calculated only numerically.

B. The effect of charge regulation

There are two length scales indicating a qualitative change of the electrostatic properties, as illustrated by the parameter m of the Jacobi elliptic function $\text{cd}(u|m^2)$ in Eq. (43), which is plotted in Fig. 13. For very large channels one has $m = 1$, which means that the double layers at opposite surfaces do not interact. The onset of the electrostatic coupling occurs at a film height λ_* which increases with the surface charge density σ , as shown by the curves of Fig. 13.

On the other hand, the electrostatic boundary conditions and charge regulation are relevant at smaller distances, and their onset shows the opposite behavior as a function of the surface charge density. Indeed, for $\sigma = 0.001$ nm⁻² the three

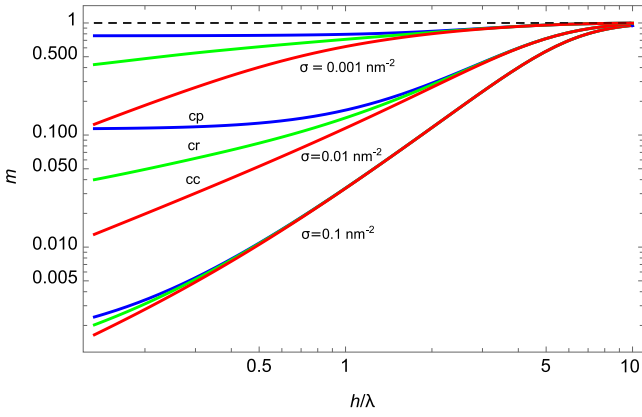


FIG. 13. The parameter m of the electrostatic potential (43) as a function of reduced channel height h/λ for three values of the surface charge density σ and for constant charge (cc, red), constant potential (cp, blue), and charge regulation (cr, green). There are two different length scales: The onset of electrostatic coupling of the two diffuse layers, where m starts to decrease below 1, occurs at a distance $h_* = 2\pi\sigma\ell_B\lambda^2$ which increases with σ . On the other hand, the electrostatic boundary condition and charge regulation (cc, cr, cp) are relevant at shorter distances, and there onset occurs at a distance which is inversely proportional to the surface charge density.

curves (cc, cp, cr) start diverging at $h = \lambda$, whereas for $\sigma = 0.1 \text{ nm}^{-2}$ this occurs at much smaller distances.

These features can be observed for both the electrostatic repulsion and electroviscous effects. Regarding the former, the two length scales for the onset of nonexponential behavior and charge regulation effects are clearly visible in the inset of Fig. 8. Similarly, the electroviscous coupling parameter ξ in Fig. 5 and the enhancement of the drag coefficient in Fig. 6 show characteristic wide-channel power laws for $h \gg \lambda$, whereas charge regulation effects occur at distances shorter than the screening length.

C. Electrokinetic lift force

In this work we have considered the electroviscous force (27) only. As pointed out by Bike and Prieve [15], there is an additional electrokinetic force given by the diagonal part $\frac{1}{2}\varepsilon E^2$ of the Maxwell stress tensor,

$$F_{\text{el}} = 2\pi R \int_{h_0}^{\infty} dh \frac{\varepsilon E^2}{2}, \quad (56)$$

with the electric field (23). Because of $E \propto V$, this “lift force” is quadratic in the driving velocity $V \propto \cos \omega t$. As a consequence, $F_{\text{el}} \propto \cos^2 \omega t$ is always repulsive and oscillates with the double frequency, contrary to the electroviscous force $F = -\gamma V$, which is opposite to the velocity and oscillates with ω .

The present experiments on squeezing motion do not show any indication of the lift force F_{el} . This does not come as a surprise: inserting the wide-channel expressions of the transport coefficients L_{ij} and a typical velocity $V = 100 \text{ nm/s}$, we find

$$F_{\text{el}} \sim \varepsilon \zeta^2 \left(\frac{\lambda^2 a \eta V R}{h_0^2 k_B T} \right)^2 \sim 10^{-17} \text{ N}, \quad (57)$$

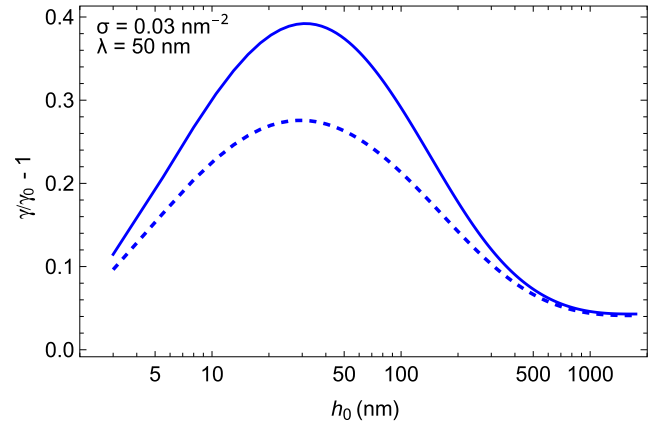


FIG. 14. Numerical calculation of the electroviscous enhancement of the drag coefficient $\gamma/\gamma_0 - 1$ as a function of h_0 , for $\sigma = 0.03 \text{ nm}^{-2}$ and $\lambda = 50 \text{ nm}$. The solid line is calculated with the full pressure (24) and the dashed line that with the linearized expression (58).

which is much smaller than the electroviscous force $F \sim 10^{-9} \text{ N}$.

For sliding motion along the surface, on the contrary, the lift force F_{el} turns out to be important. Due to the symmetry properties of the unperturbed pressure P_0 , the corresponding vertical force vanishes, $F = \int dSP_0 = 0$ [15]. Moreover, the horizontal speed \dot{X} of the sliding motion is typically of the order of 10 mm/s , much larger than the vertical velocity $V = \dot{Z}$ in the present experiment.

D. Comparison with previous work

Electroviscous effects on squeezing motion have been studied in several previous papers [15,21–23]. All of these works start, more or less explicitly, from the volume and charge currents (14) and (15). Yet when calculating the charge current J_C they use the unperturbed pressure gradient $\nabla P_0 = -6\eta rV/h^3$ instead of ∇P . This perturbative approach corresponds to a linearization of the pressure gradient in the coupling parameter ξ ,

$$\nabla P_1 = \nabla P_0(1 + \xi), \quad (58)$$

instead of the exact expression (24).

As a consequence, electroviscous effects appear as an additive correction to the unperturbed drag force F_0 . Thus the wide-channel force of Bike and Prieve [15] is identical to the first two terms of (38), whereas our expression (37) corresponds to the full series in λ_*/h_0 . Similarly, the numerical calculations of Chun and Ladd [22] and Zhao *et al.* [23] are done with the linearized pressure gradient P_1 .

In Fig. 14 we compare the electroviscous enhancement of the drag force, calculated with the numerically exact pressure gradient (24) and with the linearized form P_1 . For the parameters $\lambda = 50 \text{ nm}$ and $\sigma = 0.03 \text{ nm}^{-2}$, the linearized drag coefficient (dashed line) is by 28% larger than γ_0 , whereas the increase of the full expression (solid line) attains 40%. This difference is not surprising in view of the coupling parameters shown in Fig. 3; in the intermediate range where ξ reaches

values of the order of unity, one expects a significant nonlinear behavior.

VIII. SUMMARY

We have studied the electroviscous and electrostatic forces exerted on a vibrating AFM tip across a nanoscale water film. We briefly summarize the main findings.

(i) In the framework of Onsager relations for generalized fluxes and forces, we derive the drag coefficient (28) in terms of the electroviscous coupling parameter ξ . With the surface charge σ and the screening length λ taken from the electrostatic repulsion (Fig. 9), we find an almost quantitative agreement with experimental data (Fig. 12), with a discrepancy attaining 60% in the narrow-gap limit.

(ii) This analysis relies on a quasistatic approximation (22), where the radial charge distribution in the water film is assumed to follow instantaneously the external driving. The fits of the viscous and elastic components of the response function (55), measured at $\omega/2\pi = 100$ Hz and shown in Figs. 11 and 12, suggest that this approximation is justified at distances larger than the screening length yet ceases to be valid for $h_0 < \lambda$. Our experimental data strongly suggest that in this range both the spring constant k and the drag coefficient γ

vary with frequency. The nature of the underlying relaxation process is not clear at present.

(iii) Previous work relied on the linearization approximation (58) for the hydrodynamic pressure gradient. This linearization significantly underestimates the enhancement of the drag coefficients for the parameters of Fig. 14 by about 40%.

(iv) Charge regulation turns out to be of minor importance in the experimentally most relevant range. Indeed, the electroviscous coupling sets in at large distances and is maximum at $h_0 \sim 3\lambda$ (Fig. 3), whereas the electrostatic boundary conditions and charge regulation effects are significant in narrow channels only, as shown in Figs. 5–9.

ACKNOWLEDGMENTS

This project was supported by the French National Research Agency through Grant No. ANR-19-CE30-0012. M.R.M. acknowledges funding support from the Mexican Council for Science and Technology (CONACYT) through Grant No. CVU 625862. Z.Z. acknowledges funding support from the Chinese Scholarship Council (CSC) under Grant No. 201606020114.

-
- [1] J. N. Israelachvili, *Intermolecular and Surface Forces*, 2nd ed. (Academic Press, San Diego, CA, 1991).
 - [2] J. Israelachvili and H. Wennerström, *Nature (London)* **379**, 219 (1996).
 - [3] J. Lyklema, *Fundamentals of Interface and Colloid Science* (Academic Press, New York, 1995).
 - [4] H. A. Stone, A. D. Stroock, and A. Ajdari, *Annu. Rev. Fluid Mech.* **36**, 381 (2004).
 - [5] J. Yan, M. Han, J. Zhang, C. Xu, E. Luijten, and S. Granick, *Nat. Mater.* **15**, 1095 (2016).
 - [6] S. Marbach and L. Bocquet, *Chem. Soc. Rev.* **48**, 3102 (2019).
 - [7] L. Bocquet and E. Charlaix, *Chem. Soc. Rev.* **39**, 1073 (2010).
 - [8] H. Helmholtz, *Ann. Phys.* **243**, 337 (1879).
 - [9] M. von Smoluchowski, *Bull. Int. Acad. Sci. Cracovie* **8**, 182 (1903).
 - [10] J. J. Bikerman, *Z. physikal. Chemie A* **163**, 378 (1903); S. S. Dukhin and B. V. Derjaguin, in *Electrokinetic Phenomena*, edited by E. Matijevic, *Surface and Colloid Science* (Wiley, New York, 1974), Vol. 7.
 - [11] E. Hückel, *Physik. Z.* **25**, 204 (1924).
 - [12] D. C. Henry, *Proc. R. Soc. Lond. A* **133**, 106 (1931).
 - [13] R. J. Gross and J. F. Osterle, *J. Chem. Phys.* **49**, 228 (1968).
 - [14] B. M. Alexander and D. C. Prieve, *Langmuir* **3**, 788 (1987).
 - [15] S. G. Bie and D. C. Prieve, *J. Colloid Interface Sci.* **136**, 95 (1990).
 - [16] S. G. Bie and D. C. Prieve, *J. Colloid Interface Sci.* **154**, 87 (1992).
 - [17] S. G. Bie, L. Lazarro, and D. C. Prieve, *J. Colloid Interface Sci.* **175**, 411 (1995).
 - [18] S. G. Bie and D. C. Prieve, *J. Colloid Interface Sci.* **175**, 422 (1995).
 - [19] R. Raiteri, M. Grattarola, and H.-J. Butt, *J. Phys. Chem.* **100**, 16700 (1996).
 - [20] F. Liu, C. Zhao, F. Mugele, and D. van den Ende, *Nanotechnology* **26**, 385703 (2015).
 - [21] F. Liu, A. Klaassen, C. Zhao, F. Mugele, and D. van den Ende, *J. Phys. Chem. B* **122**, 933 (2018).
 - [22] B. Chun and A. Ladd, *J. Colloid Interface Sci.* **274**, 687 (2004).
 - [23] C. Zhao, W. Zhang, D. van den Ende, and F. Mugele, *J. Fluid Mech.* **888**, A29 (2020).
 - [24] D. Andelman, in *Soft Condensed Matter Physics in Molecular and Cell Biology*, edited by W. Poon and D. Andelman (Taylor & Francis, New York, 2006), pp. 97–122.
 - [25] B. Derjaguin, *Kolloid-Zeitschrift* **69**, 155 (1934).
 - [26] J. Happel and H. Brenner, *Low Reynolds Number Hydrodynamics* (Martinus Nijhoff, The Hague, 1963).
 - [27] J. L. Anderson, *Annu. Rev. Fluid Mech.* **21**, 61 (1989).
 - [28] H. Brenner, *Chem. Eng. Sci.* **16**, 242 (1961).
 - [29] D. Stein, M. Kruijthof, and C. Dekker, *Phys. Rev. Lett.* **93**, 035901 (2004).
 - [30] M. Abramowitz and I. A. Stegun, *Handbook of Mathematical Functions* (Dover, New York, 1964).
 - [31] L. A. Bulavin, I. V. Zhyganiuk, M. P. Malomuzh, and K. M. Pankratov, *Ukr. J. Phys.* **56**, 893 (2011).
 - [32] B. W. Ninham and V. A. Parsegian, *J. Theor. Biol.* **31**, 405 (1971).
 - [33] A. Majee, M. Bier, and R. Podgornik, *Soft Matter* **14**, 985 (2018).
 - [34] T. Markovich, D. Andelman, and R. Podgornik, *Europhys. Lett.* **113**, 26004 (2016).
 - [35] A. Maali and R. Boisgard, *J. Appl. Phys.* **114**, 144302 (2013).
 - [36] V. S. J. Craig and C. Neto, *Langmuir* **17**, 6018 (2001).
 - [37] J. Israelachvili, *J. Colloid Interface Sci.* **110**, 263 (1986).

Bibliography

- [1] K.-i. Ohno, K. Tachikawa, and A. Manz, "Microfluidics: applications for analytical purposes in chemistry and biochemistry," *Electrophoresis*, vol. 29, no. 22, pp. 4443–4453, 2008.
- [2] D. J. Beebe, G. A. Mensing, and G. M. Walker, "Physics and applications of microfluidics in biology," *Annual review of biomedical engineering*, vol. 4, no. 1, pp. 261–286, 2002.
- [3] J. C. Eijkel and A. v. d. Berg, "Nanofluidics: what is it and what can we expect from it?," *Microfluidics and Nanofluidics*, vol. 1, no. 3, pp. 249–267, 2005.
- [4] R. B. Schoch, J. Han, and P. Renaud, "Transport phenomena in nanofluidics," *Reviews of modern physics*, vol. 80, no. 3, p. 839, 2008.
- [5] W. Sparreboom, A. van den Berg, and J. C. Eijkel, "Principles and applications of nanofluidic transport," *Nature nanotechnology*, vol. 4, no. 11, pp. 713–720, 2009.
- [6] P. Abgrall and N. T. Nguyen, "Nanofluidic devices and their applications," *Analytical chemistry*, vol. 80, no. 7, pp. 2326–2341, 2008.
- [7] K. V. Wong and O. De Leon, "Applications of nanofluids: current and future," *Nanotechnology and Energy*, pp. 105–132, 2017.
- [8] L. Zhang and X. Chen, "Nanofluidics for giant power harvesting," *Angewandte Chemie International Edition*, vol. 52, no. 30, pp. 7640–7641, 2013.
- [9] A. Siria, P. Poncharal, A.-L. Biance, R. Fulcrand, X. Blase, S. T. Purcell, and L. Bocquet, "Giant osmotic energy conversion measured in a single transmembrane boron nitride nanotube," *Nature*, vol. 494, no. 7438, pp. 455–458, 2013.
- [10] R. Garud, S. Kore, V. Kore, and G. Kulkarni, "A short review on process and applications of reverse osmosis," *Universal Journal of Environmental Research & Technology*, vol. 1, no. 3, 2011.
- [11] M. Qasim, M. Badrelzaman, N. N. Darwish, N. A. Darwish, and N. Hilal, "Reverse osmosis desalination: A state-of-the-art review," *Desalination*, vol. 459, pp. 59–104, 2019.
- [12] L. Bocquet and P. Tabeling, "Physics and technological aspects of nanofluidics," *Lab on a Chip*, vol. 14, no. 17, pp. 3143–3158, 2014.
- [13] H. Daiguji, Y. Oka, T. Adachi, and K. Shirono, "Theoretical study on the efficiency of nanofluidic batteries," *Electrochemistry communications*, vol. 8, no. 11, pp. 1796–1800, 2006.

- [14] Y. Yan, Q. Sheng, C. Wang, J. Xue, and H.-C. Chang, "Energy conversion efficiency of nanofluidic batteries: hydrodynamic slip and access resistance," *The Journal of Physical Chemistry C*, vol. 117, no. 16, pp. 8050–8061, 2013.
- [15] I. Vlassiouk and Z. S. Siwy, "Nanofluidic diode," *Nano letters*, vol. 7, no. 3, pp. 552–556, 2007.
- [16] R. Karnik, C. Duan, K. Castelino, H. Daiguji, and A. Majumdar, "Rectification of ionic current in a nanofluidic diode," *Nano letters*, vol. 7, no. 3, pp. 547–551, 2007.
- [17] A. Giannitsis and M. Min, "Usage of microfluidic lab-on-chips in biomedicine," in *2010 12th Biennial Baltic Electronics Conference*, pp. 249–252, IEEE, 2010.
- [18] M. L. Kovarik and S. C. Jacobson, "Nanofluidics in lab-on-a-chip devices," 2009.
- [19] V. C. Romao, S. A. Martins, J. Germano, F. A. Cardoso, S. Cardoso, and P. P. Freitas, "Lab-on-chip devices: gaining ground losing size," *ACS nano*, vol. 11, no. 11, pp. 10659–10664, 2017.
- [20] J. N. Israelachvili, *Intermolecular and surface forces*. Academic press, 2011.
- [21] Z. Stojek, "The electrical double layer and its structure," in *Electroanalytical methods*, pp. 3–9, Springer, 2010.
- [22] M. J. Gordon, X. Huang, S. L. Pentoney Jr, and R. N. Zare, "Capillary electrophoresis," *Science*, vol. 242, no. 4876, pp. 224–228, 1988.
- [23] Y. Picó, *Chemical analysis of food: Techniques and applications*. Academic Press, 2012.
- [24] E. Klaseboer and D. Y. Chan, "On the derivation of the smoluchowski result of electrophoretic mobility," *Journal of Colloid and Interface Science*, vol. 568, pp. 176–184, 2020.
- [25] J. Lyklema, "Electrokinetics after smoluchowski," *Colloids and surfaces A: physicochemical and engineering aspects*, vol. 222, no. 1-3, pp. 5–14, 2003.
- [26] S. May, "Differential capacitance of the electric double layer: Mean-field modeling approaches," *Current Opinion in Electrochemistry*, vol. 13, pp. 125–131, 2019.
- [27] D.-e. Jiang, D. Meng, and J. Wu, "Density functional theory for differential capacitance of planar electric double layers in ionic liquids," *Chemical Physics Letters*, vol. 504, no. 4-6, pp. 153–158, 2011.
- [28] P. Cats and R. van Roij, "The differential capacitance as a probe for the electric double layer structure and the electrolyte bulk composition," *The Journal of Chemical Physics*, vol. 155, no. 10, p. 104702, 2021.
- [29] J. M. Black, M. Zhu, P. Zhang, R. R. Unocic, D. Guo, M. B. Okatan, S. Dai, P. T. Cummings, S. V. Kalinin, G. Feng, *et al.*, "Fundamental aspects of electric double layer force-distance measurements at liquid-solid interfaces using atomic force microscopy," *Scientific reports*, vol. 6, no. 1, pp. 1–12, 2016.

- [30] A. C. Hillier, S. Kim, and A. J. Bard, "Measurement of double-layer forces at the electrode/electrolyte interface using the atomic force microscope: potential and anion dependent interactions," *The Journal of Physical Chemistry*, vol. 100, no. 48, pp. 18808–18817, 1996.
- [31] W. C. Poon and D. Andelman, *Soft condensed matter physics in molecular and cell biology*. CRC Press, 2006.
- [32] D. Andelman, "Introduction to electrostatics in soft and biological matter," *Soft condensed matter physics in molecular and cell biology*, vol. 6, 2006.
- [33] R. B. Schoch, J. Han, and P. Renaud, "Transport phenomena in nanofluidics," *Reviews of modern physics*, vol. 80, no. 3, p. 839, 2008.
- [34] S.-J. Park and M.-K. Seo, *Interface science and composites*, vol. 18. Academic Press, 2011.
- [35] B. Bhattacharyya, *Electrochemical micromachining for nanofabrication, MEMS and nanotechnology*. William Andrew, 2015.
- [36] M. A. Brown, A. Goel, and Z. Abbas, "Effect of electrolyte concentration on the stern layer thickness at a charged interface," *Angewandte Chemie*, vol. 128, no. 11, pp. 3854–3858, 2016.
- [37] S. Babu, *Advances in chemical mechanical planarization (CMP)*. Woodhead Publishing, 2016.
- [38] Y. Sudhakar, M. Selvakumar, and D. K. Bhat, *Biopolymer electrolytes: fundamentals and applications in energy storage*. Elsevier, 2018.
- [39] M. Inagaki, K. Kaneko, M. Endo, A. Oya, and Y. Tanabe, *Carbon alloys: novel concepts to develop carbon science and technology*. Elsevier, 2003.
- [40] M. S. Halper and J. C. Ellenbogen, "Supercapacitors: A brief overview," *The MITRE Corporation, McLean, Virginia, USA*, vol. 1, 2006.
- [41] W. Schmickler, "Electronic effects in the electric double layer," *Chemical reviews*, vol. 96, no. 8, pp. 3177–3200, 1996.
- [42] R. Schweiss, P. B. Welzel, C. Werner, and W. Knoll, "Dissociation of surface functional groups and preferential adsorption of ions on self-assembled monolayers assessed by streaming potential and streaming current measurements," *Langmuir*, vol. 17, no. 14, pp. 4304–4311, 2001.
- [43] D. E. Yates, S. Levine, and T. W. Healy, "Site-binding model of the electrical double layer at the oxide/water interface," *Journal of the Chemical Society, Faraday Transactions 1: Physical Chemistry in Condensed Phases*, vol. 70, pp. 1807–1818, 1974.
- [44] B. Derjaguin and M. Kussakov, "Anomalous properties of thin polymolecular films," *Acta Physicochim. URSS*, vol. 10, no. 1, pp. 25–44, 1939.
- [45] A. G. Moreira and R. R. Netz, "Binding of similarly charged plates with counterions only," *Physical review letters*, vol. 87, no. 7, p. 078301, 2001.

- [46] H.-J. Butt, “Measuring electrostatic, van der waals, and hydration forces in electrolyte solutions with an atomic force microscope,” *Biophysical journal*, vol. 60, no. 6, pp. 1438–1444, 1991.
- [47] G. Trefalt and M. Borkovec, “Overview of dlvo theory,” 2014.
- [48] G. Peschel, P. Belouschek, M. Müller, M. Müller, and R. König, “The interaction of solid surfaces in aqueous systems,” *Colloid and Polymer Science*, vol. 260, no. 4, pp. 444–451, 1982.
- [49] J. N. Israelachvili and G. E. Adams, “Measurement of forces between two mica surfaces in aqueous electrolyte solutions in the range 0–100 nm,” *Journal of the Chemical Society, Faraday Transactions 1: Physical Chemistry in Condensed Phases*, vol. 74, pp. 975–1001, 1978.
- [50] R. Pashley, “Hydration forces between mica surfaces in aqueous electrolyte solutions,” *Journal of colloid and interface science*, vol. 80, no. 1, pp. 153–162, 1981.
- [51] A. M. Smith, M. Borkovec, and G. Trefalt, “Forces between solid surfaces in aqueous electrolyte solutions,” *Advances in colloid and interface science*, vol. 275, p. 102078, 2020.
- [52] A. Asadi, B. B. Huat, H. Nahazanan, and H. A. Keykhah, “Theory of electroosmosis in soil,” *International Journal of Electrochemical Science*, vol. 8, no. 1, pp. 1016–1025, 2013.
- [53] C. M. Brotherton and R. H. Davis, “Electroosmotic flow in channels with step changes in zeta potential and cross section,” *Journal of colloid and interface science*, vol. 270, no. 1, pp. 242–246, 2004.
- [54] H. C. Ma and H. J. Keh, “Diffusioosmosis of electrolyte solutions in a fine capillary slit,” *Journal of colloid and interface science*, vol. 298, no. 1, pp. 476–486, 2006.
- [55] H. C. Ma and H. J. Keh, “Diffusioosmosis of electrolyte solutions in a capillary slit with surface charge layers,” *Colloids and Surfaces A: Physicochemical and Engineering Aspects*, vol. 267, no. 1-3, pp. 4–15, 2005.
- [56] D. Velegol, A. Garg, R. Guha, A. Kar, and M. Kumar, “Origins of concentration gradients for diffusiohoresis,” *Soft matter*, vol. 12, no. 21, pp. 4686–4703, 2016.
- [57] J. T. Ault, P. B. Warren, S. Shin, and H. A. Stone, “Diffusiohoresis in one-dimensional solute gradients,” *Soft matter*, vol. 13, no. 47, pp. 9015–9023, 2017.
- [58] X. Xuan, “Ion separation in nanofluidics,” *Electrophoresis*, vol. 29, no. 18, pp. 3737–3743, 2008.
- [59] Y. Leng, “Hydration force between mica surfaces in aqueous kcl electrolyte solution,” *Langmuir*, vol. 28, no. 12, pp. 5339–5349, 2012.
- [60] A. Maali and R. Boisgard, “Precise damping and stiffness extraction in acoustic driven cantilever in liquid,” *Journal of Applied Physics*, vol. 114, no. 14, p. 144302, 2013.

- [61] F. Liu, A. Klaassen, C. Zhao, F. Mugele, and D. Van Den Ende, “Electroviscous dissipation in aqueous electrolyte films with overlapping electric double layers,” *The Journal of Physical Chemistry B*, vol. 122, no. 2, pp. 933–946, 2018.
- [62] W. R. Bowen and F. Jenner, “Electroviscous effects in charged capillaries,” *Journal of colloid and interface science*, vol. 173, no. 2, pp. 388–395, 1995.
- [63] J. Lyklema and J. T. G. Overbeek, “On the interpretation of electrokinetic potentials,” *Journal of Colloid Science*, vol. 16, no. 5, pp. 501–512, 1961.
- [64] D. Stigter, “On the viscoelectric effect in colloidal solutions¹,” *The Journal Of Physical Chemistry*, vol. 68, no. 12, pp. 3600–3602, 1964.
- [65] W.-L. Hsu, D. J. Harvie, M. R. Davidson, D. E. Dunstan, J. Hwang, and H. Daiguji, “Viscoelectric effects in nanochannel electrokinetics,” *The Journal of Physical Chemistry C*, vol. 121, no. 37, pp. 20517–20523, 2017.
- [66] R. Cox, “Electroviscous forces on a charged particle suspended in a flowing liquid,” *Journal of Fluid Mechanics*, vol. 338, pp. 1–34, 1997.
- [67] E. Yariv, O. Schnitzer, and I. Frankel, “Streaming-potential phenomena in the thin-debye-layer limit. part 1. general theory,” *Journal of fluid mechanics*, vol. 685, pp. 306–334, 2011.
- [68] O. Schnitzer, I. Frankel, and E. Yariv, “Streaming-potential phenomena in the thin-debye-layer limit. part 2. moderate pécelet numbers,” *Journal of fluid mechanics*, vol. 704, pp. 109–136, 2012.
- [69] J. R. Brauer, *Magnetic actuators and sensors*. John Wiley & Sons, 2006.
- [70] P. Warszyński, X. Wu, and T. Van De Ven, “Electrokinetic lift force for a charged particle moving near a charged wall—a modified theory and experiment,” *Colloids and Surfaces A: Physicochemical and Engineering Aspects*, vol. 140, no. 1-3, pp. 183–198, 1998.
- [71] T. G. van de Ven, P. Warszynski, and S. Dukhin, “Electrokinetic lift of small particles,” *Journal of colloid and interface science*, vol. 157, no. 2, pp. 328–331, 1993.
- [72] X. Wu, P. Warszynski, and T. G. van de Ven, “Electrokinetic lift: observations and comparisons with theories,” *Journal of colloid and interface science*, vol. 180, no. 1, pp. 61–69, 1996.
- [73] S. Bike and D. Prieve, “Electrokinetic lift of a sphere moving in slow shear flow parallel to a wall: Ii. theory,” *Journal of Colloid and Interface science*, vol. 175, no. 2, pp. 422–434, 1995.
- [74] S. G. Bike and D. C. Prieve, “Electrohydrodynamic lubrication with thin double layers,” *Journal of colloid and interface science*, vol. 136, no. 1, pp. 95–112, 1990.
- [75] O. Schnitzer and E. Yariv, “Streaming-potential phenomena in the thin-debye-layer limit. part 3. shear-induced electroviscous repulsion,” *Journal of Fluid Mechanics*, vol. 786, pp. 84–109, 2016.

- [76] O. Schnitzer, I. Frankel, and E. Yariv, “Shear-induced electrokinetic lift at large péclet numbers,” *Mathematical Modelling of Natural Phenomena*, vol. 7, no. 4, pp. 64–81, 2012.
- [77] T. Markovich, D. Andelman, and R. Podgornik, “Charged membranes: Poisson–boltzmann theory, the dlvo paradigm, and beyond,” in *Handbook of lipid membranes*, pp. 99–128, CRC Press, 2021.
- [78] C. Herrero and L. Joly, “Poisson-boltzmann formulary,” *arXiv preprint arXiv:2105.00720*, 2021.
- [79] C. Gray and P. J. Stiles, “Nonlinear electrostatics: the poisson–boltzmann equation,” *European Journal of Physics*, vol. 39, no. 5, p. 053002, 2018.
- [80] K. B. Lipkowitz, T. R. Cundari, and D. B. Boyd, *Reviews in computational chemistry*. John Wiley & Sons, 2008.
- [81] D. Andelman, “Electrostatic properties of membranes: the poisson-boltzmann theory,” in *Handbook of biological physics*, vol. 1, pp. 603–642, Elsevier, 1995.
- [82] S. H. Behrens and M. Borkovec, “Electrostatic interaction of colloidal surfaces with variable charge,” *The Journal of Physical Chemistry B*, vol. 103, no. 15, pp. 2918–2928, 1999.
- [83] D. McCormack, S. L. Carnie, and D. Y. Chan, “Calculations of electric double-layer force and interaction free energy between dissimilar surfaces,” *Journal of Colloid and Interface Science*, vol. 169, no. 1, pp. 177–196, 1995.
- [84] S. H. Behrens and M. Borkovec, “Exact poisson-boltzmann solution for the interaction of dissimilar charge-regulating surfaces,” *Physical Review E*, vol. 60, no. 6, p. 7040, 1999.
- [85] I. N. Derbenev, A. V. Filippov, A. J. Stace, and E. Besley, “Electrostatic interactions between charged dielectric particles in an electrolyte solution: constant potential boundary conditions,” *Soft Matter*, vol. 14, no. 26, pp. 5480–5487, 2018.
- [86] G. Trefalt, S. H. Behrens, and M. Borkovec, “Charge regulation in the electrical double layer: ion adsorption and surface interactions,” *Langmuir*, vol. 32, no. 2, pp. 380–400, 2016.
- [87] T. Markovich, D. Andelman, and R. Podgornik, “Charge regulation: A generalized boundary condition?” *EPL (Europhysics Letters)*, vol. 113, no. 2, p. 26004, 2016.
- [88] D. J. Acheson, “Elementary fluid dynamics,” 1991.
- [89] M. Marion and R. Temam, “Navier-stokes equations: Theory and approximation,” *Handbook of numerical analysis*, vol. 6, pp. 503–689, 1998.
- [90] G. Łukaszewicz and P. Kalita, “Navier–stokes equations,” *Advances in Mechanics and Mathematics*, vol. 34, 2016.
- [91] L. Petit, J.-P. Hulin, and É. Guyon, *Hydrodynamique physique 3e édition (2012)*. EDP Sciences, 2012.

- [92] L. R. White, "On the deryaguin approximation for the interaction of macrobodies," *Journal of colloid and interface science*, vol. 95, no. 1, pp. 286–288, 1983.
- [93] S. Rentsch, R. Pericet-Camara, G. Papastavrou, and M. Borkovec, "Probing the validity of the derjaguin approximation for heterogeneous colloidal particles," *Physical Chemistry Chemical Physics*, vol. 8, no. 21, pp. 2531–2538, 2006.
- [94] A. C. Eringen and K. Okada, "A lubrication theory for fluids with microstructure," *International journal of engineering science*, vol. 33, no. 15, pp. 2297–2308, 1995.
- [95] J. L. Anderson, "Colloid transport by interfacial forces," *Annual review of fluid mechanics*, vol. 21, no. 1, pp. 61–99, 1989.
- [96] S. Levine, J. R. Marriott, and K. Robinson, "Theory of electrokinetic flow in a narrow parallel-plate channel," *Journal of the Chemical Society, Faraday Transactions 2: Molecular and Chemical Physics*, vol. 71, pp. 1–11, 1975.
- [97] L. Bocquet and E. Charlaix, "Nanofluidics, from bulk to interfaces," *Chemical Society Reviews*, vol. 39, no. 3, pp. 1073–1095, 2010.
- [98] D. C. Prieve, "Migration of a colloidal particle in a gradient of electrolyte concentration," *Advances in Colloid and Interface Science*, vol. 16, no. 1, pp. 321–335, 1982.
- [99] D. G. Miller, "The origins of onsager's key role in the development of linear irreversible thermodynamics," *Journal of statistical physics*, vol. 78, no. 1, pp. 563–573, 1995.
- [100] D. G. Miller, "Thermodynamics of irreversible processes. the experimental verification of the onsager reciprocal relations.," *Chemical Reviews*, vol. 60, no. 1, pp. 15–37, 1960.
- [101] I. Gyarmati, "On the phenomenological basis of irreversible thermodynamics i," *Periodica Polytechnica Chemical Engineering*, vol. 5, no. 3, pp. 219–243, 1961.
- [102] A. Staverman, "Non-equilibrium thermodynamics of membrane processes," *Transactions of the Faraday Society*, vol. 48, pp. 176–185, 1952.
- [103] C. Werner, H. Körber, R. Zimmermann, S. Dukhin, and H.-J. Jacobasch, "Extended electrokinetic characterization of flat solid surfaces," *Journal of colloid and interface science*, vol. 208, no. 1, pp. 329–346, 1998.
- [104] G. N. Lewis, "The osmotic pressure of concentrated solutions, and the laws of the perfect solution.," *Journal of the American Chemical Society*, vol. 30, no. 5, pp. 668–683, 1908.
- [105] K. Janáček and K. Sigler, "Osmotic pressure: Thermodynamic basis and units of measurement," *Folia microbiologica*, vol. 41, no. 1, pp. 2–9, 1996.
- [106] S. Murad and J. Powles, "A computer simulation of the classic experiment on osmosis and osmotic pressure," *The Journal of chemical physics*, vol. 99, no. 9, pp. 7271–7272, 1993.

- [107] A. Klaassen, F. Liu, D. Van den Ende, F. Mugele, and I. Siretanu, “Impact of surface defects on the surface charge of gibbsite nanoparticles,” *Nanoscale*, vol. 9, no. 14, pp. 4721–4729, 2017.
- [108] S. de Beer, D. van den Ende, and F. Mugele, “Atomic force microscopy cantilever dynamics in liquid in the presence of tip sample interaction,” *Applied physics letters*, vol. 93, no. 25, p. 253106, 2008.
- [109] A. J. Goldman, R. G. Cox, and H. Brenner, “Slow viscous motion of a sphere parallel to a plane wall—i motion through a quiescent fluid,” *Chemical engineering science*, vol. 22, no. 4, pp. 637–651, 1967.
- [110] A. Ajdari and L. Bocquet, “Giant amplification of interfacially driven transport by hydrodynamic slip: Diffusio-osmosis and beyond,” *Physical review letters*, vol. 96, no. 18, p. 186102, 2006.
- [111] S. Shim, “Diffusiophoresis, diffusioosmosis, and microfluidics: surface-flow-driven phenomena in the presence of flow,” *Chemical Reviews*, vol. 122, no. 7, pp. 6986–7009, 2022.
- [112] E. Meyer, “Atomic force microscopy,” *Progress in surface science*, vol. 41, no. 1, pp. 3–49, 1992.
- [113] M. Quesada-Pérez, A. Martín-Molina, and R. Hidalgo-Álvarez, “Simulation of electric double layers with multivalent counterions: Ion size effect,” *The Journal of chemical physics*, vol. 121, no. 17, pp. 8618–8626, 2004.
- [114] A. Martín-Molina, J. G. Ibarra-Armenta, E. González-Tovar, R. Hidalgo-Álvarez, and M. Quesada-Pérez, “Monte carlo simulations of the electrical double layer forces in the presence of divalent electrolyte solutions: effect of the ion size,” *Soft Matter*, vol. 7, no. 4, pp. 1441–1449, 2011.